SEMICONDUCTOR PIXEL DETECTORS FOR IMAGING APPLICATIONS

Cinzia Da Via'

Department of Physics and Astronomy
University of Glasgow
Glasgow
G12 8QQ

Thesis submitted for the degree of Doctor of Philosophy

September 1997

To Michael

CONTENTS

LIST OF FIGURES

LIST OF TABLES

ABSTRACT

In this thesis the work is presented as follows:

Chapter 1 introduces the ideal detector characteristics for medical imaging. The requirements of the ideal diagnostic method are related to the various types of medical examinations, comparing the existing techniques and discussing results of Monte Carlo simulation studies. A review of existing detectors based on semiconductor microstrip and semiconductor pixel detectors introduces the hybrid Omega family, the pixel read-out electronics used by the author for the tests presented in the following chapters.

Chapter 2 describes a material defect characterisation study of semi-insulating gallium arsenide using a near-infrared absorption technique. Generally this technique is applied to "as-grown" materials but in this case, using a set-up proposed by the author, the concentration of the deep defect EL2 was monitored in a biased detector for different values of the applied electric field. The results obtained seem to support a theoretical model which predicts the presence of a "quasi"-neutral region inside the detector active volume.

The tests performed by the author using silicon and gallium arsenide pixel detectors coupled with the Omega2 and Omega3 read-out electronics are discussed in Chapter 3. The results reported include images of phantoms of different contrasts illuminated by X-ray sources, biological samples traced with β^- emitters and pixel detector characterisation using particle beams.

Chapter 4 describes the characterisation made by the author of a photosensitive version of the silicon pixel detector associated with the OmegaD and Omega2 read-out electronics. The tests were performed using light sources at different wavelengths, scintillating plastic fibres and scintillating crystals excited by radioactive sources and particle beams. The aim of this study was the search for a fast, high spatial resolution alternative to CCDs and multi-anodes photomultipliers for scintillating fibre particle tracking and for nuclear medicine based on scintillating crystals. The advantages and limitations of the present system are discussed with possible future improvements

The final chapter draws some conclusions about the work reported and offers some considerations for future developments. In particular, a description is given of a new pixel detector electronics chip with *single photon counting* capabilities, which followed the experience gained with the present versions of the Omega family electronics. The new electronics chip consists of a 64 x 64 array of pixels, each measuring 170 x 170 μm^2 and including a 15-bit binary counter. This chip is therefore extremely well-matched to a wide range of X-ray imaging applications, some of which are reviewed here.

INTRODUCTION

It is common to associate the concept of imaging by semiconductor detectors with silicon CCDs. This is not so incorrect. CCDs have become part of everyday life with videocameras and colour TV, and even in the more specialized fields of astronomy, medicine and recently high energy physics, CCDs represent today what emulsions used to represent 10-15 years ago. It is true that the technology is progressing rapidly and that the industrial effort is quite strong in this direction, but some intrinsic characteristics of this type of device make them inadequate for certain applications. The fast progresses in VLSI technology encouraged several groups to investigate other ways to overcome the limitations, in particular in local signal processing, read-out speed, dynamic range and in certain cases the analogue signal format, while preserving the positive features of CCDs like the intrinsic two-dimensionality, good spatial resolution, easy data handling, image processing and storage facility.

At CERN , the European Laboratory for Particle Physics there is at present a lot of activity directed towards the construction of the Large Hadron Collider LHC[1]. The conditions under which the experiments will work are really extreme, event simulations showing that there will be ~1000 tracks from every crossing of the proton beams, at 25ns intervals. There is therefore a need, not only for good spatial resolution and high read-out speed, but also the possibility for some kind of "smart" data processing on chip to select and reduce the amount of information to be treated and stored by the experimental data acquisition systems. These challenging requirements triggered the idea of Binary Hybrid Pixel Micropattern Detectors [2], which became the subject of investigation of the RD-19 collaboration.

The **binary** (1 or 0 response after comparison of the charge created in the detector by the passage of a charged particle with a discriminator threshold), **hybrid** (the detector and the read out electronics have the same segmentation but are processed separately and then connected using micro-bump bonding) **pixel** (true 2-D device array with pixel dimensions < 1mm) **micropattern** (the detector incorporates also information processing functions so that event selection or pattern recognition is actually integrated) **detector** was considered a "dream" in 1988[2]. Nowadays the read-out electronics chip

is in its 4th version and a telescope with 700 000 pixel elements is working successfully in the WA97 heavy ion experiment at CERN[4].

Particle physics experiments as well as many radiological and biochemical techniques record intensity distributions in space and time of ionizing particles or X-rays, so these different fields share a common goal from the imaging point of view. It was therefore natural to adapt the existing devices developed for high energy physics to medical imaging. The first tests were done using a modified version of the silicon pixel detector sensitive to visible light for the read-out of scintillating fibres (at that time a possible option for LHC tracking) and scintillating crystals, such as those commonly used in nuclear medicine for **P**ositron **E**mission **T**omography or **S**ingle **P**hoton **E**mission **C**omputed **T**omography.

Interest in the following step, efficient direct detection of X-rays at the energies of interest in most common radiological examinations, encouraged attempts to use different materials with higher absorption efficiencies with the aim to reduce the radiation dose given to the patient under examination. Gallium arsenide, with constituent atomic numbers 32 and 34, turned out to be the most promising candidate, despite problems at that time due to the incomplete charge collection efficiency caused by the presence of traps in the material. The first GaAs pixel matrix detectors were successfully bonded to the second version (Omega2) of the pixel electronics read-out chip in 1994, to the 3rd version (Omega3/LHC1) in 1996 (when a charge collection efficiency, CCE, of 100% was first measured in a high energy particle beam test) and to the 4th (Omega3')in 1997.

Some work needs still to be done before the production of a full system for medical imaging, but the present results give a strong support for the future developments.

CHAPTER 1

IMAGING IN MEDICINE

Semiconductor detectors are efficient charged particle and photon detectors which can, thanks to developments in device processing technology, be used as high precision 2-dimensional sensors. Among the different applications of this type of device are medical X-and γ-ray imaging and high energy physics. The emphasis of this chapter will be on the requirements of semiconductor detectors for medicine and high energy physics, their working principles, state-of-the-art performance and a comparison with traditional methods.

There are at present two main diagnostic methods based on radiation which are widely used in medicine: *X-ray radiology* and *nuclear medicine*. In the first the patient is illuminated with an X-ray beam from an X-ray tube and an image is taken of the absorption of parts of the body with different densities . In the second method, a drug labelled with a gamma ray-emitting isotope is injected into the patient. The drug is chosen according to the metabolism of the organ under study so that if anomalies are present they will act as accumulation centres for the drug. The information desired is in this case the spatial distribution of the source within the body.

For X-ray imaging the energy of interest goes from ~ 20keV (mammography) up to ~70 keV (dental and chest radiography) as can be seen in Figure 1-1. Within this energy range are performed digital radiology (DR) with some special applications like *scintigraphy* and *dual subtraction angiography* performed at 33.16 keV, the Iodine K-absorption edge [5], computed tomography (CT) between 50 and 70 keV, and synchrotron radiation applications which normally employ even lower energy X-rays. Synchrotron sources are the 'perfect' X-ray sources for medicine because the beam is monochromatic, but unfortunately compact sources to be sited in hospitals and laboratories are at present only at study level [6].

For radiological examinations higher X-ray energies than those mentioned above would be preferred because this would reduce the skin dose, but the soft tissue contrast would be reduced as well, so the working energy is chosen in relation to the type and structure of the object/organ to be imaged.

In mammography, for example, the current dose given to the organ is about 150 mrads and the minimum contrast an expert eye can distinguish in a developed film is ~3%. From recent studies [7] there are two possible types of early stage tumours which can be detected. The first is a small calcification (normally as small as 100 μm) with high contrast and the second a nodule of low contrast (from as low as 1%) with dimensions in the cm range. These dimensional and contrast requirements, together with the need to reduce the present dose, fix the detector parameters for this application.
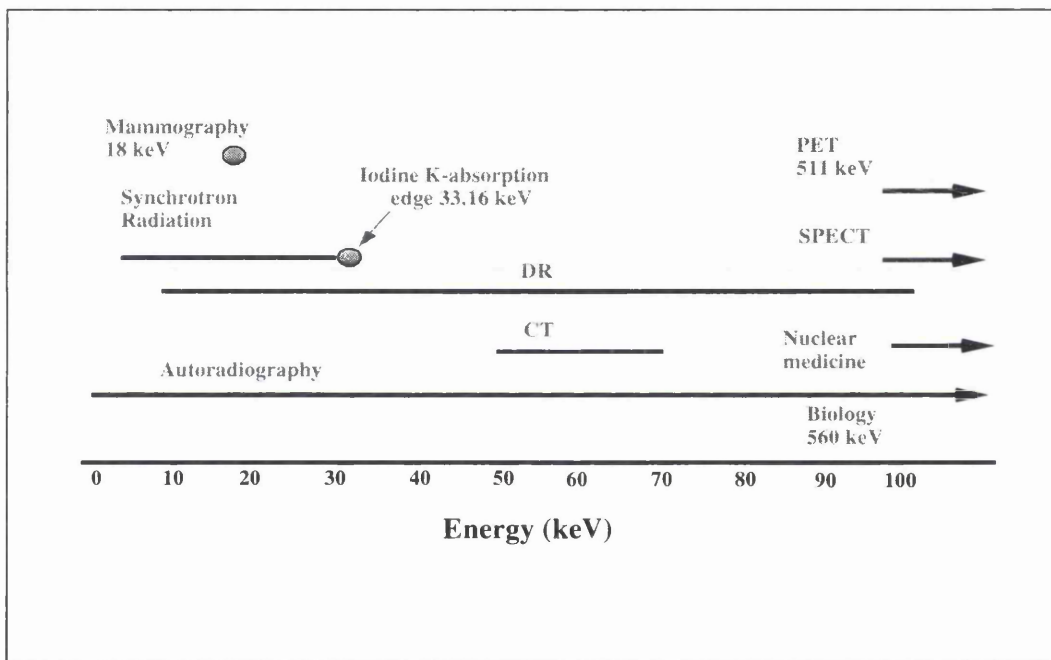
Figure 1-1. Energy range for the most typical medical and biological examinations.

In the case of nuclear medicine there are at present two main diagnostic methods: PET and SPECT.

Positron Emission Tomography (**PET**) consists of the detection of back-to-back photons from the annihilation of positrons, emitted by a drug injected into the patient, with electrons in the neighbouring tissue. The range of the positron in the patient's body fixes the intrinsic spatial resolution for the system at ~2mm.

In **SPECT** (Single Photon Emission Computed Tomography) the detector is sensitive to the direct emission of a photon by a radioisotope in the drug injected into the patient. The energy range of the photons to be detected goes from ~90keV up to 511keV or above.

A list of the main radioisotopes used in SPECT is presented in table 1-1.

table 1-1. Main radioisotopes used in SPECT [8]

isotope	half-life	energy (keV)
^{99m}Tc	6.02 h	140
^{201}Tl	73.5 h	69-83
^{123}I	13.2 h	156
^{131}I	8 yr	364
^{133}Xe	5.3 yr	81
125I	60 yr	27.5
^{113}In	1.05 h	393

In **biology** one of the principal techniques used to localise cells or macro-molecules and to study their metabolism is *autoradiography*. The tissues or the molecules under study are traced with a radioisotope which doesn't change their chemical properties. The radioisotopes, which are generally β^--emitters, are compatible with the metabolism of the cells so that the evolution of a certain biochemical process can be investigated by following the spatial distribution of the radioactivity.

The most commonly used radioisotopes in biology are listed in table 1-2.

table 1-2. List of the commonly used isotopes in biology [10].

isotope	energy (MeV)
^{3}H	0.0186
^{14}C	0.156
^{35}S	0.167
^{32}P	1.709
^{125}I	0.035 (γ)

The ideal detector for medical imaging has to give at the same time a good spatial resolution and be as safe as possible in terms of risk to the patient, namely be as efficient as possible to minimise the necessary dose for a good diagnosis. For a real device these two key requirements can be optimised by choosing the best detection technique and the optimal detector operation mode.

At present there are two main techniques used for X-ray detection. In the first the detector directly converts the absorbed X-ray into a charge signal; in the second there is an added step in which the X-rays hit a phosphor that converts the radiation into light which is then converted into an electrical signal. We talk of *direct* and of *indirect* X-ray detection in the first and the second cases, respectively.

The two main detector operation modes used to image X-rays are: *integration mode*, in which the total charge released by incident radiation is accumulated during exposure and the *counting mode* in which each detected photon is simply counted, independently of its energy.

Another rather recent nuclear medicine detection technique is based on *Compton scattering*. The position of the emitted photon, also called point-source response function (PSRF), is defined by backprojection reconstruction.

These different techniques and operation modes will be discussed in more detail in the following paragraphs.

DETECTOR TECHNIQUES FOR X-RAY IMAGING

The two possible ways to form an X-ray image, through direct and indirect energy conversion, are shown in Figure 1-2.

DIRECT
CONVERSION

INDIRECT
CONVERSION

X-RAYS

X-RAYS

photo conductor converts X-rays to electrical signals

conversion losses: increase in noise

phosphor converts X-rays to visible phorons

VISIBLE PHOTONS

X-RAY IMAGE

visible photons converted to electrical signals
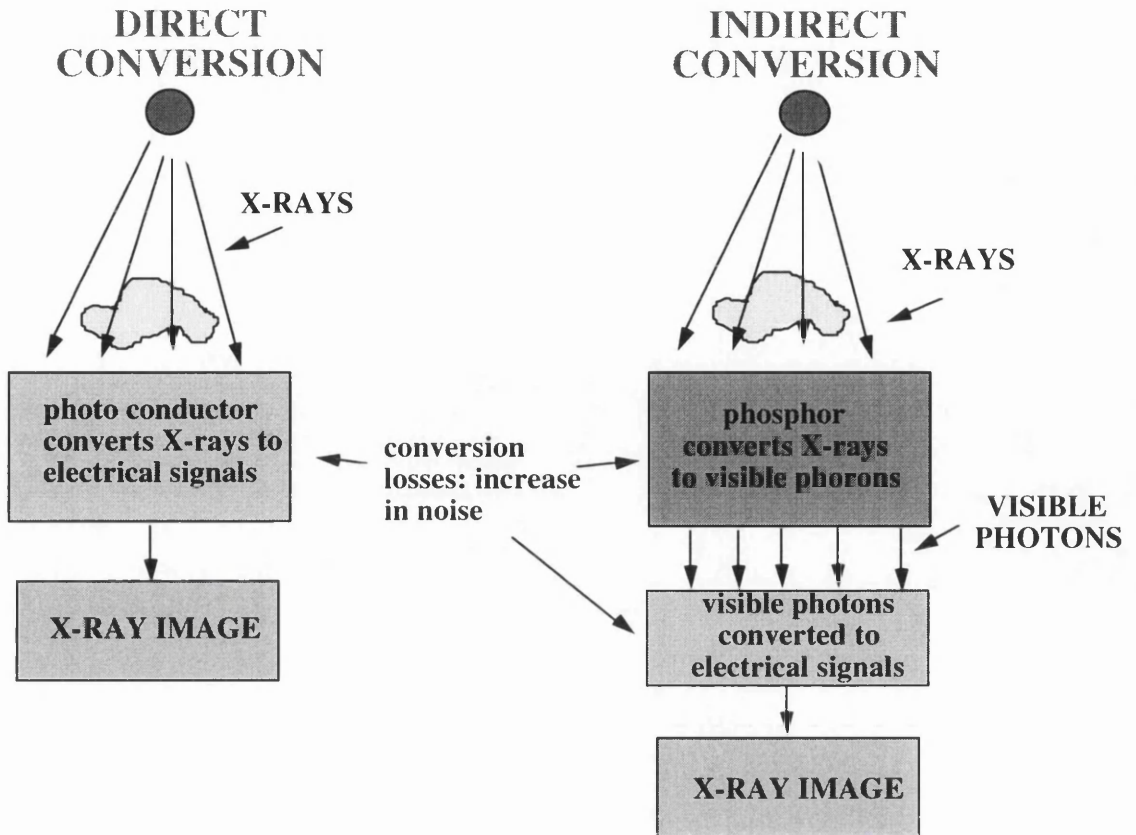
X-RAY IMAGE

Figure 1-2. Comparison of direct and indirect energy conversion steps to obtain an X-ray image.[9]

DIRECT X-RAY DETECTION

For X-rays energies below 100 keV direct detection is possible if the detection medium has a good absorption efficiency. As can be seen in Figure 1-3, for this range of energy the dominant interaction is the photoelectric process. This is enhanced for absorber materials of high atomic number Z. No single analytic expression is valid for the probability of photoelectric absorption per atom τ, over all ranges of energy E and Z, but a rough approximation is given by : $\tau = const \times \dfrac{Z^n}{E^{3.5}}$, where the exponent n varies between 4 and 5 over the X-ray energy region of interest [12]

21
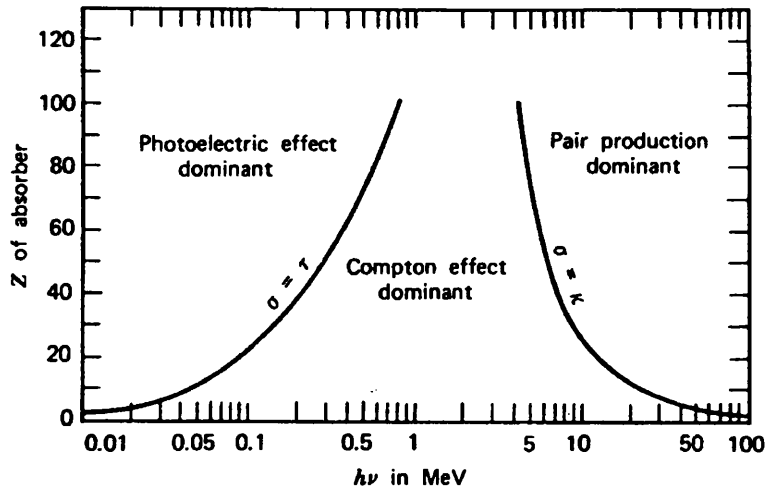
Figure 1-3. The relative importance of the three major types of gamma-ray interactions. The lines show the values of Z and hv for which the two neighbouring effects are just equal. τ, σ, κ are respectively the photoelectric, Compton and pair production probabilities of occurrence per unit path length in the absorber [12].

In Figure 1-4 are plotted the absorption efficiencies of some relevant semiconductors, (silicon, gallium arsenide, cadmium telluride), a commercial X-ray film and a gadolinium-based phosphor for X-ray energies between 0 and 100keV, where the photoelectric interaction is predominant.

Discontinuities in the curves or "absorption edges" appear at X-ray energies that correspond to the binding energy of electrons in the various shells of the absorbing atom. The edge lying highest in energy therefore corresponds to the binding energy of the K-shell electron. For X-ray energies slightly above the edge, the photon energy is just enough to initiate a photoelectric interaction in which a K-electron is ejected from the atom. For X-ray energies slightly below the edge, this process is no longer energetically possible and therefore the interaction probability drops abruptly.

Although the existence of an absorption edge can affect the performance of the image receptor, which can have different efficiency immediately below and above the edge, it can be a useful property if used to enhance the absorption capability of an organ with poor contrast. This is the case, for example, in *image subtraction*, a technique used to "contrast" internal organs in the human body. For that, drugs like iodine with a sharp absorption edge at a defined energy, are injected into the body. Two images of the same detail are taken at two different energies immediately above and below the K absorption-edge (~33keV for iodine) and afterwards subtracted, the result being an

enhancement of the regions in the body where the drug is present. An important application of this technique is *angiography* [11].

The photon scattering cross-section varies more slowly with energy than the photoelectric one and is approximately proportional to the atomic number. For soft tissue scattering becomes important only at higher photon energies where the photoelectric cross-section becomes small. For detectors with higher atomic numbers, some effect on the efficiency and image blurring due to scattering can be observed also at lower energies due to the higher spread of the scattered photons.
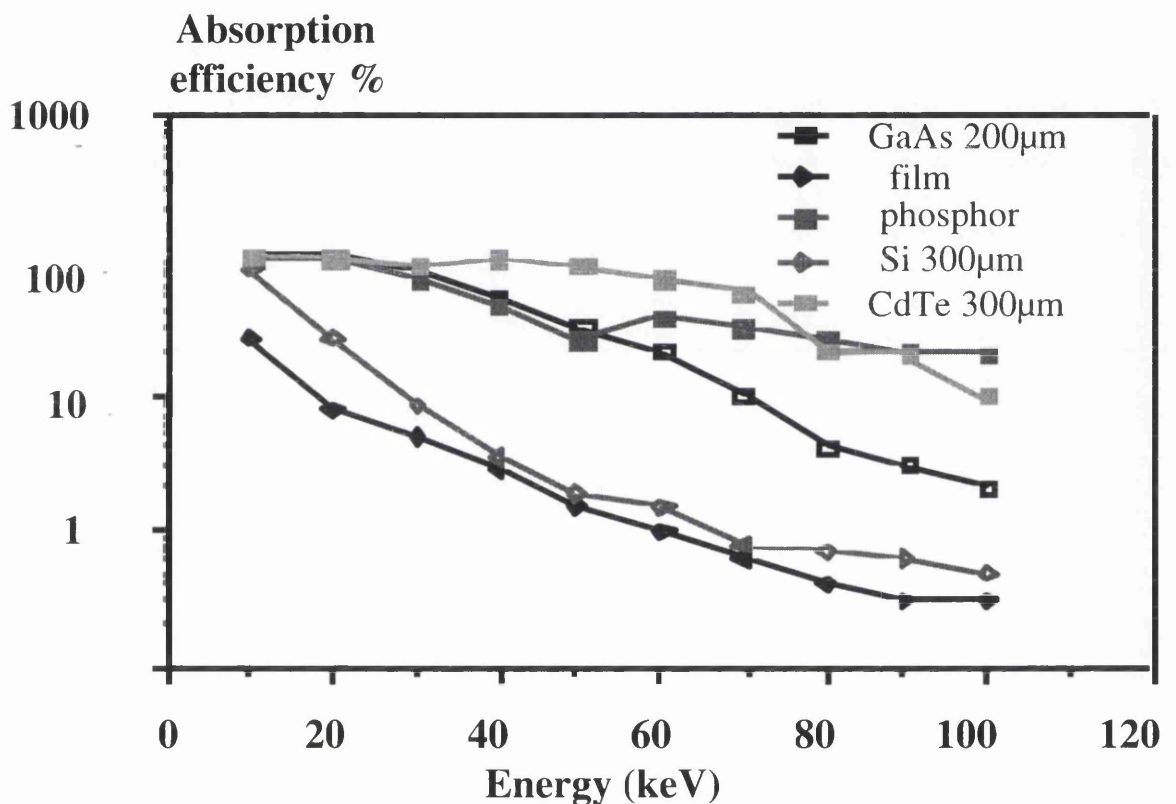
Figure 1-4. Absorption efficiencies of different detector media in the X-ray radiology energy range. [13].

INDIRECT X-RAY DETECTION

From Figure 1-4 it is clear that the absorption efficiency is rather poor above 20 keV in the case of film and silicon. In order to increase this efficiency, a converting medium is

sometimes used, typically a scintillating material ~70-300μm thick between the contrasting detail and the detector. In scintillators the X-ray photon excites an electron which later returns to a stable state through de-excitation, generating a light pulse which is then converted into an electrical signal. This double conversion of the incident radiation leads to deterioration in the spatial resolution of the image obtained, but sometimes this is preferable if it results in a lower risk for the patient.

Using gadolinium based phosphors as an example, the conversion efficiency from energy deposited by an X-ray in the screen to fluorescent light photons is at best 18%. The probability for these photons to reach the detector is ~50%. The sensitivity of the latter in converting visible photons into film blackening or electron-hole pair creation in a semiconductor device depends on the detector material and on the wavelength of the incident radiation, but is at the level of a few per cent for visible photons. The contrast ratio, which defines the capability of distinguishing the presence of an object, is then dominated by the global quantum efficiency of the system, defined as the combination of all the efficiencies involved in the conversions and energy transfer of the original radiation.

At energies above 100keV, the conversion from X-rays to visible photons is normally made using ~1-2 centimeter thick scintillating crystals. The diffusion of the light in such a thick layer of transparent material is solved by shaping the crystals as optical guides. The light produced by the scintillation process is confined within the guide and the spatial information is then given by its lateral dimension. In Table 1-3 are listed some of the best known scintillating crystals, some of which, like BGO, have also been used successfully in high energy physics calorimetry.

For all energies, effects of scattering are minimised by the use of physical or electronic collimation or by the use of a scanning system. The physical collimators, usually made from tungsten interspersed in plastic, decrease the scattered radiation and allows only photons with a straight trajectory to be detected. A drawback to using such grid systems is that some desired photons are accidentally absorbed as well, with the consequence that the radiation dose must be larger to ensure that enough desired photons will reach the detector.

Figure 1-5 shows the absorption efficiencies and penetration depths at different wavelengths for different semiconductors. In the blue-green region, which is the most common emission region for existing scintillators the quantum efficiency for silicon is ~50% and the penetration depth of blue light is ~2μm. Photodiodes and CCDs are commonly produced using silicon. For detection of visible light the thickness of the active detector is not a problem.

	NaI:Tl	CsI:Tl	BaF₂	YAG:Ce	YAP:Ce	BGO
Density(g/cm³)	3.67	4.51	4.89	4.57	5.37	7.13
Index of refraction	1.85	1.78	1.5	1.82	1.95	2.15
Crystal structure	Cubic	Cubic	Cubic	Rhombic	Monoclinic	Cubic
Hygroscopic	yes	slightly	slightly	no	no	no
Integrated light output (%Na:Tl)	100	45	20	15	40	15
Wavelegnth (peak) (nm)	415	550	325	550	370	480
Decay const. (ns)	230	900	630	70	25	300
Radiation length (cm)	2.9	1.86	2.03	3.5	2.7	1.1
Photon yield at 300K (10³ ph/MeV)	38	52	10	8	10	3

Table 1-3. Characteristic properties of some common scintillators[22].
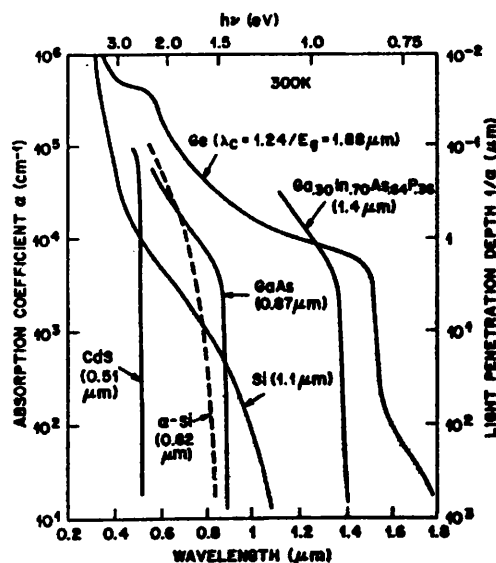
Figure 1-5. Optical absorption coefficients for different semiconductor materials [24].

DETECTOR OPERATING MODES IN X-RAY IMAGING

The two main detector operation modes used to image X-rays are: *integrating mode*, and *counting mode*.

INTEGRATING DEVICES

The detectors commonly used for radiology can provide an integrated quantification of the incident radiation. Film is a typical example of signal integration and the response of commercial film is expressed in optical density D.

The optical density, defined as $D = \log_{10}(I_0 / I)$, where I_o and I are the beam intensity before and after passage through the film, is an indication of the blackening of the emulsion after X-ray exposure. A typical curve is illustrated in Figure 1-6 together with the combined response of the film plus a phosphor screen[13].
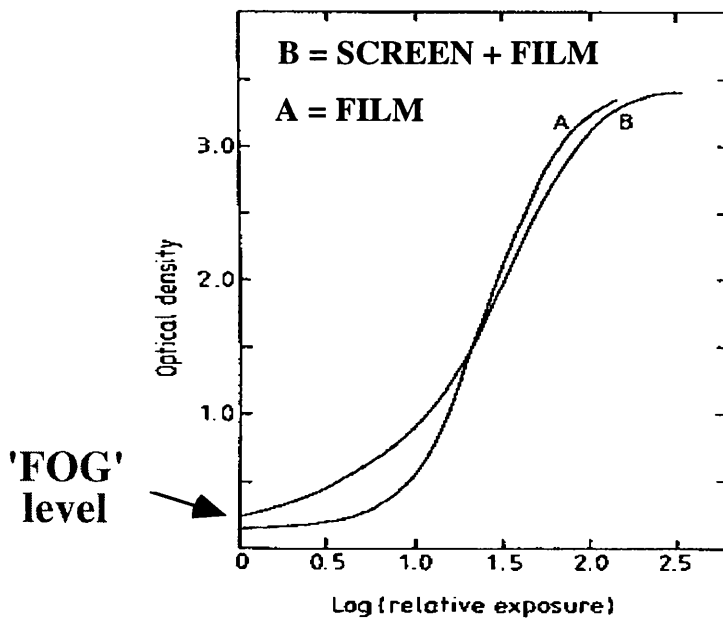
Figure 1-6. Optical density of a film and a film plus screen combination commonly used in X-ray imaging. The optical density measures the blackening of the film and is expressed as the logarithmic ratio of the incident light intensity over the transmitted light through the film. The presence of a "fog level" in the film response fixes an intrinsic limitation in the detection of low contrast objects [13].

26

It is possible to transform the integrated information given by the optical density into a digital form using a densitometer. The linearity which can be obtained corresponds to ~63 Gray scale levels, similar to that of the human eye. In the lower part of the exposure range the sensitivity is limited by the so-called *fog level* while the linearity of response is limited by the low efficiency in the activation of the emulsion grains. The fog-level is represented as a baseline shift of the curve and is a consequence of spontaneous blackening of the silver grains present in the emulsion during film development. The range of exposure for which the film response is linear is called its *latitude*. The contrast is expressed by the *gamma* factor of the film. Other examples of signal integration are given by silicon CCDs and some types of smart pixels. In the case of the CCD the information accumulated after a certain exposure is stored as electrical charge in potential wells located underneath the sensitive pixels and then transferred through a *shift register* to the read-out electronics.

More details about the different detector approaches and their performances are given later in this chapter in the section devoted to *semiconductor detectors.*

COUNTING DEVICES

The lower possible limit to patient irradiation is set by the statistical fluctuation or *quantum noise* in the number of photons reaching unit area. This limit is almost impossible to reach using conventional screen-film radiography, due to its poor sensitivity but can in principle be approached using digital methods. In the latter case image quality is conveniently expressed by the signal-to-noise ratio, SNR defined as $(SNR)^2 = E(N)Aq \times Ix$[16], where E(N) is the expectation value of the Poisson distributed number of photons N, Aq is the quantum absorption efficiency, or fraction of incident photons detected, and Ix is a statistical factor which includes the internal noise of the detector.

With a totally absorbing detector and neglecting scattering, all incident photons are registered, Aq=1 and each incident photon imparts all its energy to the detector. In this sense a totally absorbing detector extracts all the information contained in the incident beam. However the SNR depends on the detector mode of operation. When operating in counting mode the energy information is lost and all photons are equally registered as a single 'event'. It follows that Ix=1 and $(SNR)^2$=E(N).

When the detector is used in energy integrating mode Ix still equals 1 with monoenergetic photons but with incident X-rays of a range of energies it is less than one and $(SNR)^2 < E(N)$. It can be then concluded that an ideal detector optimising the SNR disregards the energy information and counts the photons.

Monoenergetic photons of sufficient intensity for X-ray imaging are provided at present only by synchrotron sources. The spectra emitted by the conventional tubes used for radiological examinations are not monochromatic and moreover the relative intensity changes after the radiation passes through matter. An example is shown in Figure 1-7 where the X-ray spectrum of a molybdenum target tube is taken before and after attenuation by 5 cm of tissue.

With a tungsten target tube similar spectra can be obtained which have a characteristic emission peak at ~60keV, the energy for which the contrast between bone and fat is maximum. As can be seen, there is a large difference between the X-ray spectrum before and after passage through the patient, the difference being due to the photons that interact with the patient and deliver dose.

The contribution to the dose due to soft photons is attenuated by the use of aluminium or copper filters, depending on the tube potential [13].
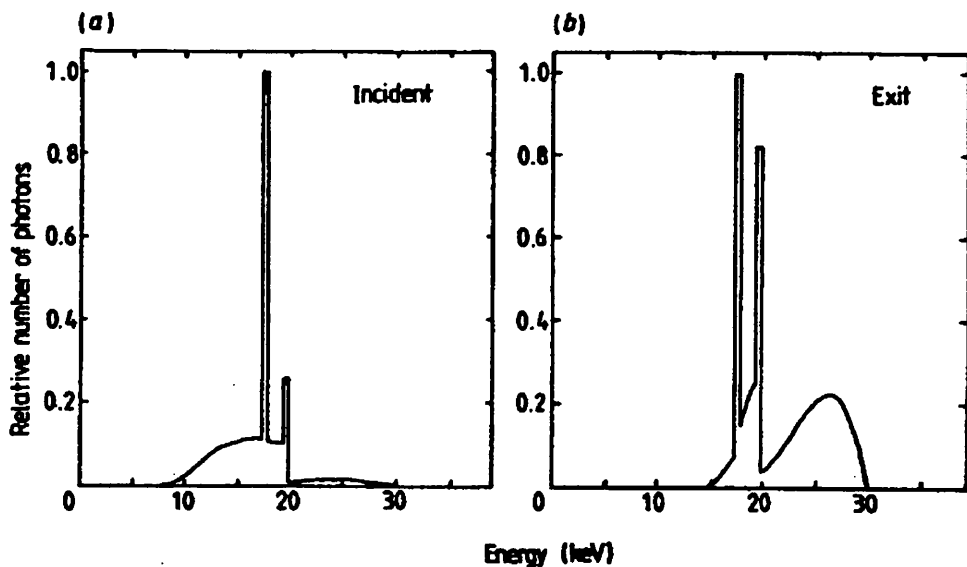
Figure 1-7. X-ray spectra for an X-ray tube with a molybdenum target; 30 kV constant anode potential with 0.03 mm molybdenum filter. The spectra are shown before and after attenuation by 5cm of tissue[13]

Another definition of signal to noise which directly considers the number of photons counted is given by $\dfrac{n-n'}{\sqrt{n+n'}}$, where n and n' are respectively the number of photons on the background and inside the target image and $\sqrt{n+n'}$ is the quantum noise. The contrast ratio SCR is defined as $\dfrac{2(n-n)'}{\left(n+n' \right)}$ with the same definition as above for n and n'. If p is the fraction of photons absorbed by the target, $n'=\left(1-p \right)n$, the signal then becomes S=pn and the noise $N = \sqrt{n(2-p\;)}$. With these definitions the contrast ratio is given by $SCR = \dfrac{2p}{2-p}$ and the number of background photons needed to see a detail with a given contrast C is $n = \dfrac{2(\; SNR\;)^2}{pC}$. A plot of n versus the contrast ratio for different SNR is given in Figure 1-8 [17].

The signal to noise ratio which gives the minimal probability of a false signal for a given detector, as reported in the literature, is SNR=5[13]. For an area of $1mm^2$ and a standard illumination of $\sim4\times10^6$ photons/mm^2 this translates, for example, to $\sim3\%$ minimal detectable contrast ratio for the human eye on a radiographic film [13][17]. If the detector used has an active surface
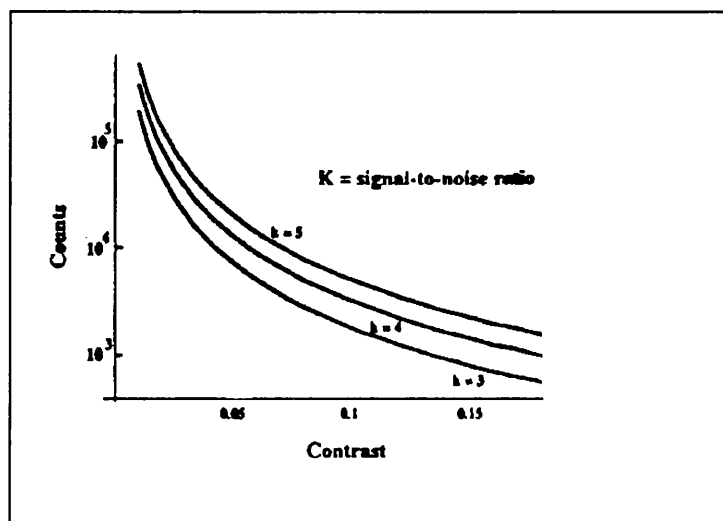
Figure 1-8. Visibility curve simulated using the SNR and SCR formulae [17].

A subdivided in square pixels of area d^2 and M is the total number of photons reaching the surface A, then M/n=A/d^2 and the contrast ratio in this case is given by $\dfrac{\sqrt{2}SNR}{d\sqrt{M\,/\,A}}$,

so it depends on the square root of the superficial dose and for a counting detector, limited only by quantum noise, the minimal detectable object is given by the pixel size.

When other noise sources such as electronic or detector noise are included in the signal, the minimum detectable contrast would be reduced by a factor R = *quantum noise / total noise,* in the case of an integrating device. All these calculations are made in the ideal case of a *photon scattering free* device.

The behaviour of a pixel detector in the presence of photon scattering has been studied by Monte Carlo simulations [21]. Some results of this analysis are reported in Figure 1-9 for a GaAs device. The curve represents the DQE, detection quantum efficiency, defined as the ratio of the SNR at the output to the SNR presented at the input of an imaging system, $DQE = (SNR)/(SNR_{in})$.

If coherent and incoherent scattering are included in the calculations, the curves show that the difference of DQE between photon counting and charge integration, for different energies is minimal for a 500μm thick device at 40 keV.
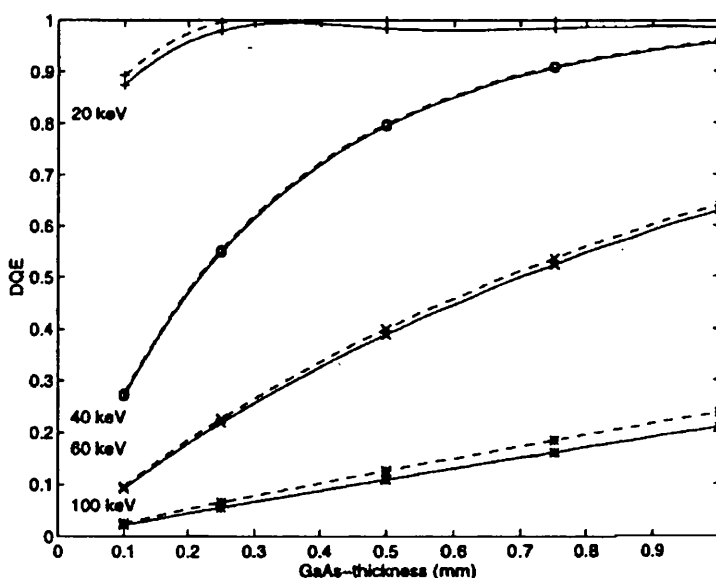
Figure 1-9. The DQE for the case of photon counting (--) and energy integration (-) for a GaAs detector at 20, 40, and 100 keV[21]

Unfortunately no tests on existing devices have been performed so far to confirm the results of the simulations.

The Compton scattering camera, sometimes also called the "electronically collimated" camera has been proposed for imaging in SPECT. The camera consists of two detecting planes (Figure 1-10).
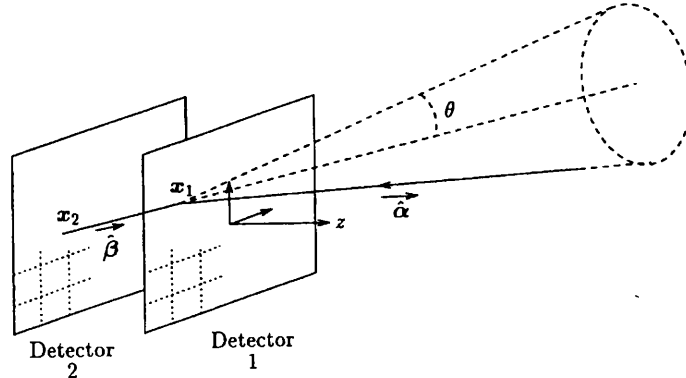
Figure 1-10. Geometry of the Compton scattering camera. The back projection for a particular trajectory through x_1 and x_2 with scattering angle θ localises the photon as having its origin somewhere on the surface of a cone (represented by the dotted line) [19]

The first detector, closest to the source distribution, is designed so that Compton scattering is the dominant interaction process while the second detector is designed so that complete absorption of photons takes place. From the two position measurements and angle of scatter, it is possible to back-project to localise the photon as having been sourced on the surface of a cone whose apex lies at the point of Compton scatter, x_1, has semiangle θ and axis of symmetry passing through the two detection points, x_1 and x_2, as shown in Figure 1-10 [18][19][20].

The Compton scattering angle θ can be calculated from the deposited energy ΔE in the first detector by : $\cos\theta = 1 - \dfrac{mc^2\Delta E}{(E-\Delta E)E}$, where E is the initial photon energy m is the electron mass and c the speed of light.

Both detectors should measure at the same time the position and energy of the interacting photons, but for the best precision in the determination of the point source emphasis should be given to the following parameters:

- energy resolution of the first detector;
- position resolution of the two detectors;
- thickness of the detectors;
- distance from the source of the first detector.

For a Ge-NaI detector with 2mm and 10mm thickness, respectively, the best intrinsic efficiency, (defined by the likelihood of a detected coincidence given that the photon is incident on the face of the scattering detector), has been calculated to be ~2% while the spatial precision in the point source reconstruction is ~3mm with source-first detector distance ~20mm. The same performance is obtained for a Si-NaI Compton camera if the silicon thickness is 4 mm. In both cases considered by the Monte Carlo study the isotope used was ^{99m}Tc [19]

IMAGE QUALITY CRITERIA

In the previous section SNR, SCR and DQE were defined and used as quality criteria for radiographic systems. For the general definition of quality of an imaging system, however, it is common to use other parameters. Among these others are the line spread function (LSF) and the modulation transfer function (MTF).

LINE SPREAD FUNCTION (LSF)

The line spread function (LSF) is a way of defining the resolution of a system in one dimension. In practice this can be seen as a measure of how much a line in an object becomes blurred after being detected.

MODULATION TRANSFER FUNCTION (MTF)

MTF is a more general method to define an image quality in terms of spatial resolution. It is a measure of the fidelity of reproduction of object details of varying spatial frequency. An MTF of 1 for a certain frequency indicates that the full amplitude of a signal having this frequency is recorded in the image whereas an MTF of 0 indicates that the signal is not recorded at all.

MTF can be defined as: $MTF(f) = \sqrt{NEQ(f)W_{\Delta E/E}(f)}$, where NEQ is the noise equivalent quanta, or the photon fluence that would give the same SNR if the source of

all noise was attributed to quantum fluctuation, $W_{\Delta_{E/E}}$ is the Wiener (noise power) spectrum and f is the spatial frequency [16].

The requirements for an ideal detector have been presented and some motivation has been given to justify the choice of semiconductors as radiation detectors for medical imaging applications. In the following paragraphs, semiconductor properties will be reviewed and details given of the different detector configurations.

SEMICONDUCTORS

INTRODUCTION

Detectors based on semiconductors have been available since the early '60s. The principle of operation of this kind of device is based on the collection of electron-hole pairs after their generation in the material by the interaction of charged particles or photons. This property, typical of semiconductors, is related to the energy of the electrons inside the crystalline material in which the periodicity of the lattice establishes allowed energy bands for electrons. The energy of each electron must be confined in one of these bands, which may be separated by gaps or ranges of forbidden energies. The main difference between insulators, conductors and semiconductors depends on the height of the forbidden gap between two specific energy bands: the *valence band* which corresponds to those electrons that are bound to specific lattice sites within the crystal, and the *conduction band* which represents electrons which are free to migrate through the crystal. For insulators and semiconductors the number of electrons within the crystal is just adequate to fill completely all the sites within the valence band and this is why in the absence of thermal excitation both materials, theoretically would not show any electrical conductivity. In a metal, on the other hand, the highest occupied energy band is not completely full and the electrons can easily migrate throughout the material since the energy barrier they have to cross is very small.

If sufficiently high energy is given to an electron in the valence band it can be elevated across the bandgap to the conduction band. Physically, this process simply represents the excitation of an electron that is normally part of a covalent bond such that it can leave the specific bonding site and drift through the crystal. The excitation process not only adds an electron to the conduction band but also leaves a vacancy in the valence

band, called a "hole". This process in semiconductors is defined as *electron-hole pair creation*. A quantitative evaluation can be made, introducing the Fermi-Dirac distribution function $f_D(E)$ which expresses the probability that a state of energy E is filled by an electron.

$$f_D(E) = \frac{1}{1 + \exp\left(\dfrac{E - E_f}{kT}\right)}$$
Equation 1-1

E_f, the Fermi level, is the energy level for which the occupation probability is 50%. For a pure semiconductor, called also *intrinsic*, the Fermi level is approximately in the middle of the band gap. This is not the case for *extrinsic* or *doped* materials, which allow high concentrations of electrons (n-type) or holes (p-type), by moving the Fermi level close to the conduction or valence band edge.

The procedure for doing this is to replace a small fraction of the semiconductor atoms in the crystal lattice by dopant atoms with a different number of valence electrons. Depending on the lattice structure characteristics of the semiconductor the dopant atom can be a *donor* or an *acceptor*. If the dopant is a donor the number of its covalent electrons is higher than that of the intrinsic semiconductor, the sharing of the covalent bonding between the electrons of different neighbouring atoms is not complete and one electron is loosely bound. Already at room temperature this electron would be free and available for conduction. In this case the density of electrons in the conduction band is high and electrons are said to be *majority carriers* (n-type).

Alternatively if the dopant is an acceptor its number of covalent electrons is lower than in the intrinsic semiconductor. This means that one bond is incomplete and can be easily filled by an adjacent electron. Holes are then majority carriers in p-type material and behave as reasonably mobile, positively charged carriers in the sea of fixed negative charge. The charge concentrations are given by shifting the Fermi-Dirac distribution to within the hole binding energy, namely close to the valence band edge. Since the density of electrons is then negligible the latter would become *minority carriers*.

A typical example of doped semiconductor is given in Figure 1-11 [26] in which is sketched the general situation of doped silicon.

34
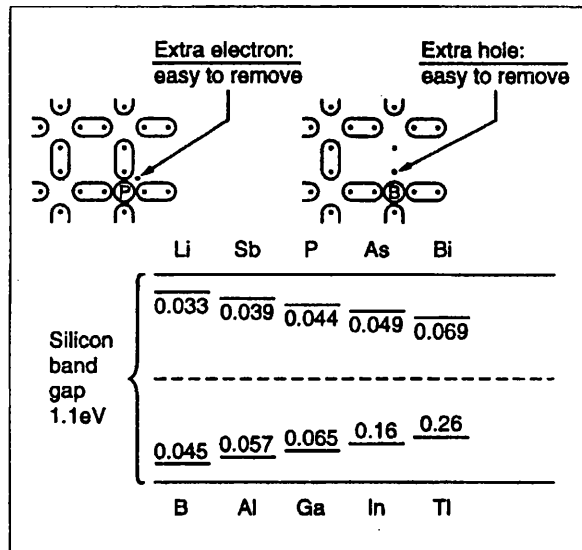
Figure 1-11. Sketch of bond occupation in doped silicon (top) and energy levels of different n- and p-type dopants within the band gap (bottom)[26].

The bond occupation is schematically represented in the top half of the Figure while the bottom half shows the energy levels within the bandgap corresponding to various n- and p-type dopants. Levels of acceptor atoms are conventionally measured from the top of the valence band and levels of donor atoms are measured from the bottom of the conduction band. A typical concentration of electrons in n-type silicon is $\sim 10^{16}/cm^3$.

The electron in the conduction band can be made to move under the influence of an electric field. The hole, representing a net positive charge, will also tend to move in an electric field, but in a direction opposite to that of an electron. The motion of both charges contributes to the conductivity of the material and is the combination of a random thermal velocity and a net *drift velocity* parallel to the direction of the applied field. At low to moderate values of the electric field intensity, the drift velocity v is proportional to the applied field, the *mobility* μ for both electrons and holes can be defined as $v_{e,h} = \mu_{e,h} E$, where E is the electric field magnitude. In semiconductors the mobility for electrons and holes is roughly of the same order while in gases, for example the mobility for free electrons is much larger than that of the positive ions.

The *resistivity* ρ of the material depends not only on the concentration of the free carriers but also on their mobilities. $\rho = \dfrac{1}{q_e\left(\mu_n \cdot n + \mu_p \cdot p\right)}$, where n and p are the electron and hole concentrations and q_e is the electron charge. For an intrinsic

semiconductor $n = p = n_i$, with n_i the intrinsic carrier density, while their approximate expression, (valid for the case of Boltzmann statistics, for which the Fermi level must be at least several times kT below E_c), is

$$n = N_c \exp\left(-\frac{E_c - E_f}{kT}\right) \qquad p = N_v \exp\left(-\frac{E_f - E_v}{kT}\right) \qquad \text{Equation 1-2}$$

where N_c and N_v are the effective densities of states for electrons and holes. The neutrality condition for intrinsic semiconductors is derived from the dynamic equilibrium between thermal generation and recombination and can be obtained by equalising the above expressions, showing that the Fermi level in this case lies very close to the middle of the band gap. For doped materials the two concentrations become

$$n = n_i \exp\left(\frac{E_f - E_i}{kT}\right) \qquad p = n_i \exp\left(\frac{E_i - E_f}{kT}\right) \qquad \text{Equation 1-3}$$

where $pn=n_i^2$. The deviation of doped semiconductors from intrinsic ones can be simply represented by a shift in the Fermi level with respect to the intrinsic level. In thermal equilibrium, the increase of electron concentration by donor doping causes a decrease in the concentration of mobile holes by recombination such that the pn product is always constant. It is generally valid, in fact, to think of n-type material in equilibrium as containing only mobile electrons and p-type material as containing only mobile holes, which are the majority carriers in each case.

A list of semiconductors used or potentially interesting for use as detectors and their properties, where known, is presented in Table 1-4.

36

Table 1-4. Semiconductors and their properties [27].

Material	Eg (300 K) eV	μ_e (300K) cm^2 V^{-1}s^{-1}	μ_h (300K) cm^2 V^{-1}s^{-1}	τ_e s	τ_h s	Z	E (e-h) eV
Si	1.12	1500	600	3×10^3	3×10^3	14	3.61
Ge	0.67	3900	1800	10^3	10^3	32	2.96
C(diam.)	5.47	2000	1550	10^8	10^8	6	13.2
GaAs	1.43	8500	420	10^7	10^7	31-33	4.27
GaP	2.25	300	100	10^8	10^8	31-15	7.8
CdS	2.42	300	50	10^8	10^8	48-16	6.3
CdTe	1.5	~1000	~80	10^6	10^6	48-52	4.43
InSb	0.17	78000	750	10^7	10^7	49-51	1.2
GaSb	0.67	4000	1400	10^8	10^8	31-51	
InAs	0.36	~33000	460			49-33	
InP	1.27	4600	150			49-15	
AlSb	1.52	200	550			13-51	
HgI2	2.1	100	4	10^7	10^8	80-53	4.15

SEMICONDUCTOR DETECTORS

In order to construct a practical radiation detector, some means must be provided to collect the electrical charges created by the radiation at the boundaries of the semiconductor material. The simplest way is to collect the charges by applying a voltage through two metal contacts on the opposite faces of the detector layer, but this principle can only be applied to insulators and to very high resistivity semiconductors (semi-insulators), for example CdTe which has a resistivity as high as 10^9 ohm cm. Silicon can have a resistivity as high as ~5x10^4 ohm cm but even then the leakage current at room temperature would be too high for X-ray or particle detection applications. It is possible however, to generate a region of internal electric field devoid of free charge carriers, leading to a lower leakage current, by creating a reverse-biased junction. For this purpose two main detector structures are generally used :

- *p-i-n* diodes
- *metal-semiconductor (Schottky)* structures.

37

A *p-i-n* diode is a *p-n* junction with a doping profile tailored so that an intrinsic layer, the *i* region, is sandwiched between a *p* layer and an *n* layer. In practice the intrinsic layer is either a high resistivity *p* or *n* layer.

\

The junction is normally fabricated by diffusion of *p* and *n* regions into the high-resistivity substrate. An abrupt p-n junction in thermal equilibrium is shown schematically in Figure 1-12 with the space charge distribution, electric field distribution and potential variation with depth. Here V_{bi} is the built-in potential (or diffusion potential).

If N_A and N_D are, respectively, the acceptor and donor impurity concentrations , the depletion layer thickness for a one-sided abrupt junction is

$$W = \sqrt{\frac{2\varepsilon_s}{qN_B}\left(V_{bi} - 2kT/q\right)}$$

Equation 1-4

where N_B is N_A or N_D depending on whether $N_A \gg N_D$ or vice versa. The electric field is calculated by integrating Poisson's Equations

$$-\frac{\partial^2 V}{\partial x^2} \approx \frac{q}{\varepsilon_s} N_D \qquad \text{for } 0 < x \le x_n$$

Equation 1-5

$$-\frac{\partial^2 V}{\partial x^2} \approx \frac{-q}{\varepsilon_s} N_A \qquad \text{for } -x_p \le x < 0$$

Equation 1-6
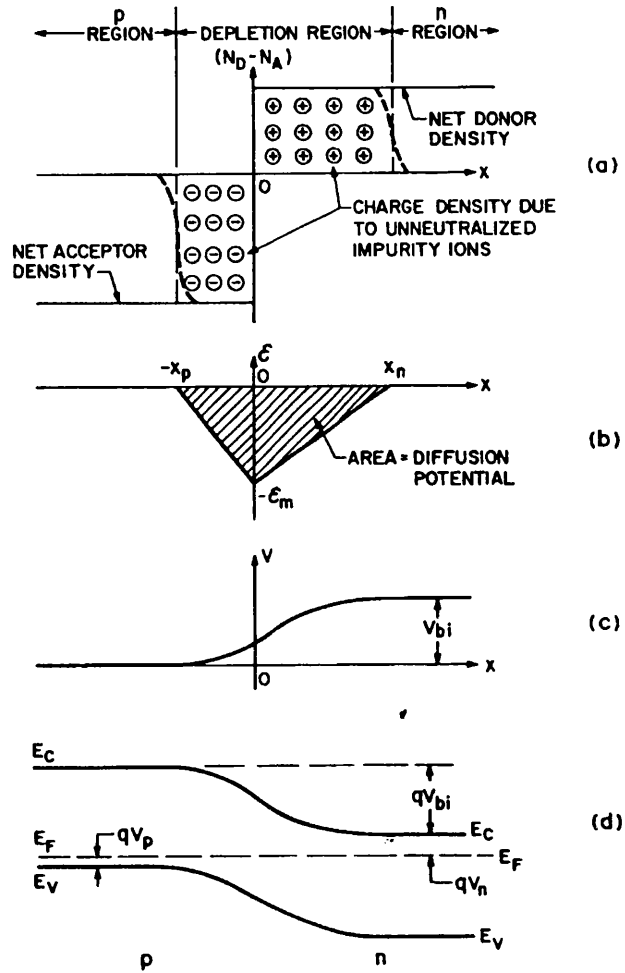
Figure 1-12. Abrupt p-n junction in thermal equilibrium. a) space-charge distribution b)electric field distribution, c) potential variation with distance where V_{bi} is the built-in potential d) energy-band diagram.

and the electric field E then becomes:

$$E(x) = -\frac{qN_A(x+x_p)}{\varepsilon_s} \quad \text{for } -x_p \leq x < 0 \qquad \text{Equation 1-7}$$

$$E(x) = \frac{qN_D}{\varepsilon_s}(x-x_n) \quad \text{for } 0 < x \leq x_n \qquad \text{Equation 1-8}$$

The depletion layer capacitance per unit area for a one-sided abrupt junction is given by:

$$C \equiv \frac{dQ}{dV} = \frac{\varepsilon_s}{W} = \sqrt{\frac{q\varepsilon_s N_B}{2}} \left(V_{bi} \pm V - 2kT/q\right)^{-1/2} \qquad \text{Equation 1-9}$$

where dQ is the incremental increase in charge per unit area upon an incremental change of the applied voltage dV.[24].

When a metal makes contact with a semiconductor, a potential barrier is formed at the metal-semiconductor interface. In a so-called Schottky barrier, the depletion layer of the metal-semiconductor contact is similar to that of a one-sided abrupt junction and the thickness of the active region is proportional to $V^{1/2}$ when there is a stable space charge in the semiconductor. The metal and the semiconductor have different work functions $q\phi_m$ and $q\phi_s$, defined as the energy difference between the Fermi level and the vacuum level. When the metal and the semiconductor are put in contact (Figure 1-13))[24], the Fermi levels of the two materials must be equal at thermal equilibrium. In addition the vacuum level must be continuous.
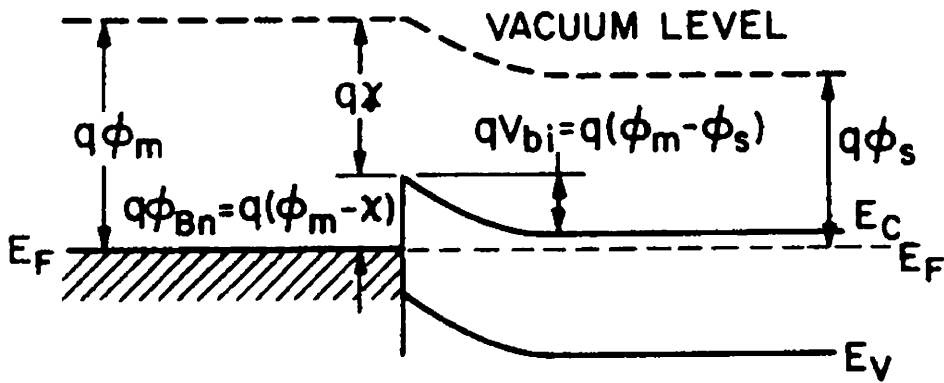
Figure 1-13 Energy band diagram of a metal-semiconductor contact in thermal equilibrium. The work function $q\phi_m$ for the metal and $q\phi_s$ for the semiconductor, respectively, represent the difference between the Fermi level and the vacuum level. qX is the electron affinity, defined as the difference between the conduction band edge and the vacuum level in the semiconductor, the barrier height $q\phi_{Bn}$ is the difference between the metal work function and the electron affinity of the semiconductor (both $q\phi_{Bn}$ (eV), and ϕ_{Bn}(V) are referred to as the barrier height) [24]

These two requirements determine a unique energy band diagram for the ideal metal-semiconductor contact. For this ideal case the barrier height ϕ_{Bn} is simply the difference between the metal work function and the electron affinity, $q\chi$, of the semiconductor,

defined as the energy difference between the conduction band edge and the vacuum level. With these conditions, the dependence of the depletion layer width W on the applied bias voltage V is similar to that of a p-n junction. That is: $W = \sqrt{\dfrac{2\varepsilon_s (V_{bi} - V)}{q N_d}}$,

where V_{bi} is the built-in potential, q is the electron charge, N_d the carrier concentration and ε_s is the permittivity of the material.

SILICON DETECTORS

Three main type of detector structures based on silicon have been used for imaging applications:

- Microstrips
- Charge Coupled Devices
- Smart pixels, either hybrid (in which the read-out electronics is separated from the detector) or monolithic (with the electronics integrated on the same substrate as the detector).

MICROSTRIPS

Silicon microstrip detectors pioneered the use of semiconductors for large area imaging of tracks in high energy physics. Different attempts were subsequently made to use this powerful tool in medical or biological imaging, as will be discussed in the following paragraphs.

A silicon microstrip detector (Figure 1-14) consists essentially of a one dimensional array of reverse biased *p-i-n* diodes in which the parallel strip collecting electrodes have an inter-strip distance of ~20-50 μm . The diode structure is formed typically by implanting boron ions along thin strips on the front side of an n-type high resistivity silicon substrate, to create p-type regions. The processing is then completed by deposition of aluminium.

On the back side ohmic contact, an n^+ implant is normally used, to prevent massive electron injection when full depletion is reached, followed by metal deposition. The

back side process can be uniform over the whole surface (in a single-sided device) or again segmented, as in the front side, (for a double-sided device). In the latter case the orientation of the strips on the two sides is usually at an angle, (sometimes 90^0), to provide 2-D information.

There are, however, some problems related to the processing of the strips on the back side, for example inter-strip short circuits. These are due to the accumulation of positive ions in the oxide layer which attracts negative charges to the oxide-silicon interface, creating a low-resistivity electron channel between read-out strips. This problem was solved by the insertion of p+ (p-stop) implants between adjacent strips, polarised negatively to create a negatively charged depletion layer. This repels the mobile electrons back to the surface accumulation layers and so interrupts the flow of electrons between neighbouring strips. Another problem is related to the coupling between the strips used to bias the junction and the (usually grounded) read-out electronics. Decoupling capacitors are normally integrated on one end of the strips for this purpose while the bias voltage is applied through integrated polysilicon resistors.

In high energy physics, silicon microstrip detectors have already been used successfully in some large scale experiments [28].

Silicon strips for medical imaging applications have used both single-and double-sided detectors. The low absorption efficiency of a 300 μm thick silicon substrate for radiological X-rays restricts the applications of these devices to low energy photons or beta particles such as are used for biochemical tracing.
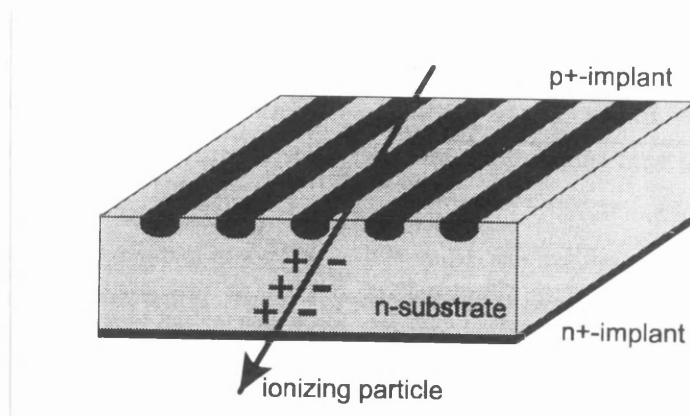
Figure 1-14. Sketch of a silicon strip detector

One original way to overcome the limitation and detect directly high energy X-rays is the approach which uses the strips in their longitudinal direction (Figure 1-15).

The detector is transformed in this way into a layer of pixels, which are scanned over the interesting area. In the reported set-up, a strip length of 4 mm gives a detection efficiency higher than 90% at 25 keV X-ray energy.
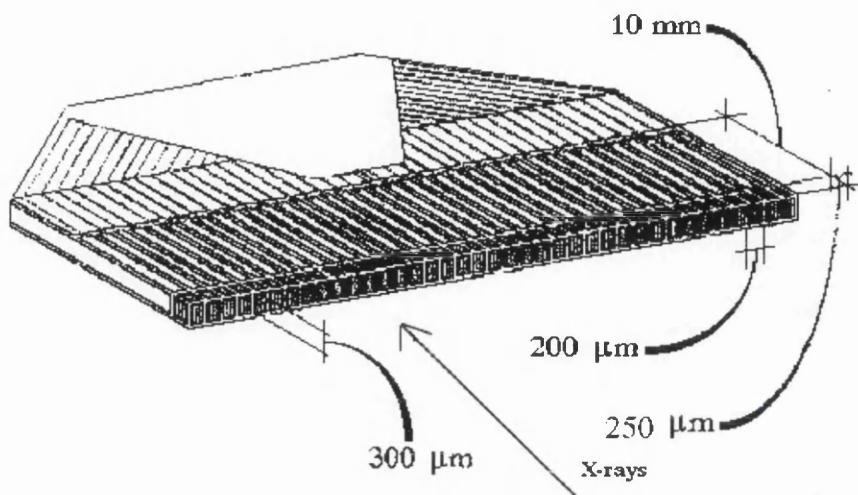
Figure 1-15. Original way to use silicon microstrips and transform the detector into an efficient X-ray detector. With the X-ray direction parallel to the strip length instead of being orthogonal to it the detection efficiency improves up to 90% [29].

A system of two layers of strips/pixels already exists and a further improvement includes the possibility of piling as many layer of strips as necessary to cover large areas. The main problem to be solved in this respect is the mechanical interconnection with the read-out electronics [29][30].

A much more traditional way of using silicon microstrip detectors is employed in imaging DNA sequences or ^{32}P labelled human epithelial cells. In the first reported account of this application [31] the strips had a pitch of 250μm since to distinguish all DNA fragments required a spatial resolution of at least 500μm. The strips were 2.0 mm long and processed in 8 columns, each measuring 4.0mm. The electronics used was developed for high energy physics applications, with a shaping time of 700ns and a read-out rate of 10-20 MHz, but with no self triggering capability is limited in its efficiency. The noise of 600 e$^-$ (equivalent noise charge) allows a sensitivity as good as ~10 keV.

A second such application used double-sided strip detectors [32] which were originally developed for digital X-ray imaging in mammography [33]. The strip pitch was 25μm on the front and 50μm on the back side, (with read-out electronics pitch 100μm), and the threshold was set as high as 100 keV. The reconstruction of the distribution of radioactivity was made with parallel processors which looked for time coincidences between orthogonal strips [34]. The total detector area was 1.4 x 1.4 cm^2 and large surfaces were covered by scanning methods. The 64 channel multiplexed analogue electronics had an equivalent noise charge of 1000 e$^-$ and a minimum threshold of ~22keV. The measured efficiency of the system was 20% and the measured sensitivity was 0.002 nCi/mm^2.

Double-sided strip detectors with 50μm read-out pitch on the two sides and a total area 40.96 mm^2 have also been used to detect low energy X-rays and β$^-$ particles. The 128 channel read-out chip (Viking-3) has a low noise (~200 e$^-$ rms) amplifier with test inputs and the possibility of suppression of noisy channels. The read-out rate is ~150 kHz, (limited by the slow external analogue-to-digital conversion to 500 Hz) [35].

The ambiguities in the reconstruction of the particle interaction point at large radiation fluxes, together with the high capacitance which causes a deterioration in the signal-to-noise, are the critical points in using strip detectors for imaging in medicine. Their application to particle tracking is essential however, and most of the HEP experiments presently working or planned for the future include silicon microstrips in their inner detector part [51][52].

CHARGE-COUPLED DEVICES (CCDs)

CCDs represent the most widely recognised definition of "pixellated" semiconductor devices. The CCD is so commonly used in everyday life that it deserves some description of its operating principles and its main scientific applications.

An imaging CCD consists of a pixellated silicon detector, comprising a square matrix of potential wells, so that charge generated below the silicon surface can be accumulated. In a second stage the stored charges can be transferred in parallel from one row to the next by manipulating clock voltages in a parallel register.

After reaching the last row, the stored signals are then transferred sequentially onto the output node, which is connected to the input of a charge sensitive preamplifier. A reset

signal is used to restore the output node to its nominal value after reading the signal from each pixel. In this way the CCD image is converted from a 2-D charge pattern to a serial train of pulses well suited to display in a video monitor. Figure 1-16 shows a sketch of the principal structural features of a CCD. Voltage pulse sequences applied to the Iϕ and the Rϕ gates are used to manipulate the parallel shift register and the output node serial charge transfer, respectively.

The fabrication of modern CCDs is based on the buried-channel architecture, in which the charge is stored in the bulk of the detector approximately 1 μm below the surface. The displacement of the accumulated charge is done by moving the potential wells along one column by clocking of the gate electrode voltages. For example in the 3-phase CCD structure the physical width of each CCD pixel is given by the total dimension of 3 gates $\phi_1 + \phi_2 + \phi_3$.
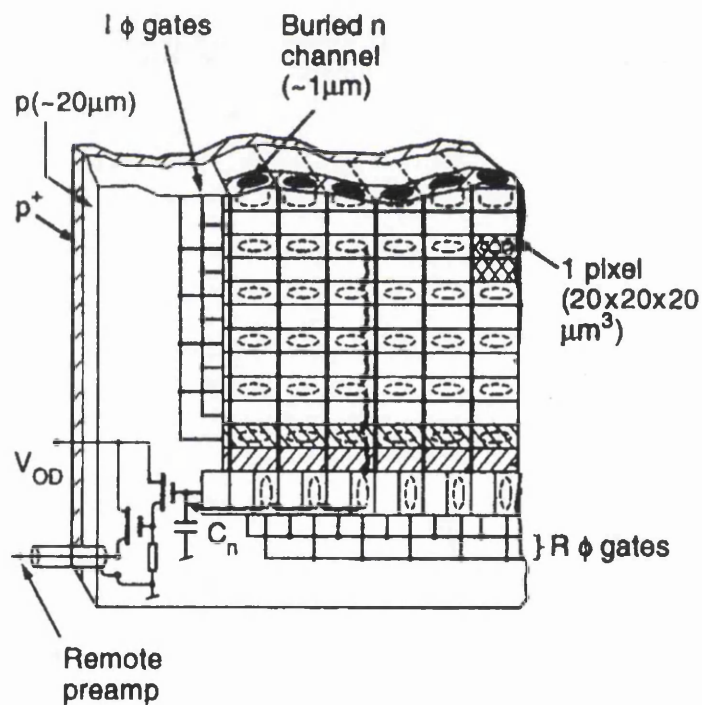
Figure 1-16. Corner region of a CCD showing the principal structure features, in particular the Iϕ and Rϕ gates which are used to transfer the accumulated charge to the read-out preserving position information.

The static situation is for one gate (e.g. ϕ_1) to be at a high voltage level, so that electrons are stored under this gate. The manipulation of the voltages between ϕ_1 and ϕ_2 allows the charge to move to ϕ_2 and the confinement of the charge under the proper pixel is assured by keeping ϕ_3 low during the operation. The digitization of the charge normally gives 256 Gray levels (with a potential well capacity per pixel of 10^5 e⁻) and the read-out clock frequency can be as high as 30 MHz for a 20 µm pixel size [26].

CCDs were developed and are widely used as video sensors but about 15 years ago there was a first theoretical evaluation of their potential as high precision detectors for ionizing particles [36]. Since that time many improvements have been made to overcome the detection efficiency deficit due to the limited active thickness. Fully depleted 200 µm thick *pn* CCDs fabricated on high resistivity silicon could match the detection efficiency requirement[45]. Furthermore, traditional light-sensitive CCDs manufactured with a phosphor layer grown on the top of the sensitive CCD input window are nowadays most commonly used for X-ray detection. Examples of the successful use of this technology are found in mammography [37][38], synchrotron radiation crystallography[39], dental radiology[46], biology[40] and astronomy[41]. The advantages of using this type of detector for such applications are

- very high spatial resolution provided by the small pixel size when used directly
- moderately low cost supported by the market (if standard production CCDs can be used)
- read out electronics package easily available
- TV or computer connection

The disadvantages are

- spatial resolution comparable with other systems when used with phosphor
- high cost when custom made (especially for large areas)
- slow read-out speed, limitation for high rate applications
- charge integration
- low temperature operation required to suppress leakage current integration, a limitation for high sensitivity applications

Among the high energy physics experiments which have used CCDs, the SLD collaboration built the entire vertex detector for their experiment at the SLAC linear collider [42]. One previous, extensive use of CCDs in this type of application was in

the scintillating fibre tracking detector in UA2 [[43] and CHORUS [44], which used CCDs after a sophisticated image intensifier chain.

ACTIVE PIXEL SENSORS

There are two main classes of active pixel device: *hybrid* and *monolithic* pixel detectors.

HYBRID PIXELS

In a hybrid pixel device the electronics and the detector are processed separately and connected together only in a final stage. For a true 2-dimensional pixel device the interconnection of the detector elements to the corresponding electronics is made through the "flip-chip" process. Such a process makes use of micro-drops of solder which create at the same time a low-capacitance electrical and mechanical contact as illustrated in Figure 1-17 and Figure 1-18.
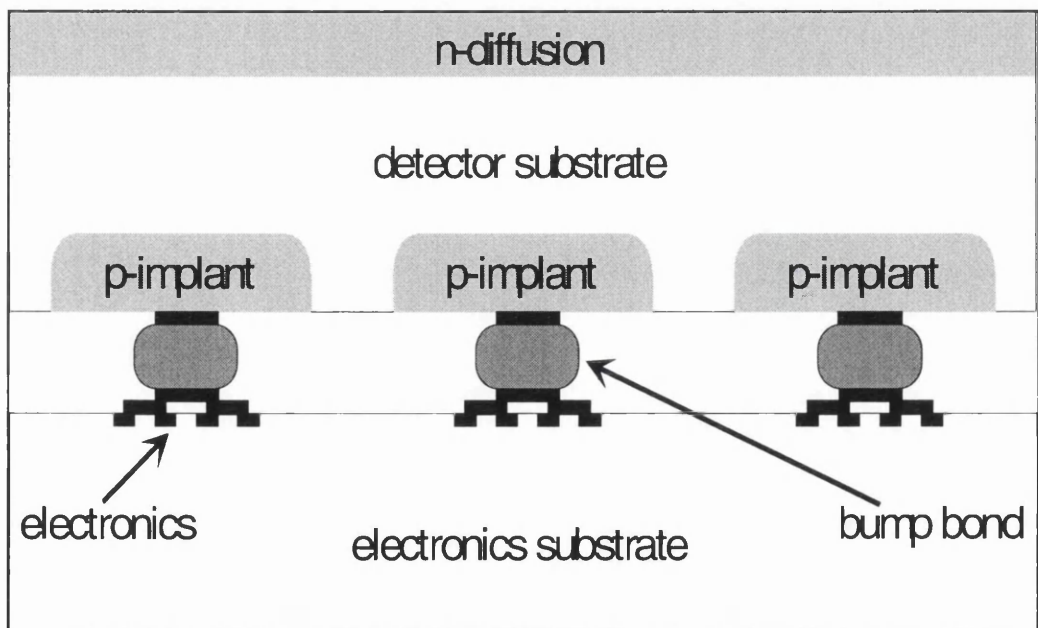
Figure 1-17. Hybrid silicon pixel detector

The advantages of the hybrid technology are

- the possibility of using different materials for detector and electronics
- the optimisation of the detector and electronics separately
- a high yield
- large areas

and the disadvantages

- the bump-bonding is not always reliable
- few manufacturers offering bump-bonding services
- cost.

More details of the bump-bonding technology are given in the following paragraphs.
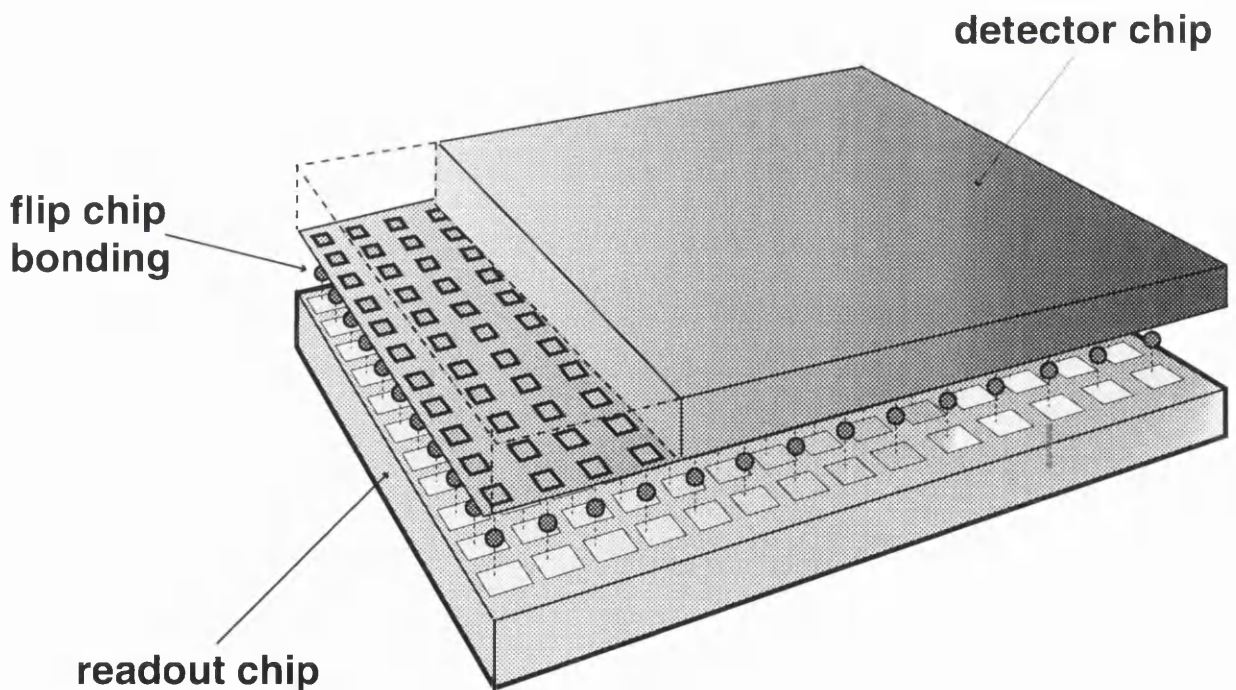
Figure 1-18. Sketch of a pixel detector matrix.

Hybrid pixel detector technology started from a pioneering study for high energy physics tracking applications at the LHC [47] and the SSC [48] and generated widespread interest in the high energy physics community evidenced, for example, by generic asynchronous detection applications [49], the Delphi vertex detector upgrade [50], the RD-19/WA94 heavy ion experiment [4] and finally ATLAS [51] and CMS [52].

The step towards medical imaging applications was short. CdTe [53], GaAs [112] and silicon [54][55][56][57][58] hybrid pixel detectors were produced and tested, but so far none of these efforts has led to the development of a full system.

In this thesis emphasis is given to the author's contribution to the Omega hybrid pixel detector development carried out within the framework of the RD-19 collaboration.

THE OMEGA HYBRID PIXEL FAMILY

Hybrid technology was chosen as the main focus by the RD-19 collaboration for the pixel detector development for high energy physics at the Large Hadron Collider. The proposal was accepted in the R&D programme for the LHC in 1990 [59]. The common feature for all the hybrid pixel electronics versions is the binary information about the hit pattern. The evolution of the VLSI technology over a 4 year interval allowed the implementation of additional functionality in smaller pixel cell sizes, the number of transistors per pixel going from ~80 to ~400.

The different versions of the pixel electronics developed towards LHC specifications were all tested in the heavy-ion, fixed-target experiments WA94-WA97, operating in the Omega multi-particle spectrometer in the west experimental area (WA) at CERN.

"Omega" therefore became the label for the RD-19 family of pixel read-out electronics chips.

The first member of the series was the Omega-D read-out chip [60][61], an *asynchronous binary* read-out chip which consists of an active matrix of 16 x 63 elements and a test row of pixels for a total area of 8 x 4.8 mm^2. Every pixel measures 75 x 500 μm^2. As shown in the block diagram of Figure 1-19, it consists of an analogue front end with charge preamplifier, leakage current compensation through a dummy

pixel placed at the end of each column and an externally tunable comparator threshold with a dynamic range between 3 000 and 10 000 electrons.
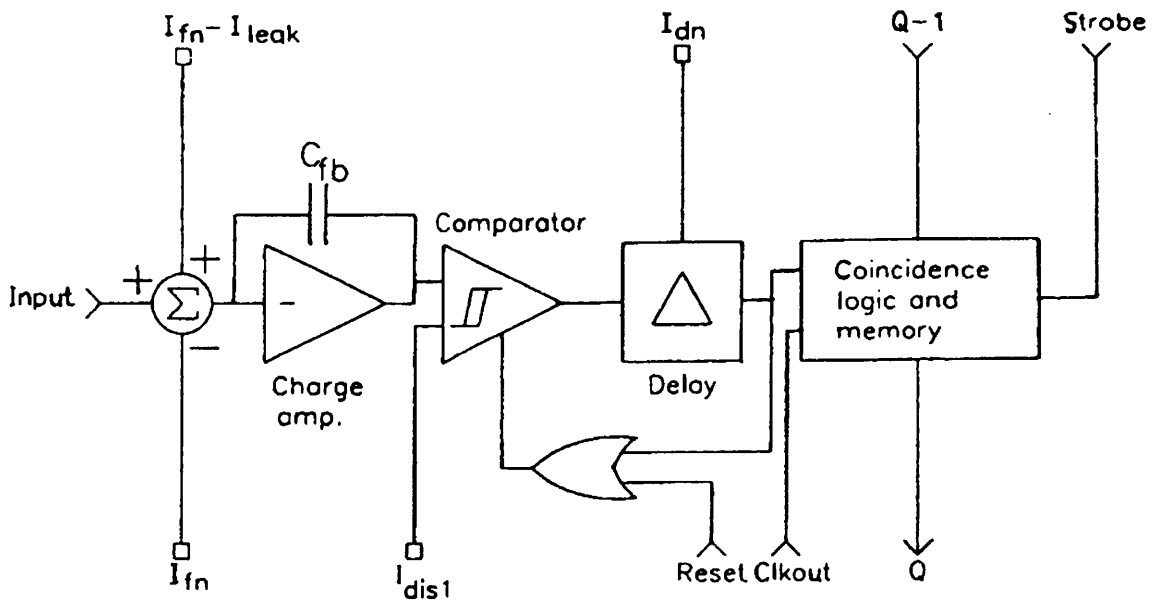
Figure 1-19. Block diagram of the D-Omega-Ion pixel read-out circuit.

The comparator output signal is delayed to match the timing of the coincidence and read-out logic. The delay is also adjustable externally. After a hit is detected the pixels have a dead time of ~400 ns before being reset, and a "1" is stored in the memory flip-flop only if the falling edge of the comparator output coincides with an external strobe. When the strobe is low a multiplexer connects all of the flips-flops of one column together so that by using the "clkout" signal the flip-flops behave as a single shift register. The clock frequency in this version is 1MHz, corresponding to a total read-out time of ~60 μs. The power consumption of a single pixel cell is ~25 μW and the equivalent noise charge without and with the detector bonded are 100 e⁻ and 170 e⁻ rms, respectively. The signal delay was adjustable from ~400ns to ~1μs.

In the following version, Omega-2, some improvements were made with respect to Omega-D, principally to make it compatible with large area coverage[62]. Specific features of the new chip include a reset which can be applied immediately following a false trigger, an improved minimum strobe time of ~100 ns and a read-out clock rate of ~20 MHz giving a full matrix read-out time of ~3 μs.

Complementary control lines were also implemented with the aim of reducing charge injection from the digital busses across the air-gap to the sensitive detector input terminal. The single pixel dimensions are maintained, as are the good performances in

50

terms of noise and power consumption. The read-out of the cells is unchanged from the previous version, with the flip-flop of each pixel again becoming part of a vertical shift register which is driven by the 'clkout' signal.

Some extra logic has been added, however, to ensure that the clocking out is done only when the chip is enabled by the experiment read-out system. In this way the same control signal and data bus may be shared by many chips.

This electronics has been used successfully to cover 5 x 5 cm^2 planes for a total of ~500 000 pixel in the WA97 experiment.

Omega3/LHC1 is the latest version of the pixel family [63]. The chip covers a sensitive area of 8 mm x 6.35 mm with a matrix of 16 x 127 read-out cells. It has been manufactured using a high density process with which almost 5 times more logic may be integrated in a 50 x 500 μm^2 pixel compared to the previous versions.

Several improvements have been implemented from the previous versions as shown in Figure 1-20 a) and Figure 1-20 b). The main changes are the provision of an analogue test signal, a 3-bit fine delay adjust, allowing strobe widths as low as 40 ns, flip-flops for testing and masking and the presence of a wired fast-OR in each column for alternative trigger generation or to resolve eventual timing ambiguities.

The read-out clock frequency is ~40 MHz. The control logic defines 4 distinct modes of operation selectable via external control lines.

The *mode 0* is the normal mode of operation in which the strobe is connected to all pixels during data taking and the read-out is performed with the same shift-register scheme as for the previous versions. In the *mode 1* operation the strobe is enabled by a signal generated on chip by the fast-OR, allowing a wider strobe to be used while keeping timing ambiguities rare.

This mode is essential in cases for which no other trigger is possible, for example for the detection of X-rays. The *mode 2* and *mode 3* are initialisation modes which allow reading and writing the contents of the delay adjust register and the test and mask registers. In both mode 0 and mode 1 the delay adjust and the external fast-OR output can be enabled or disabled.
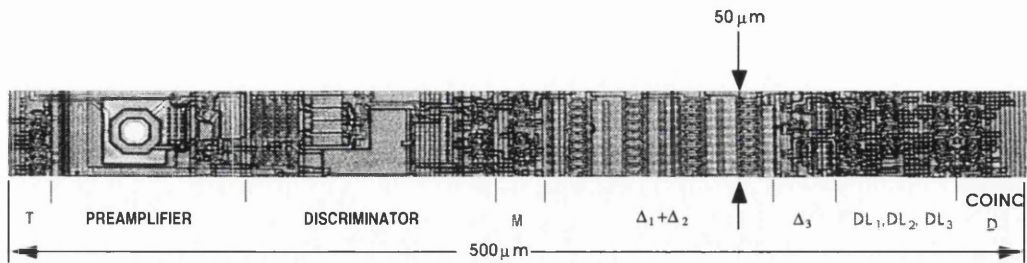
Figure 1-20 a). The Omega3/LHC1 pixel cell
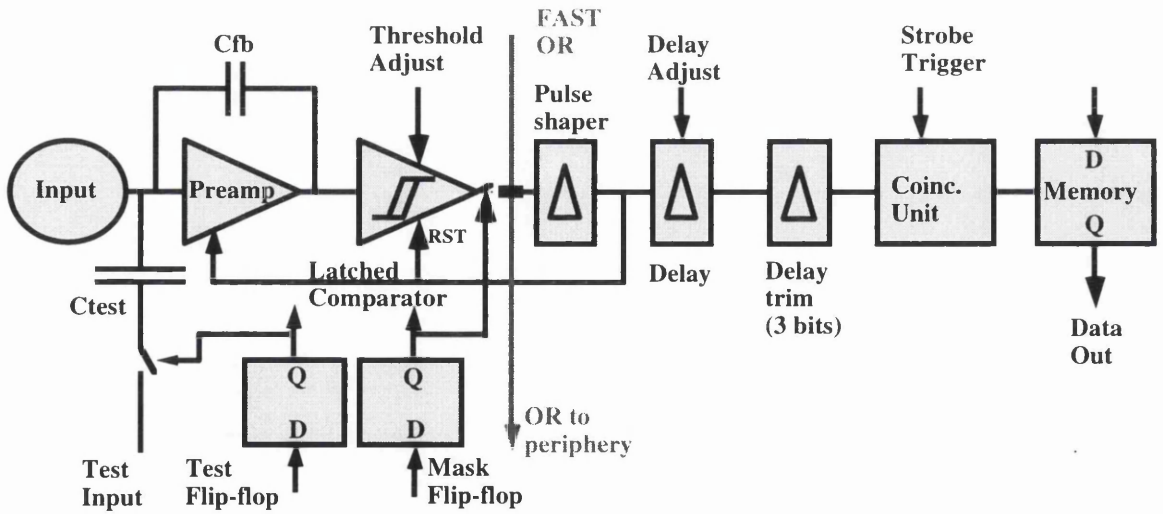
Figure 1-20 b). The Omega3/LHC1 block diagram. The dimensions of the pixel are 50 x 500 μm^2.

In Table 1-5 are summarised the parameters of the Omega pixel family electronics chips.

Table 1-5. The Omega pixel electronics family.

	Year	cell size (μm^2)	transistors per cell	columns x rows
Omega-D	1991	75 x 500	81	16 x 63
Omega2	1993	75 x 500	81	16 x 63
Omega3/LHC1	1995	50 x 500	395	16 x 127

All the work on imaging presented in the following chapters has been carried out using the 3 versions of the Omega electronics chip, connected respectively with a traditional silicon pixel detector, a modified version of the silicon detector sensitive to visible light, (for indirect X-ray and charged particle detection), and finally a gallium arsenide pixel detector used mainly for direct X-ray particle detection but also tested in particle beams.

LARGE AREA COVERAGE

The greatest achievement made with the Omega2 and the Omega3/LHC1 pixel detector was the coverage of a 5 x 5 cm^2 area. Six read-out electronics chips were mounted side by side and bump-bonded to a single piece silicon pixel detector "ladders". The dead area between one pixel detector chip and the following one was filled by making 1 mm long pixels (instead of 500 μm) as can be seen in Figure 1-21.

Figure 1-21. Detail of a pixel detector "ladder" used to cover a 5 x 5 cm^2 area. The interconnection between adjacent pixel electronics is made using twice as long detector pixels.

To cover a full plane two ceramic cards have been used, each one containing six (Omega2) or 4(Omega3) such ladders. The reason for this was the presence of a gap between ladders which had to be covered by staggering the ladders on their short dimension as shown in Figure 1-22 in the case of Omega2
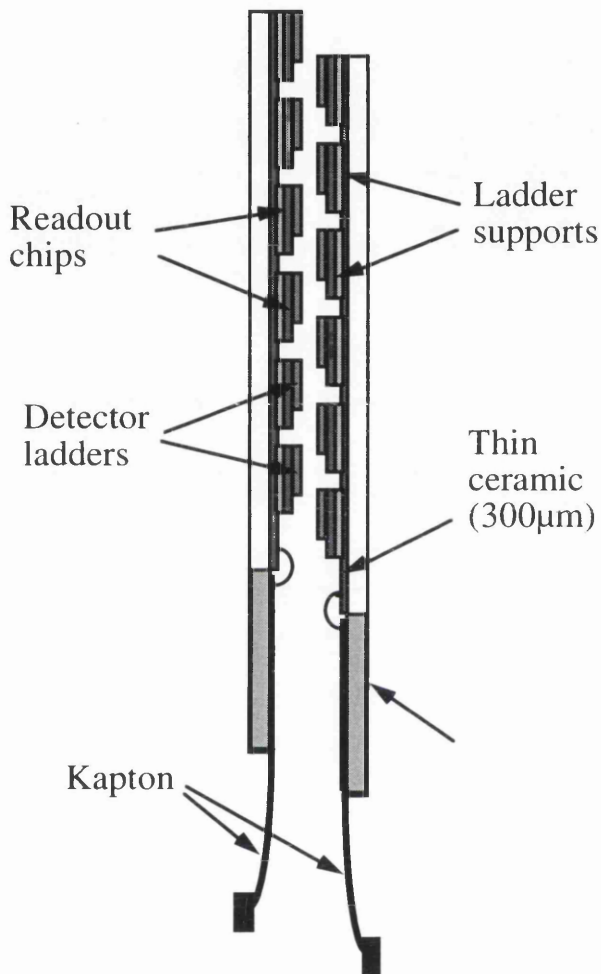
Figure 1-22. Covering of a 5 x 5 cm^2 plane by staggering two separate planes containing , in the case of Omega2, 6 pixel ladders.

The selection of good electronics chips prior to bump bonding and good ladders after bump bonding allowed pixel detectors planes with 3% (Omega2) and 5% (Omega3/LHC1) noisy or dead elements to be produced. An example of the response of half Omega3 pixel plane to a ^{90}Sr β^- source is shown in Figure 1-23.
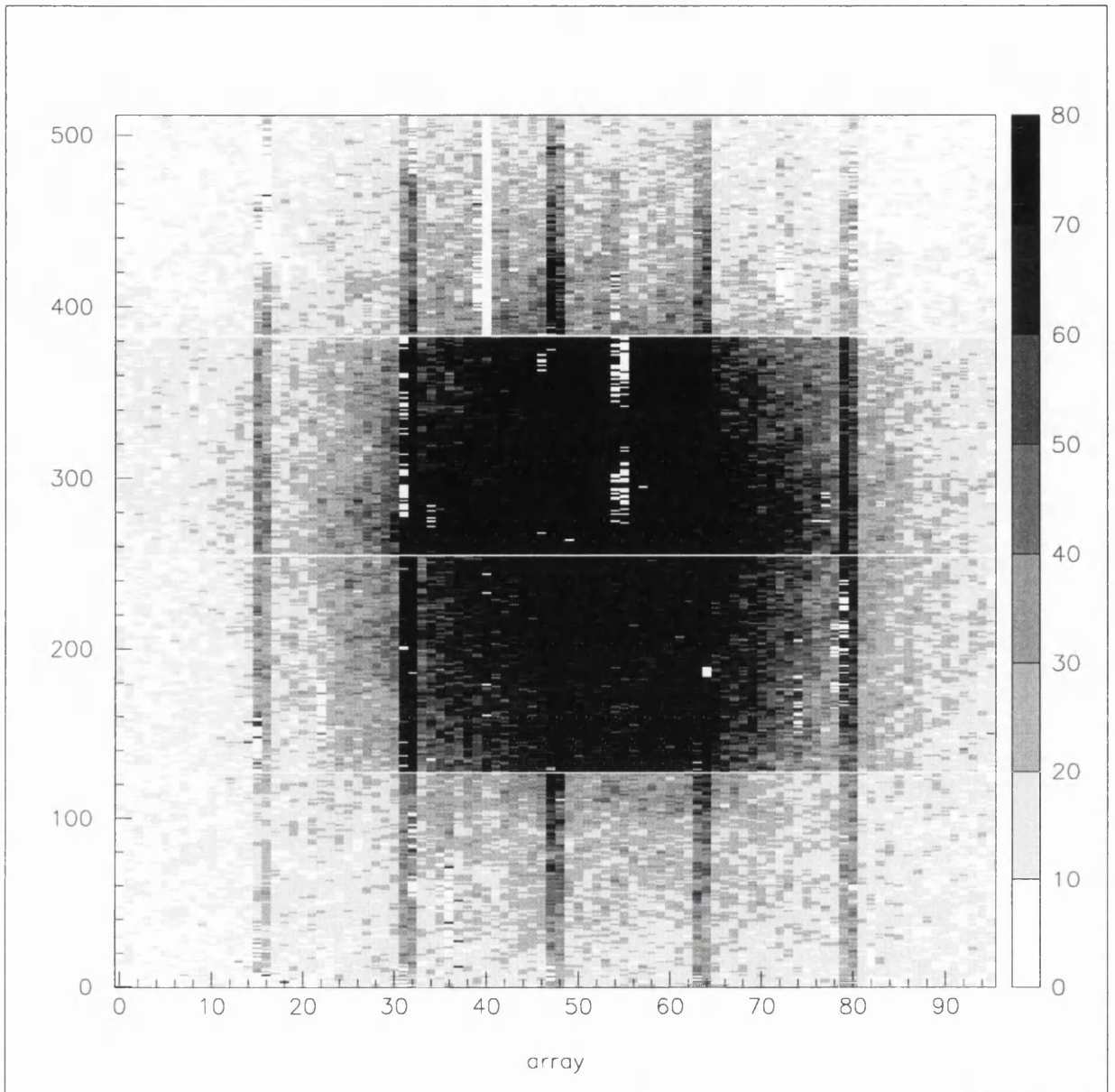
Figure 1-23. Response half Omega3 pixel detector plane. Two of such planes cover an area of 5 x 5 cm^2 for a total of ~100 000 pixels.

BUMP-BONDING TECHNOLOGY

There are essentially two different technologies for flip-chip bonding. The older one based on the IBM C4 process has a fundamental limit in the bump dimension due to the use of a molybdenum mask which is used to define physically the bonding location. In the modern processes a finer pitch can be obtained as the bump boundaries are defined by normal photolithography.

55

Introduced by IBM in 1964 as Controlled Collapse Chip Connection (C4) [64], lead-tin solder bump interconnects formed through an evaporation process were developed to eliminate many of the manufacturing issues associated with conventional wire-bonding, as well as to enhance package performance. The most obvious advantage of solder bumping is the ability to use the majority of the chip surface to interconnect pad sites. At present lead-tin and indium are used for flip-chip bonding, the latter being preferred where heating could be a problem since the indium process can be carried out at room temperature. An alternative gold/tin (80/20 wt%) alloy is also under study for low temperature assemblies.

The two methods for producing solder bumps are through evaporation and plating processes.

Evaporation provides very good process controls and allows a precision in bump height and alloy content as good as 1% across the wafer. The evaporation is limited however to high lead content solders. This process is dependent on the use of a shadow mask and is limited by the mask thickness and the mechanics.

The *electro-plating* process requires a sputtering system, ashing, and photolithography. The system requires a high level of automated controls overall when a good metal composition is necessary for precision and uniformity on the wafer. With newer systems the bump height is controlled to 10% across the wafer and the alloy content to 0.2%. One important advantage of plating is the fact that it can be used to deposit solder of any composition, including eutectic (37/63 weight % lead/tin), which is impossible using evaporation. Plating can handle tighter pitches than evaporation, the latter being limited to 250μm pitch, with smaller bump size. The future requirements for bump bonding are driven essentially by the demands of MCMs (multi-chip-modules) [64][66]. These will require a different approach to back-end processing and a higher level of sophistication in the processing equipment.

The aim of a present study of gold/tin bumps by Alenia [67] is to interconnect two different semiconductors like silicon and gallium arsenide. This is why the "wettable metal" reproduces the Ti/Pt/Au metal sequence of the Schottky metallization in the gallium arsenide detector. The dimension of the bumps is 20μm and the deposition is made at 300 °C [68].

Indium bumps are currently used to interconnect cadmium telluride and cadmium zinc telluride detectors to their silicon read-out electronics. Among others LETI [69] and IMC [70] have developed this technology for compound semiconductor infrared

detectors and tried already to apply their experience to X-ray sensors. The LETI process uses indium bumps of 50μm for this kind of application but the dimensions are related to the pixel dimensions and could be much smaller. The contact between the two wafers with indium is done at room temperature using a compressing force of ~20kg (IMC). After hybridization the air gap between the connections is filled with epoxy to guarantee the mechanical stability of the assembly. The precision in the alignment reached with this technique is ~3μm.

The pixel matrices of the Omega assemblies were mounted using a process developed by GEC-M.M.T. Ltd. [65]. In this process, a via is defined through the passivation layer on the chip surface down to the aluminum alloy metallisation that is employed for interconnection tracks and input-output pads on the integrated circuits. This via is covered by sequential layers of wettable metals, in the case of silicon detectors Cr-CrCu-Cu-Au. The Cr layer provides adhesion and a diffusion barrier between the solder and the aluminum layers, the chromium-copper layer provides 'solderability' and at the same time resistance to solder dissolution, the copper layer extra solderability and finally the gold layer prevents oxidation of the underlying layer upon exposure to atmosphere. The solder commonly used for assemblies is made of a 95/5-lead/tin alloy, liquidus temperature 310 °C.

For the Omega assemblies, however, a lower melting point solder, a 37/63 lead/tin alloy with eutectic temperature 183 °C, was used. The process for the deposition of the solder bumps comprises several steps, after the deposition of the wettable metal on the bonding pads of the electronics chip. This process is normally made on the complete wafer for silicon matrices. The deposition of the solder follows by an electro-deposition process over an area larger than that of the wettable metallisation, using a resist mask. After deposition the solder is reflowed to effect the formation of a well-defined solder bump on the wettable metallisation, the solder Heating of the wafer allows the solder to retract, forming hemispherical bumps as can be seen in Figure 1-24.
The wafer is then diced and the read-out chips can be pre-aligned to the "flipped" detector ones. A precision of ~1 μm in the alignment can be reached, heating the pre-aligned assembly to the eutectic temperature of the alloy, using the surface tension of the fused solder.

The bond diameter obtained was 28 μm for Omega-D and Omega-2 and 22 μm for Omega3/LHC1. The height of the latter is 15 μm and it can withstand a force of 10 mN (1g) before breaking.
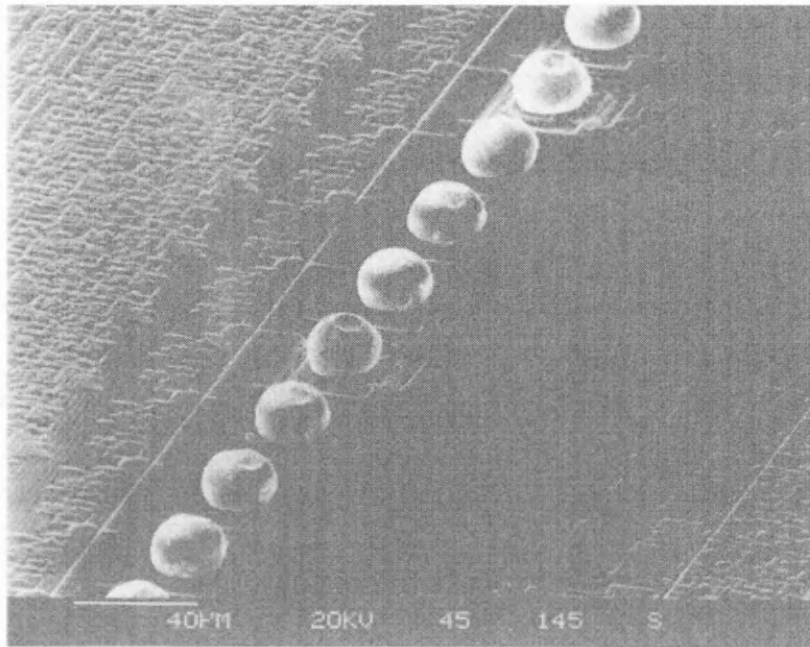
Figure 1-24. A microphotograph of the lead-tin bumps used to interconnect the Omega3 electronics with GaAs and Si detectors. The diameter of the bumps is 22μm.

THE ISPA TUBE

Omega2 and Omega3 pixel detectors were used as multi-anodes in image intensifier tubes. The Imaging Silicon Pixel Array (ISPA) tube[124] is a vacuum-sealed image intensifier which contains a silicon pixel anode instead of a conventional phosphor screen. The tube is a cylinder of 40 mm length and 35 mm diameter. An 18 mm diameter multialkali photocathode, evaporated onto the surface of an optical fiber window for collimated light passage, is viewed at 30 mm distance by the Omega2 or Omega3 silicon pixel matrices.

The photoelectrons converted by the light detecting photocathode are accelerated by the internally applied electric field (25 kV) and bombard the silicon pixel matrix. Each electron hitting the silicon creates 280 electron-hole pairs per kV[130] for a total of 7000 at full applied voltage. Up to the present, tests have been successfully made with γ-rays and β⁻ tracers [130][131].

The spatial resolution is 3 times better than with commercially available position sensitive photomultipliers due to the lower charge spread and the read-out rate is estimated at 400 kHz/cm^2 (chip read-out rate/chip surface). Studies are under way to improve the present anode surface (Omega2 / Omega3 pixel area) by arranging four silicon pixel matrices close to each other inside the same ISPA envelope.

In a monolithic pixel device the detector and the electronics are integrated on the same substrate. The signal processing circuits are placed in potential wells next to the collecting electrodes in order to prevent induced noise in the electronics and cross-talk between adjacent electrodes.

A cross-sectional view of a silicon monolithic pixel detector is shown in Figure 1-25.
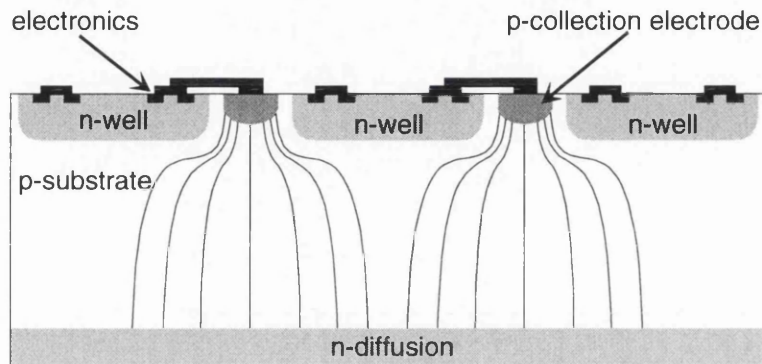
Figure 1-25. Cross-sectional view of a monolithic pixel detector. The electronics and the collection electrodes are processed on the same substrate.

Monolithic pixels can be processed double-sided on a p-type substrate[72] or, more traditionally, single-sided on an n-type substrate [76]. In the first approach the diode junction is formed on the back-side, thus minimising the electric field at the collection electrode when the diode is fully depleted. In the front-side version, the amplifier is housed in a n-well which acts as a Faraday cage. The n-wells also help to shape the electric field in the depleted substrate so as to guide holes created by ionising radiation to the collection electrodes and the electrons to the back-side diode contact. Guard-rings are necessary to assure a correct field shape at the edges of the detector and to prevent surface current flow after die cut.

The performance of a 10x30 matrix with pixel dimensions 125 x 34 μm^2, developed for high energy physics applications is described in [72][73]. The main motivation in using this approach rather than, for instance, hybrid technology in high energy physics applications, is the reduction of material in the detector volume.

The electronics contained in each pixel cell comprises "store" transistors and charge integration transistors with the possibility to sample a reference voltage after applying a reset pulse. This last operation was done to minimize the errors introduced by switching

transients. The transistor currents, modulated by the charge collected in their gates, were read-out sequentially using shift registers.

The X-ray applications are, so far, restricted to mammography [74][75]. Excellent images of mammography phantoms of 0.85 mm are reliably detectable. It has been suggested that 3-dimensional information may be obtained by using multiple sources and scanning of the detector in order to reduce scattering contamination and image blurring due to patient motion.

Some more study is needed, however, before the realisation of a practical device made by this technology. The detector processing is still too delicate to guarantee a good yield. Covering large areas is another problem to solve, together with the possibility of using more efficient materials than silicon for X-ray detection. The last restriction on the use of monolithic pixel detectors is the need to process information locally, an important issue when a large number of channels are present, if only to avoid the need for a huge amount of data to be transferred and stored for off-line processing. In this respect hybrid technology seems a more reliable approach for this type of application.

OTHER TYPES OF PIXEL

The main point of using pixels for any type of imaging is the necessity of an unambiguous high resolution, two dimensional information. Other constraints, imposed by special applications or special environments motivated the research of more specially-adapted structures. These include (a) the combination of large foils of amorphous silicon associated with CsI (Tl) crystals[77] or selenium [78], studied as an inexpensive X-ray detection alternative, (b) a new idea of using micro-anodes across the thickness of a silicon or gallium arsenide wafer [79] to decrease carrier drift lengths and solve radiation hardness problems and, finally, (c) the use of super-conducting Josephson tunnel junctions [80] for high radiation environments. The first two are closest to industrial production and deserve some further comment.

AMORPHOUS SILICON AND SELENIUM

Amorphous silicon and selenium are becoming very interesting for the creation of an image array capable of covering areas as large as 25 x 23 cm^2. The pixel array consists of a matrix of thin film transistors coupled to the Si:H photodiode or Se. In the first case the pixel array matrix needs a converting scintillator like CsI while 600 μm thick

selenium can be used as a direct detector itself. The array requires 30s to read out completely and there is some penalty in the signal-to-noise figure given by the FET transistor, but industrial effort is being applied to find a cheap solution to these problems and, consequently, these two techniques look the most promising short term large area imagers for X-ray detection.

SUMMARY

The ideal detector for imaging applications has to have a high spatial resolution, to cover a large area and to be efficient for the type of radiation used. For medical applications where X-rays are used in a wide energy range direct detection is the preferable technique but, due to limitations in the available high efficiency semiconductor materials, feasible only below 100 keV X-ray energy. Photon counting is moreover preferable if the X-ray source is not monochromatic since the noise performance of the detector is then degraded.

Nuclear medicine, which deals with photons at energies above 100keV, needs other approaches for its detectors, essentially converters before photodetecting devices. With the same type of considerations pixels are preferred to other detectors such as cooled CCDs, and smart pixel sensors are promising substitutes for film plates.

Semiconductors are, in their intrinsic properties, very well suited to the requirements mentioned above. VLSI technology helps as well in this direction and nowadays a wide variety of structures: strips, monolithic pixels and hybrid pixels are available while even more sophisticated detectors are under study to satisfy the extreme requirements of radiation hard environments.

Advantages and disadvantages of the different approaches have been presented. More details have been given about the Omega hybrid pixel family, their structure and the technique used to cover large areas with them as an introduction to the study presented in the following chapters where the Omega electronics chips were used in combination with gallium arsenide pixel detectors and silicon pixel detectors.

CHAPTER 2

A general requirement for room temperature operation of semiconductor material radiation detectors is a relatively large bandgap energy so that thermal generation of charge carriers is minimised. At the same time the material under consideration should have a relatively large average atomic number to increase X- and γ–ray interaction probability. High charge carrier mobilities and long charge carrier lifetimes are also needed to ensure a good charge extraction and minimal effect of position dependent charge collection. Gallium Arsenide is a semiconductor with several material characteristics that are well balanced for such a detector.

This chapter addresses the present status of GaAs both from the material characteristics and from the detector point of view. Some emphasis is given to the influence of the electric field on the material behaviour in samples grown with the Liquid Encapsulated Czochralzky (LEC) method. Near infra-red absorption is used to understand a possible variation of defect concentration in the material in the presence of an electric field and the results are compared with the predictions of existing theoretical models.

GALLIUM ARSENIDE

Gallium Arsenide is a III-V compound semiconductor with atomic numbers of 31 and 33 and density of 5.32 g/cm^{-3} . The bandgap energy is 1.42 eV at room temperature and the average energy required to produce an electron-hole pair is approximately 4.2 eV [81]. The electron mobility at low electric fields can exceed 8000 cm^2/Vs. At fields above 3 x 10^3 V/cm the electron mobility decreases due to the intervalley exchange of electrons from the direct conduction band valley (Γ valley) to the lower mobility valley (L valley), as represented in Figure 2-1. In contrast holes have mobilities near 400 cm^2/Vs. Both electrons and holes have saturation velocities near 10^7 cm/s, however holes need higher fields than electrons to reach this saturation velocity as shown in Figure 2-2 [24]. All these properties affect the performance of detectors made with gallium arsenide and in particular the charge collection efficiency for devices made from semi-insulating (SI) bulk material. Although undoped SI bulk GaAs material has a very low

free carrier concentration (10^6 - 10^7 /cm^3), the measured devices normally behave more like extrinsic materials rather than intrinsic ones. The low free charge concentration and the high resistivity (as high as 10^8 ohm cm) are achieved by the compensation of residual shallow acceptor impurities (like silicon and carbon) by native EL2, deep donor defects. The basic material properties are summarised in table 2-1.

table 2-1 GaAs main properties

atomic number	31,33
density (g/cm^3)	5.32
band-gap energy (eV)	1.42
Energy/ e-h pair (eV)	4.2
mobility e$^-$ (cm^2/Vs)	8000
mobility h (cm^2/Vs)	400
resistivity (ohm cm)	10^8
dE/dx$_{MIP}$ (keV/μm)	0.56 (most prob. val.)
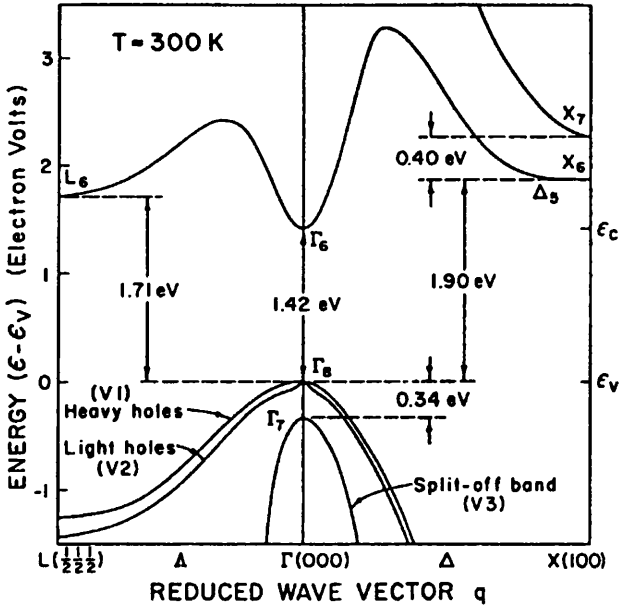
Figure 2-1. Energy variation as a function of reduced wave vector near the valence band maxima and conduction band minima [81].
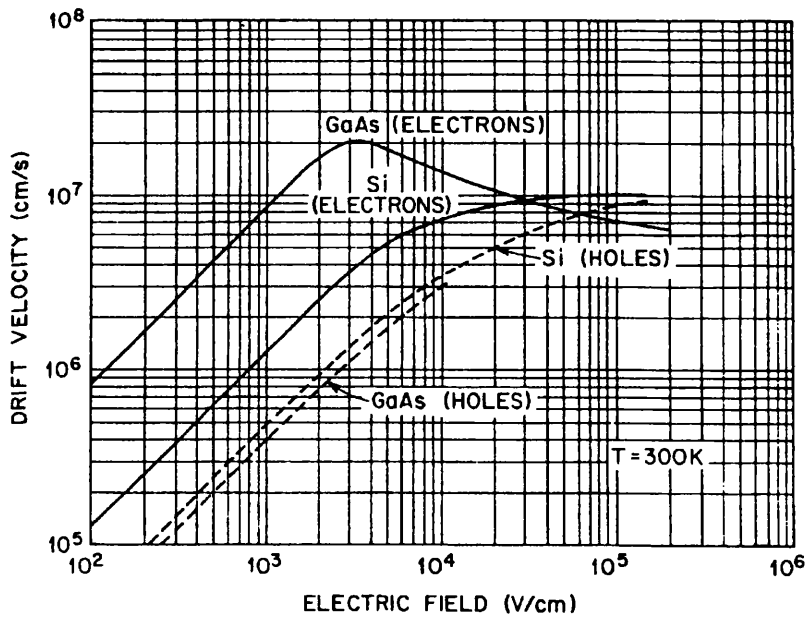
Figure 2-2. Electrons and holes drift velocity as a functions of the electric field in GaAs and in silicon [23].

THE EL2 DEFECT

The EL2 defect is considered to be responsible for the charge collection deficit in detectors made from semi-insulating (SI) gallium arsenide[81][82][83]. It is widely accepted that it is a substitutional, arsenic antisite defect As_{Ga}, where a gallium vacancy is substituted by an arsenic atom as represented in Figure 2-3 [89].
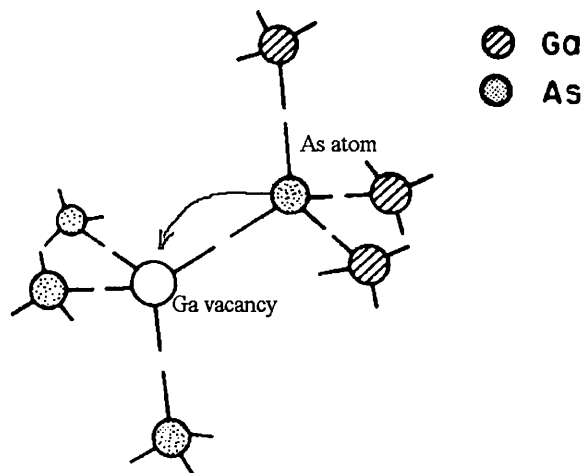
Figure 2-3. Representation of the arsenic antisite defect As_{Ga}.

64

EL2 is a midgap donor in GaAs. Actually in its ground state it is a double donor with energy level at Ec - 0.75 eV [88]. It can exist also in an EL2$^+$ ionised state which has been localised at an energy of Ev + 0.52 eV. EL2$^+$ does not play a major role in the compensation mechanism in semi-insulating (SI) GaAs, but there is experimental evidence [82][83] suggesting that in this state it is acting as one of the most important electron traps in devices made with this kind of material. In Figure 2-4[84], are reported, for example, the charge-collection efficiencies of devices made from different manufacturers as a function of their EL2 and EL2$^+$ concentrations. The influence of the EL2$^+$ concentration in the device behaviour is evident and this triggered the idea of a dynamic monitoring of this crucial parameter under detector standard working conditions. The theoretical motivations and the experimental techniques used will be discussed in the following sections.
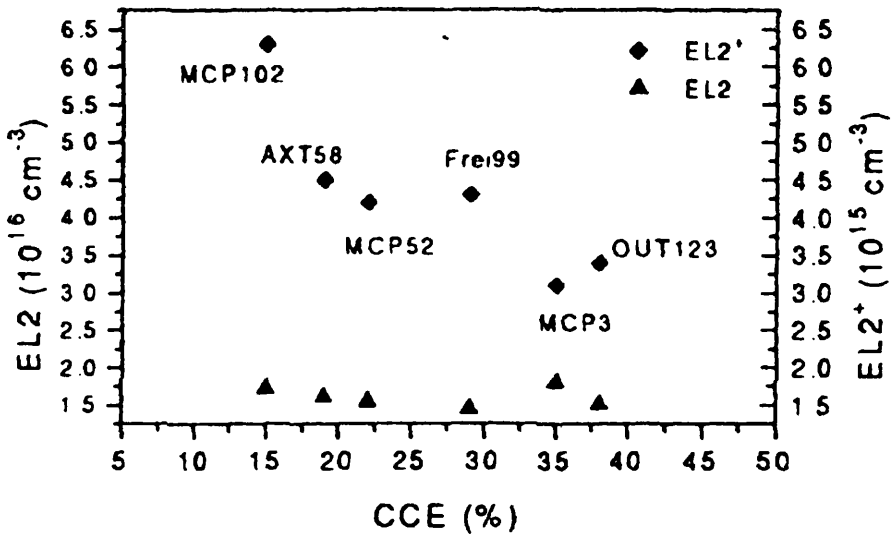
Figure 2-4. Concentration of EL2^0 and EL2$^+$ versus the CCE on sample provided by different manufacturers measured using alpha particles [84].

Defect formation in SI GaAs depends essentially on how the material is grown. Among several different methods of growth of bulk gallium arsenide, the most commonly used is High Pressure, Liquid Encaspulated Czochralski (LEC). The starting material is normally 99.9999 % pure and arsenic loss is inhibited by the molten B_2O_3 cap and about 60atm of high purity nitrogen gas. When the reaction of the Ga and As is complete, then single crystal growth can proceed immediately if a single crystal seed is lowered into the melt.

Usually the crucible holding the melt is lined with pyrolytic boron nitride in order to avoid silicon contamination. The stoichiometry of the melt defines the level of order in the structure of the crystal. Gallium arsenide has a zincblende structure; in this case there are equal numbers of gallium and arsenic ions distributed on a diamond like lattice so that each element has four of the other kind as nearest neighbours and in this case almost perfect stoichiometry is achieved. The stoichiometry has a great influence on the resistivity of the crystals, as can be seen in Figure 2-5.

A larger departure from stoichiometry is possible, however, if the crystal is cooled rapidly. On the arsenic rich side of the graph, the resistivity is determined by the deep donor EL2 concentration, as long as the shallow acceptor concentration N_a is greater than the shallow donor concentration N_d. This is a compensation process by which the bound electrons and holes of shallow donors and acceptors are transferred to deep levels, where thermal excitation to the conduction band is unlikely.
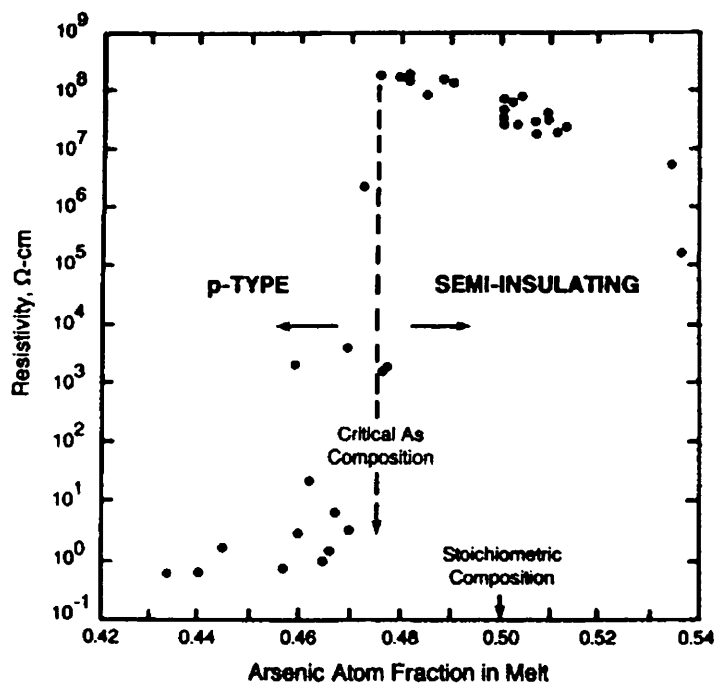
Figure 2-5. Resistivity of LEC GaAs as a function of the arsenic fraction in the melt composition[88]

In arsenic-rich LEC materials the EL2 concentration is nearly always within range of $2x10^{16}$ cm^{-3}. These concentrations are normally higher than those of the electrically active impurities, so that As-rich LEC material is semi-insulating as long as $N_a>N_d$. This

is why the growth of SI GaAs usually begins with an As-rich melt in which N_d is kept very low. In certain cases, like low temperature gallium arsenide (LT GaAs), the material is grown via molecular beam epitaxy (MBE) at 200 °C (instead of the usual 600 °C). This temperature allows a higher concentration of arsenic to be incorporated into the lattice in the form of arsenic antisite (EL2) defects and shows a lower resistivity than the bulk LEC material. The concentration of EL2 can be as high as 10^{20} cm^{-3} and after post-growth annealing at 600-700 °C the material becomes highly resistive. LT GaAs shows remarkably short photo-carrier lifetimes (measured typically in fractions of a nanosecond) and devices made with this material are presently being studied for applications as fast photo-switches.[85].

ELECTRIC FIELD IN SCHOTTKY BARRIER GaAs DETECTORS

Important characteristics of a semiconductor detector like the charge collection efficiency and depletion region thickness depend strongly on the applied bias voltage across the active volume. In particular for SI gallium arsenide devices where the bias voltage is applied through a Schottky barrier and an ohmic contact, the performance was seen to be non-ideal due to the presence of the deep defects which, in their ground and ionised state, act as hole and electron traps.

What has been commonly observed by different groups studying this type of device is that the electric field inside the detector is high enough to ensure good charge collection through the total volume only at very high voltages.

In GaAs, however, there is evidence of the presence of two regions: one at low voltages where the increase in depletion layer width W is proportional to $V^{1/2}$ and a second region at higher bias voltages where the dependence is proportional to V [86], as shown in Figure 2-6[93]. This fact was already unexpected in the case of LEC GaAs considering its intrinsic high resistivity.
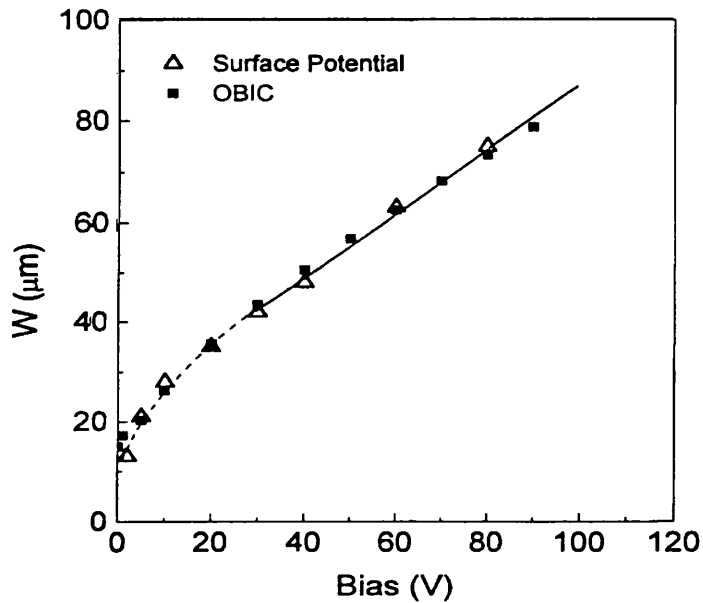
Figure 2-6. Depletion region width as a function of applied bias voltage determined using direct measurement of the surface potential and optical-beam induced current (OBIC) along the edge. 2 distinct regions are clearly visible: one with thickness directly proportional to the applied voltage and the second in which the thickness is proportional to the square-root of the applied voltage[86][93].

Several models have been proposed in an attempt to explain this unusual behaviour. A common consideration among the different approaches is that the presence of the electric field causes a variation in the state of excitation of the deep defects which have their energy levels near the middle of the bandgap. In Figure 2-7 are shown the results of the Monte Carlo simulations of two models.

The first (Figure 2-7 left [91]) calculates from Poisson Equations and the space charge density a field distribution which increases almost linearly from the ohmic contact towards the Schottky barrier. The second one (Figure 2-7 right [92]) predicts a field distribution divided in two regions, as observed experimentally. The model assumes that all donors which are near the Fermi level in the bulk of the detector will be ionised when the band bending is increased by the application of a reverse bias to the Schottky barrier. They will add to the total positive charge leading to a perturbation of the electric field in the depletion region. The shallow donor levels, however, can provide electrons to compensate the ionised deep level defects so that the latter become neutral defects, cannot trap further charge carriers and be the source of perturbation of the electric field.
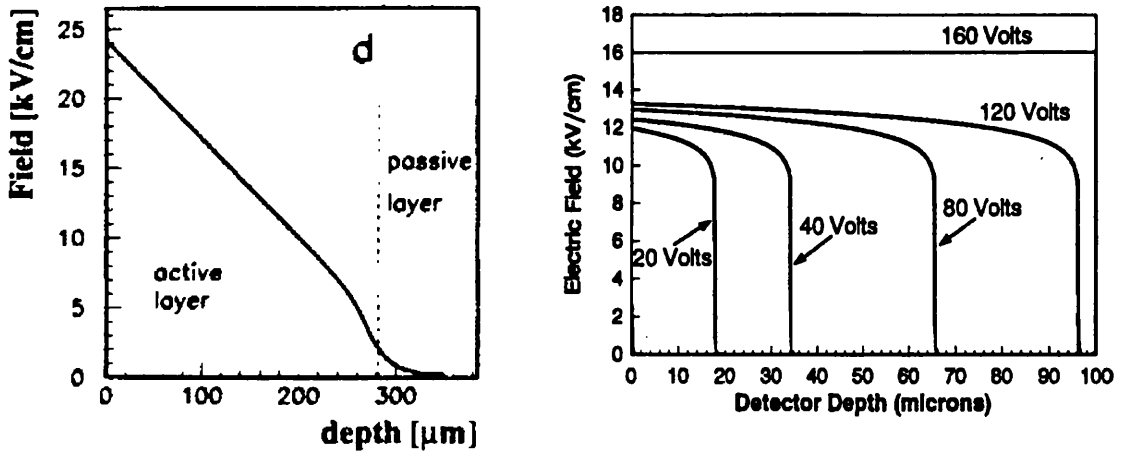
Figure 2-7. Monte Carlo simulations of 2 models which try to explain the electric field behaviour inside Schottky barrier GaAs detectors. [91][92]

This model then is based on the hypothesis of a "quasi-neutral" region resulting from the balance of electron emission rate and EL2 capture cross-section, the two processes possibly assisted by the strength of the applied electric field.

The deep donors, with energy near the middle of the band-gap but just below the Fermi level, are generally not fully ionised at room temperature. The concentration of the ionised fraction can be expressed as:

$$N_{DD}^+ \approx \frac{N_{DD}}{1 + n\sigma_e v_e / e_n}$$

Equation 2-1

where N_{DD} is the deep donor concentration, n is the free electron concentration v_e is the electron thermal velocity, σ_e is the deep donor electron trapping cross-section and e_n is the emission rate.

The emission rate dependence on the electric field is described by the Poole-Frenkel effect [95]. The Poole-Frenkel effect states that for a semiconductor in the presence of an electric field ξ the potential barrier E which an electron must pass to escape from the atom and get into the conduction band is lowered in proportion to the applied field:

$$\frac{e(\xi)}{e(0)} = e^{\xi E / kT}$$

Equation 2-2

69

Apparently in the case of SI GaAs containing EL2s the electron emission rate goes through a minimum between zero and 10^5 V/cm to increase by several orders of magnitude beyond this value. On the other hand, in the presence of an electric field with strength as high as 10^4 V/cm, the EL2 electron capture cross-section increases largely, as shown in Figure 2-8[97].
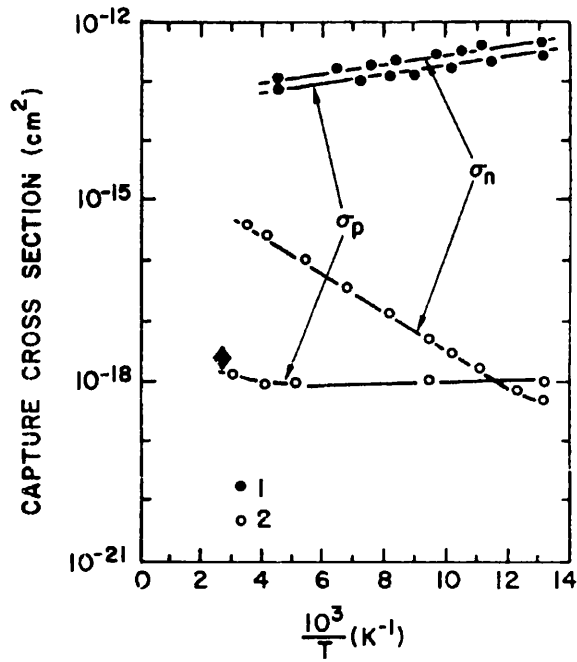
Figure 2-8. Experimental measurements of EL2 capture cross-section in a strong electric field (>10^4V/cm) (1) and in a zero electric field (2). The diamond in the figure denotes the value of the hole capture cross-section [97].

The complete explanation of a definite mechanism of carrier capture in an electric field requires the knowledge of the field dependence of capture in fields less than 10^4 V/cm. Unfortunately this is not available at present. It is an interesting fact, in any event, that in an electric field the electron capture cross-section of EL2$^+$ increases considerably.

If it can be assumed that the capture cross-section is the predominant electric field assisted process for EL2 defects in SI GaAs, at fields as high as 10^4 V/cm, this would explain the neutralisation effect foreseen by the model of reference [92]. The low net positive space charge would explain the flat field observed close to the Schottky barrier and the decreasing of the field further in the bulk due to the higher positive space charge.

If then the capture cross-section dominates, the presence of the electric field would lead to a total increase of the concentration of EL2 in the ground state, or correspondingly a decrease of the concentration of EL2$^+$ due to neutralisation by predominantly electron absorption.

A possible verification of the above mentioned hypothesis is the direct measurement of the EL2 concentration in the presence of the electric field.

Among the different techniques which are normally used for this purpose, NIRA (near-infra-red absorption) and MCDA (magnetic circular dichroism of absorption) measure EL2 concentrations respectively in the ground and ionised state in "as-grown", transparent samples[99][107]. The choice of these techniques, combined with the necessity of a realistic electric field distribution in the material and a transparent medium at the same time, required some study of the geometry of the detector contacts used for the measurement.

EL2 CONCENTRATION MEASUREMENT USING NIRA

Optical absorption spectroscopy presents the most direct information on the electronic defect structure. It is based on the different interactions of the defect with the lattice and this can be measured through the different absorption of the material at different wavelengths. A detailed analysis of energy, amplitude and shape of the transmitted spectrum gives direct information on the electronic behaviour of the material.

Incident radiation, after passing through a certain volume of an absorbing medium, decreases exponentially. The outgoing radiation can be expressed in terms of the incident one as:

$$I = I_0 e^{-\alpha C d}$$
<div align="right">Equation 2-3</div>

where I_0 is the incident intensity, d the thickness of the sample, C is the concentration of the absorbing defect and α is the linear absorption coefficient. In the case of EL2, a very strong correlation between the absorption spectrum and the photo-ionisation cross-section σ_n^0 has been experimentally demonstrated, as shown in Figure 2-9[104], so the absorption spectrum can be used to measure photo-ionization cross-section. σ_n^0 and σ_p^0 represent the EL2 photo-ionisation cross-sections with the centres initially filled with or empty of electrons, respectively.

It is possible to observe (Figure 2-10)that the photo-ionisation cross-section σ_v^0 at 85K, which corresponds to the $EL2^0$ absorption spectrum, consists of three structures with energy thresholds at about 0.9 eV, 1.1 eV and 1.3 eV. and refers to transitions between the EL2 bound state and the three conduction band minima Γ, L and X. Figure 2-10

shows also the photo-ionisation cross-section of EL2 with the centres initially empty σ_p^0 measured at 305K.
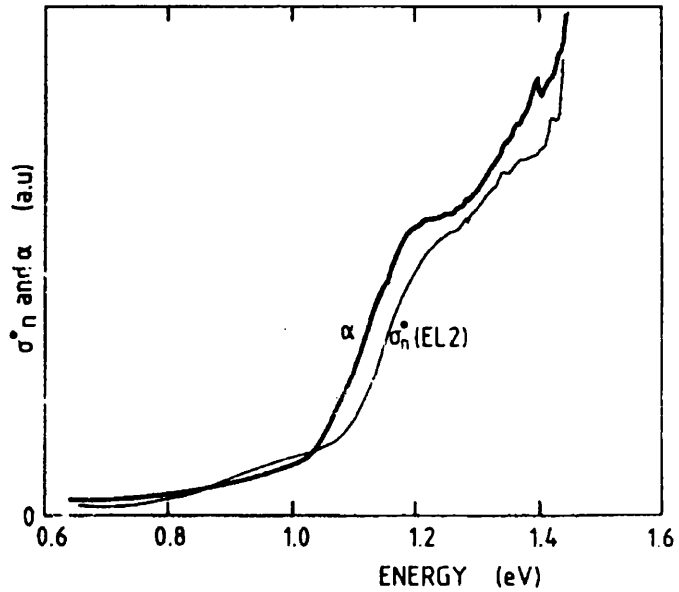
Figure 2-9. Comparison of the absorption spectrum in high purity SI GaAs with the σ_n^0 spectrum [104]
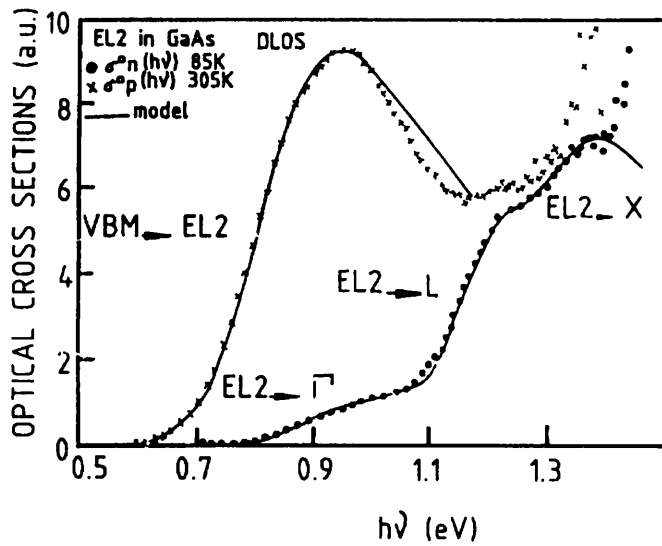
Figure 2-10.Spectral dependence of σ_n^0 (lower curve) and σ_p^0 (upper curve) using Deep Level Optical Spectroscopy (DLOS) technique[105].

A more detailed study of EL2 absorption bands showed that the spectrum has also a broad band at 1.24 eV and this is the energy value which was used by Martin [107] to

calibrate the EL2 concentration from the absorption coefficient, as shown in Figure 2-11, $N = \dfrac{\alpha}{1.182 \times 10^{-16}}$ [cm^{-3}] for measurements at temperatures of 5 K and 300K. This calibration is also used to analyse the data presented at the end of this chapter.
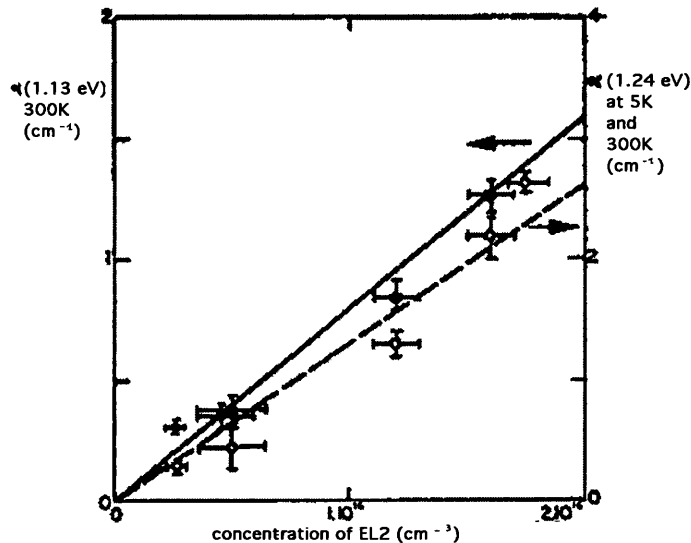
Figure 2-11. Variation of the optical absorption coefficient in undoped n-type materials as a function of the EL2 concentration determined by capacitance methods in the same materials. The measurements are at room temperature (full circles) and 5 K (open circles).[107]

EL2 CONCENTRATION MEASUREMENT USING MCDA

EL2 in its singly ionised state is a paramagnetic level. To determine the occupation of that state, one of the most precise methods is the magnetic circular dichroism of absorption (MCDA)[99][102][103]. This method associates at the same time some attributes of absorption spectroscopy and magnetic resonance spectroscopy. The application of a magnetic field allows Zeeman splitting of degenerate states. Circularly polarised light can be used to probe these new, non-degenerate energy levels and extract data regarding the multiplicity and symmetry of levels involved in the transition.

MCDA is based on the Faraday effect, the presence of optical activity in a sample exposed to a magnetic field coincident with the propagation axis of light. The Faraday effect refers usually to optical activity using linearly polarized light, which can be thought of as a sum of circularly polarized components. If the index of refraction n_+ for right circularly polarized light differs from the left one, n_-, then the components of linearly polarized light traversing a sample will travel at a different speed from each other, namely one will be retarded with respect to the other. As a result the emerging

73

linearly polarized light will be rotated with respect to the incident one. All substances show the Faraday effect in the presence of a magnetic field. In the MCDA set-up the circularly polarised light is provided by a modulator, as will be described more in detail later.

In a region of the electromagnetic spectrum where the sample absorbs light, the index of refraction is expressed as $\hat{n} = n - ik$, where k is the absorption coefficient and $i = \sqrt{-1}$. For right and left circularly polarized light we have $\hat{n}_{\pm} = n_{\pm} - ik_{\pm}$. If in the region of absorption $k_{+} \neq k_{-}$, the sample shows *circular dichroism* . If the circular dichroism is only present upon the application of a magnetic field it will show *magnetic circular dichroism*. Because MCDA is dependent on the absorption coefficient k_{-}, it is non-zero only in regions of the spectrum where absorption of light occurs. MCDA is a consequence of the interaction of electronic energy levels with the magnetic field. This is why it is a measure of the Zeeman effect.

Experimentally the useful information is derived from the intensities of the transmitted polarised beams[99]:

$$MCD = const(I^{+} - I^{-})/(I^{+} + I^{-})$$ Equation 2-4

where the + and - refer to right and left circular polarization.

As a consequence MCD can be defined as a subtraction technique that can be both positive and negative depending on the relative magnitudes of I^{+} and I^{-}.

THE DETECTOR.

The gallium arsenide detector used for the measurement of the EL2 concentration was processed with Schottky barriers on the front and back sides in Freiburg [100]. Depending on the applied bias polarity, one of the two contacts becomes non-rectifying. The metal layers forming the contacts are schematically represented in Figure 2-12. The Schottky barrier is formed after the deposition of layers of titanium, tungsten and aluminium. The semi-insulating substrate, produced by Freiberger [108], has a nominal resistivity of $\sim 3 \times 10^{7}$ Ωcm and a thickness of 602μm.
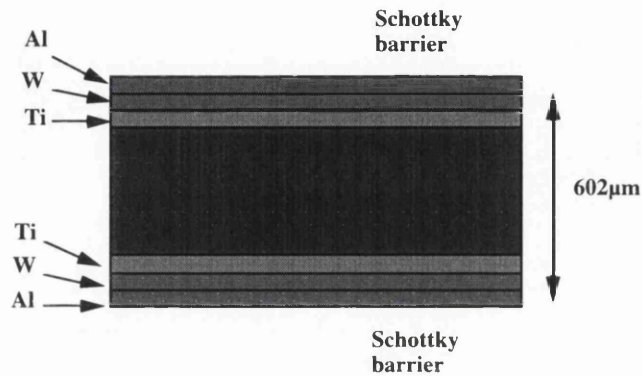
Figure 2-12. Schematic representation of the detector structure. Schottky barriers have been processed on each side of the wafer. Depending on the polarisation, one of the Schottky contacts is forward biased and therefore non-rectifying.

The inter-digitated strip contacts were processed on an area of 5 x 4 mm^2 on the two sides of the detector and the inter-strip distance was chosen to be ~10µm. A sketch of the contacts is shown in Figure 2-13. The bias voltages are applied through long pads perpendicular to the strips on the two edges. No guard rings are used, but the distance from the contacts to the cleaved edge of the substrate (~2mm) is large enough to prevent surface current flow.

Moreover the infrared illumination, perpendicular to the strips, covers a spot of 2mm diameter in the central region of the device, so the electric field distortion present on the edges of the detector should have negligible effect.

75
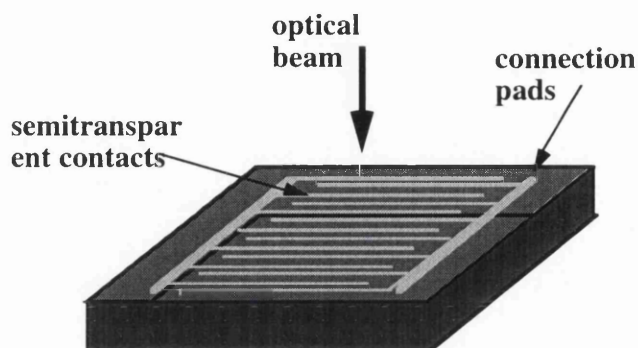
Figure 2-13. Sketch of the strip-like contacts used to obtain a semi-transparent structure. The contacts were processed on both sides of the 602μm thick Freiberger substrate.

THE SET-UP

The detectors used for the test were mounted on a rigid support. Electrical connection between the detector and the external instrumentation was made using ~50μm thick gold wires glued on the two sides of the strip pads with a conductive epoxy normally used on silicon detectors. The amount of epoxy was kept to a minimum to prevent stresses on the material surface due to the different thermal expansion coefficient of the different media. The support was then glued on the sample holder of the cryostat. The detector was aligned with one of the ~2mm diameter holes of the sample holder. One of the holes is normally left free and the transmitted spectrum through it, I_0, used for normalisation. Since part of the measurements was to be performed at low temperature, special care was devoted to the heat sinking of the detector mounting. This was provided by a copper ribbon which was connected from the sample holder to the metal

pads of the vetronite support and in this way in contact with the detector through the gold bonding wire. A picture of the detector is shown in Figure 2-14.
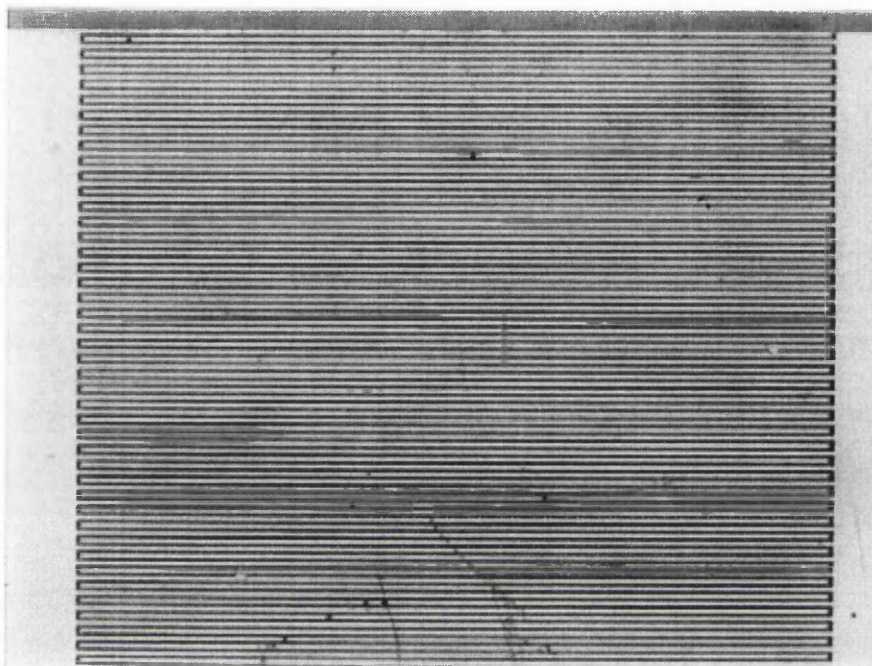
Figure 2-14. Picture of the detector. It is possible to recognise the metal strips which guarantee infra-red semitransparency

THE NIRA-MCDA APPARATUS

The experimental apparatus, installed in the Material Science Dept in LBL, Berkeley [101] is set-up such that both near infra-red absorption and magnetic circular dichroism of absorption can be performed with only minor changes. A block diagram of the optical apparatus is shown in Figure 2-15.
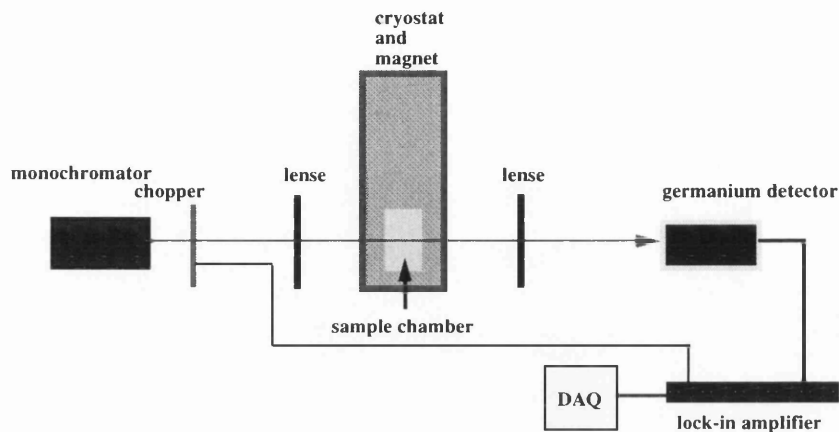
Figure 2-15. Apparatus for infrared absorption measurements. The light from a tungsten lamp is split and one part focused onto the sample. The transmitted light is then collected by a germanium detector. The sensitivity of the set-up is enhanced by a lock-in amplifier associated with a chopper.

For both types of measurement a white light source (a focused 250 W quartz-tungsten-halogen lamp) is dispersed by a monochromator. The monochromatic light is chopped and then focused onto the sample and the transmitted light is finally collected by a germanium detector, cooled to liquid nitrogen temperature. The signal from the germanium detector is finally sent to an amplifier and stored.

The EL2 native defects have an absorption in the near infra-red region, therefore a tungsten halogen lamp with high emission in this region and a grating with 150 grooves/mm are used for NIRA To cut down the influence of stray light, a chopper is used in conjunction with a lock-in amplifier.

For the MCDA measurements(Figure 2-16), circularly polarized light is used.
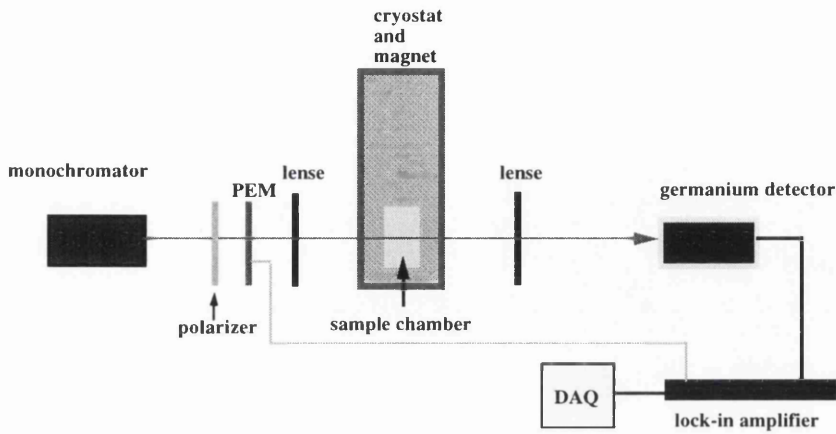
Figure 2-16 MCDA apparatus which uses, instead of a chopper, a linear polarizer followed by a photoelastic modulator (PEM). The PEM is used to produce left and right circularly polarized light

A linear polarizer is introduced after the monochromator and, in place of a chopper, the lock-in triggers on a photoelastic modulator (PEM) at 42kHz. The purpose of the PEM is to produce left and right circularly polarized light from the linearly polarized light by electronically inducing stress-related birefringence. MCDA is used to study the paramagnetic defects EL2$^+$. The temperature for this kind of test is fixed at 1.7K. A typical MCDA investigation utilises three different spectra: (1) NIRA, (2) MCDA at 2T and (3) MCDA at 0T. The 2T spectrum has a strong signal of the EL2 defect while the 0T is subtracted from the 2T one to eliminate system birefringence. The NIRA spectrum is used to normalise the final result.

$$MCDA = \frac{MCDA(2T) - MCDA(0T)}{NIRA}$$

Equation 2-5

The preparation of the cryostat starts with the cooling of the external jacket of the dewar with liquid nitrogen. If the temperature required for the measurements is below 77K another reservoir is filled with liquid helium and the cooling down procedure starts with the injection of liquid helium in the space surrounding the sample chamber. The temperature is continuously monitored by a thermometer connected with a heater which allows external temperature settings.

EXPERIMENTAL RESULTS

Figure 2-17 shows a characteristic I-V curve at room temperature for the detector used in the test. The symmetric response is characteristic of the double-Schottky contact on the two sides of the device. The leakage current at 600V bias voltage, measured at different temperatures, varied between 0.06 μA at 90K and 6μA at 180K. At room temperature the detector at 600V was in breakdown.

CAP1 / 06
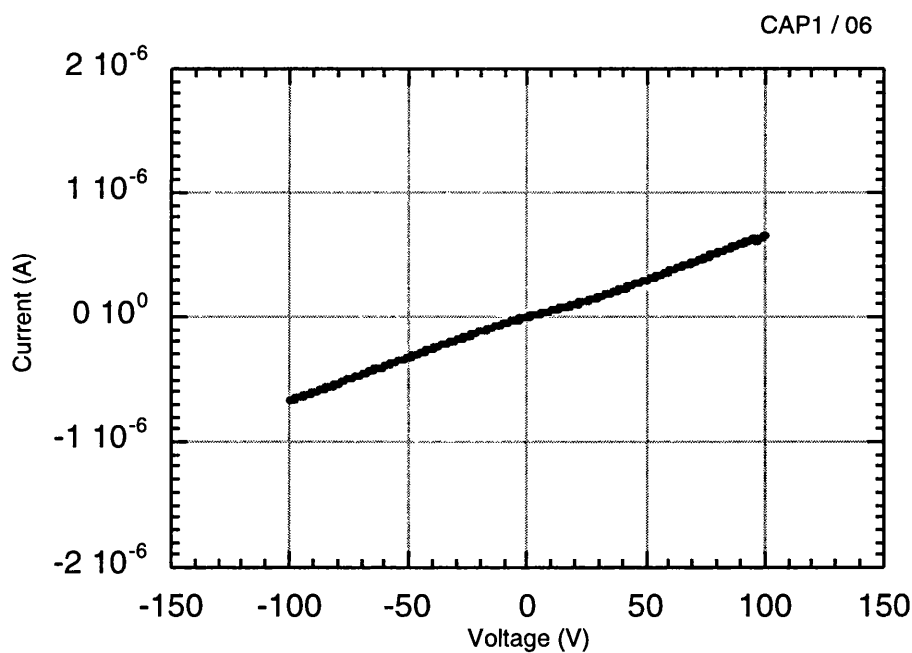
Figure 2-17. I-V characteristic of the sample CAP06. This sample was chosen for the particularly good symmetrical response for the optical tests

80
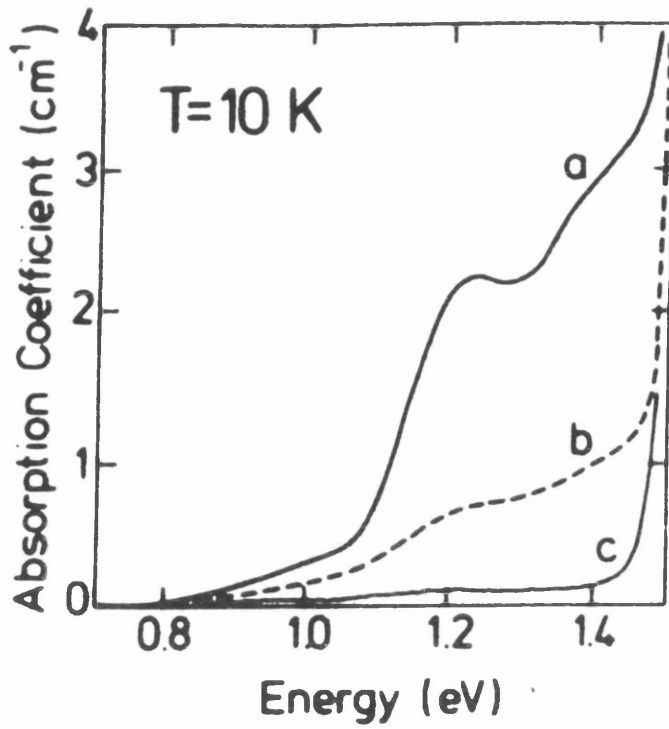
Figure 2-18 a) typical absorption coefficient (a) reported in the literature[107]. The amplitude at 1.24eV is proportional to the concentration of EL2 in its ground state.
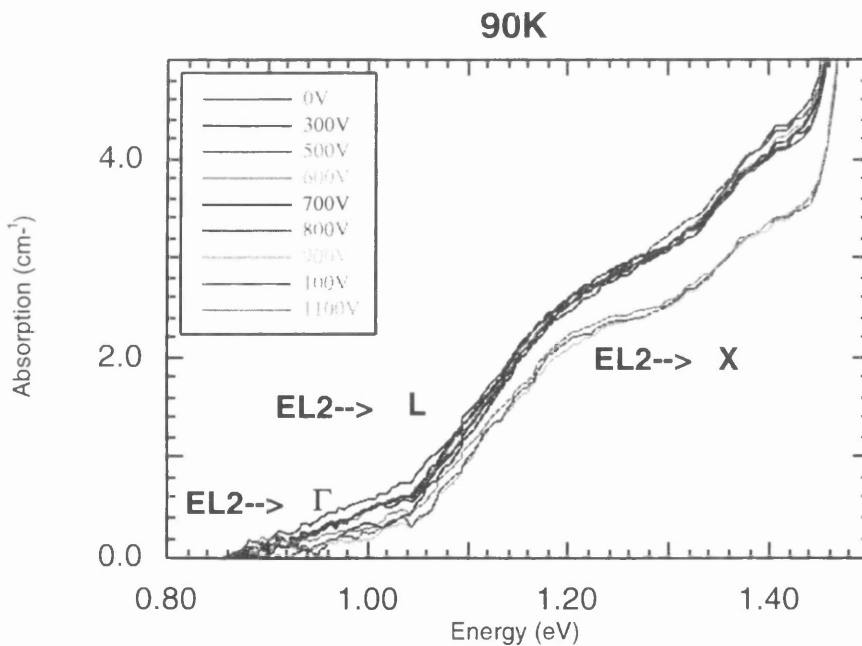
Figure 2-18 b) Spectral absorption coefficient measured at 90K for different bias voltages. It is possible to recognise the optical transitions between the EL2 bound state and the Γ, L and X conduction band valleys as seen in Figure 2-10 at 0.9 eV 1.04 eV and 1.2 eV.
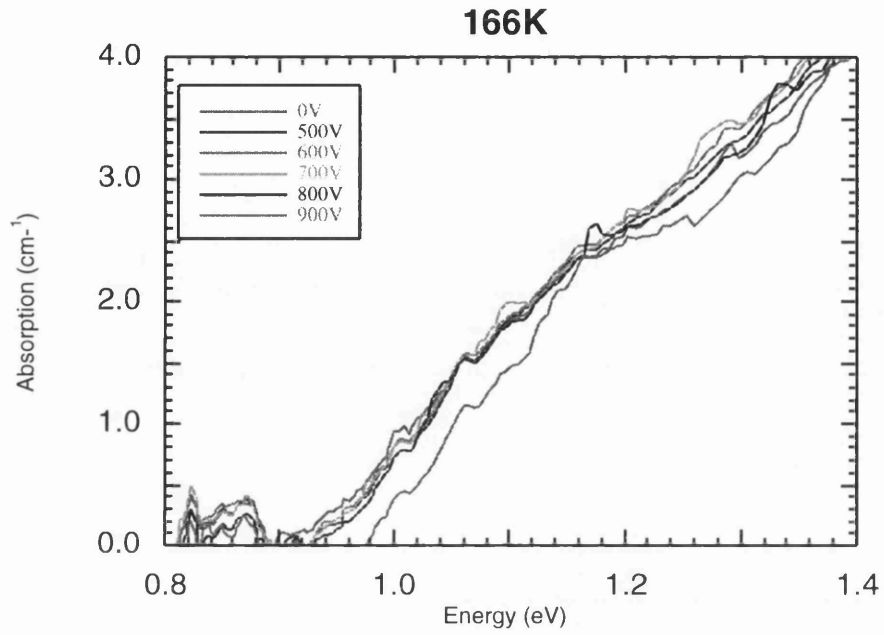
Figure 2-18 c). Spectral absorption coefficient of the GaAs sample measured at 166K for different bias voltages.
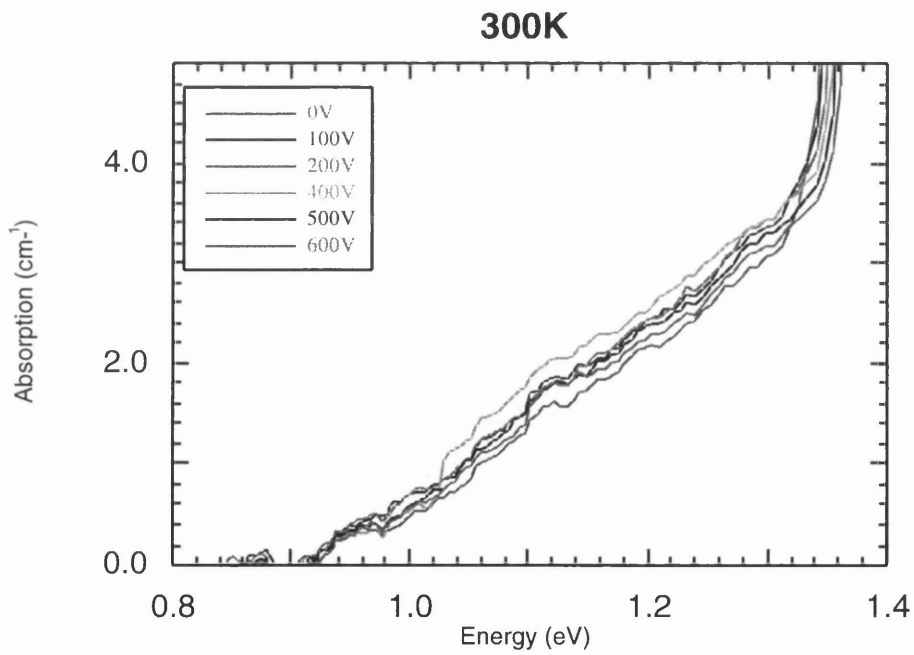
Figure 2-18 d). Spectral absorption coefficient of the GaAs sample measured at room temperature and different bias voltages

Figure 2-18 (a) [107] shows a typical optical absorption spectrum recorded at 10K together with the spectra recorded after photoquenching of the sample for 1min (middle curve) and 10min (lower curve). Photoquenching is achieved by white light illumination of the semiconductor samples at low temperature. In fact illumination at low temperature has the property to excite the defect into a metastable state giving as a result the partial or complete elimination of the absorption signal. The metastability can be recovered after heating of the sample up to 140K for few minutes.

In Figure 2-18 (b), (c) and (d) are shown the optical absorption of the semitransparent sample at different temperatures and different applied bias voltages. The $EL2^0$ concentrations have been measured between 1.8 x 10^{16} /cm^3 and 2.4 x 10^{16} /cm^3. In the absorption spectrum at 90K it is possible to recognise the optical transitions between the EL2 bound state and the Γ, L and X conduction band valleys as also seen in Figure 2-10.

The absorption coefficient for different bias voltages and different temperatures is calculated from Equation 2-1, where I is the intensity of the spectrum at 1.24 eV. The concentration of EL2 defects is then obtained using the calibration of Martin [107] illustrated in Figure 2-11.

The EL2 concentrations as a function of bias voltage at different temperatures are illustrated in Figure 2-19.

The expected variation of deep donor concentration calculated from Equation 2-1, at room temperature, goes from $N_{DD}^{+} = 0.96 N_{DD}$ at low fields up to $N_{DD}^{+} = 0.20 N_{DD}$ for a field of 10^4 V/cm. The above calculations consider a variation in the absorption cross section of 2 order of magnitude, a measured electron density of 4x10^5/cm^3 flowing through the depletion region and a saturated drift velocity of 10^7 cm/s. The variation is not observed experimentally due to detector breakdown at 500V.

The dramatic increase of 5 order of magnitude of the capture cross-section at 90K reported by the literature([97] and Figure 2-8), would imply the number of $EL2^0$ to increase of ~80% for a similar electron density at 10^4 V/cm. However, the measured leakage current at 90K gives an electron density of ~ 3x10^3/cm^3 which results in an expected variation of the ionised concentration from $N_{DD}^{+} \approx N_{DD}$ to $N_{DD}^{+} = 0.97 N_{DD}$, only 3%, comparable with the observed experimental data. An insufficient supply of charge carriers to could then explain the measured results.

The trend in the variation of the concentration with applied bias is however repeatable at different temperatures as shown in Figure 2-19. In particular the EL2 concentration measured at detector breakdown coincide consistently with the one at zero field. Moreover the points measured at fields higher than 10^4 V/cm are supporting the hypothesis of a predominant effect of the electron emission rate, mainly due to impact ionisation[89]. Future measurements should perhaps include the possibility of pumping charge carriers during measurement (e.g. by illumination).
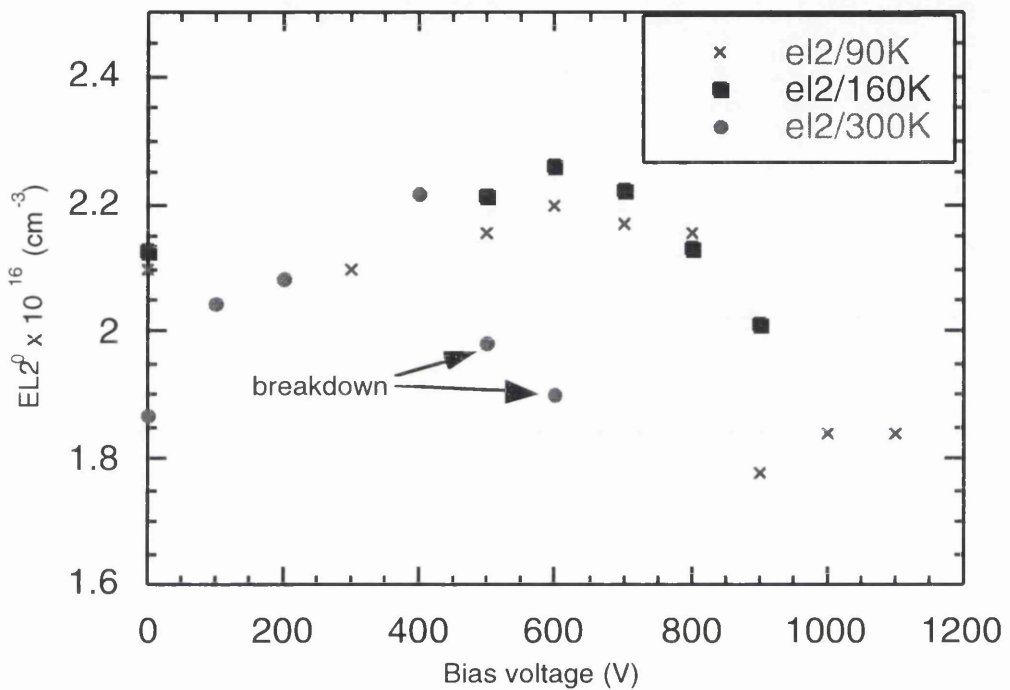
Figure 2-19. EL2 concentration versus bias voltage at different temperatures.

The MCDA measurement of the $EL2^+$ concentration would have been a direct demonstration of the influence of the electric field on these defects. Unfortunately the unusual experimental conditions did not allow the measurement at a complete set of bias voltages and only two points at 0V and 200V are available. The measured $EL2^+$ concentration using Equation 2-3 is 5 x 10^{13}/cm³ and is the same in the two cases as can be seen in Figure 2-20. The electric field at 200V was not high enough to produce any evident change in the $EL2^+$ concentration.
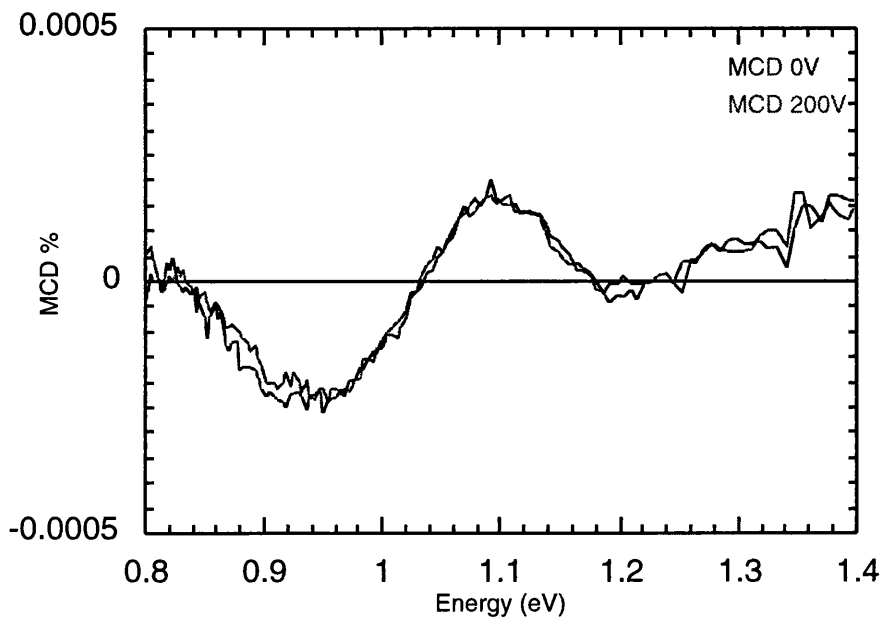
Figure 2-20. MCDA spectra of the LEC GaAs detector at two different bias voltages. The small variation of the electric field was not sufficient to produce a visible variation between the two plots.

SUMMARY

In this chapter a direct measurement of the concentrations between 1.8×10^{16} /cm^3 and 2.4×10^{16} /cm^3 of the EL2 defect at different bias voltages and different temperatures was described. The motivation for this study was a demonstration of the influence of electric field in the concentration of EL2 defects in SI-GaAs devices. The original, purely optical "dynamic" technique was chosen as an alternative to electro-induced techniques. The set-up for infrared tests is normally used with simply polished samples, and the necessity of having a biased device required some study to process semitransparent contacts, in order to have at the same time a uniform electric field on the detector and optical transmission of the infrared spectrum.

The trend of the above results seem to confirm the theory which predicts the presence of a quasi-neutral region in an LEC GaAs Schottky detector after the application of a bias voltage. But insufficient supply of injected electrons, overall at low temperature,

might explain the expected variation of 3% also observed experimentally A direct dynamic measurement of $EL2^+$ using MCDA at the full set of bias voltages was not possible at the present experimental conditions, but further optimisations of the set-up should allow a more comprehensive study of the effects reported here.

CHAPTER 3

In this chapter are reported results obtained by the author by irradiating gallium arsenide pixel detectors bump bonded on the Omega2 and Omega3 electronics with different β^- (^{90}Sr and ^{32}P) and X-ray sources (^{241}Am (60 keV) and ^{109}Cd (22.1 keV)) using phantoms of different contrasts. The results on efficiency tests performed using high energy beams are also discussed, together with autoradiography applications.

In particular, for β^- particle detection there is no advantage in using GaAs and a silicon pixel detector was used instead. For X-ray detection, on the other hand, the inherently high absorption efficiency of GaAs, associated with the self-triggering capabilities of the pixel read-out system, reduced considerably the acquisition time compared with traditional systems based on silicon or emulsions.

The present configuration has been developed for high energy physics applications and therefore is not optimised for X-ray imaging. The last chapter of this thesis will describe the characteristics of a new type of pixel detector, which has evolved for this application, consisting of a 64 x 64 array of pixels each of area 170 x 170μm^2 covering a total area of ~1cm^2.

THE GALLIUM ARSENIDE DETECTOR

The gallium arsenide detectors used for the tests were produced by ALENIA SpA [67]. Surface barrier metal contacts were patterned on 200μm thick, semi-insulating Hitachi substrates using a lift-off technology. A silicon-nitride layer was used as passivation. To make the process compatible with the solder bump-bonding technology, a metal stop layer was deposited on the bonding apertures, to avoid the solder reaching the semiconductor or penetrating underneath the passivation. An 1μm thick electroplated gold layer was grown on the bonding pad to facilitate the adhesion.
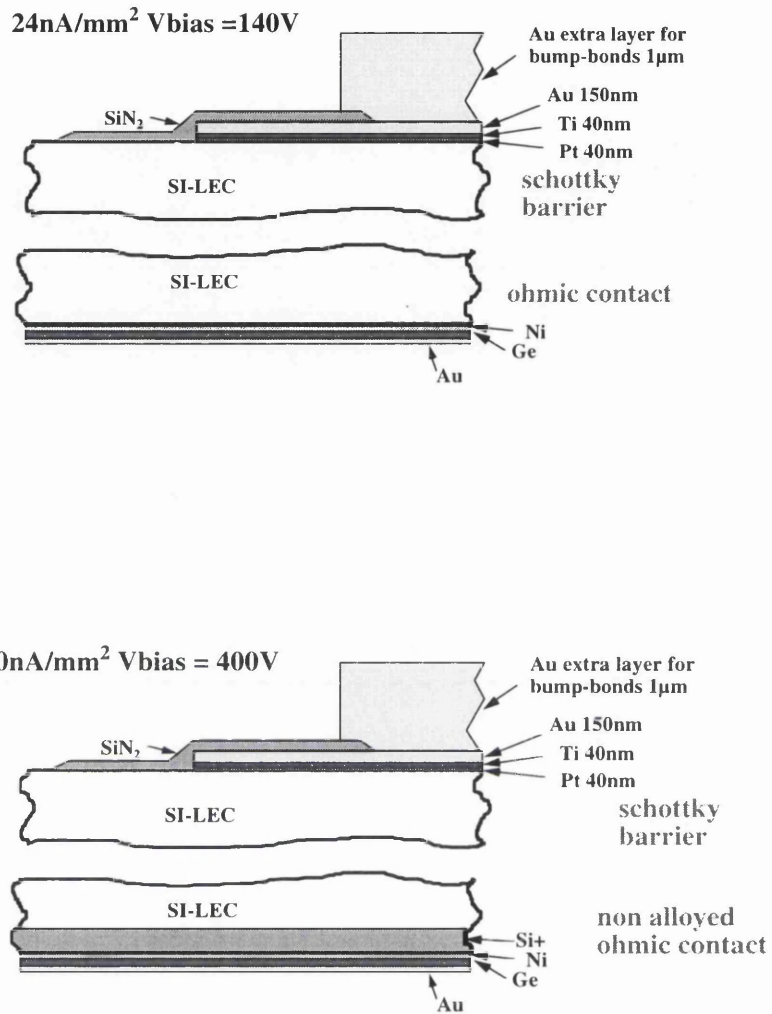
Figure 3-1. The GaAs detector structures, illustrating the standard (top) ohmic contact and the non-alloyed ohmic contact (bottom). The latter incorporated an ion implantation before the metallization to allow higher voltages operation without charge injection breakdown.

In an attempt to enhance charge collection efficiency, different types of ohmic contact were tried. Together with a standard, alloyed multi-layer Ni-Ge-Au contact, we tested a configuration with a Si$^+$ implantation on the ohmic contact (Figure 3-1). This had been reported by other groups to give promising results in terms of energy resolution, (12% at 60keV and room temperature [110]), and charge collection efficiency, (97% at 520V

bias for a 100µm thick detector [109]). The implantation in this case is used to avoid charge injection from the contact and bias voltage limitations due to breakdown.

A microscopic photograph of part of the Omega3 electronics and GaAs detector is shown in Figure 3-2. The sensitive area of the pixel matrix is 81 mm² for a total of 2048 elements divided in 16 columns and 128 rows.
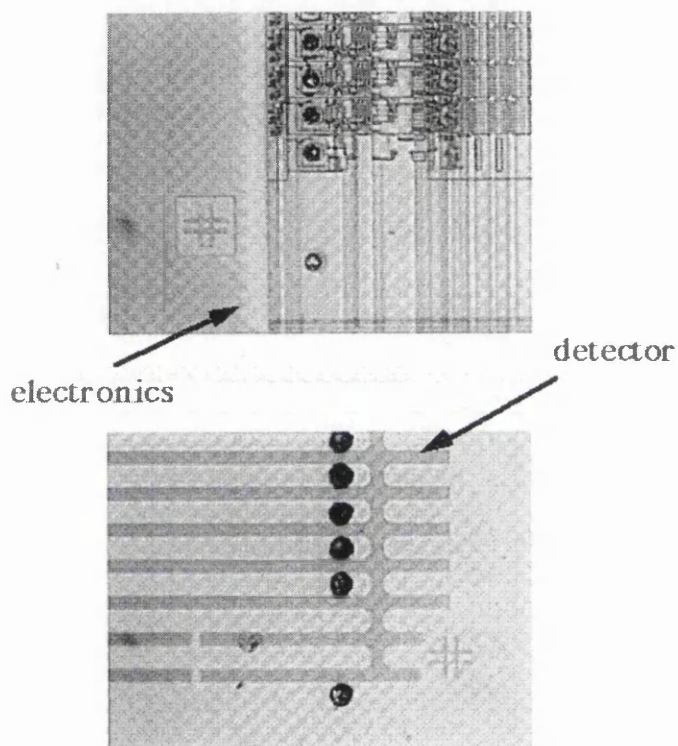
Figure 3-2. Picture of a corner of a GaAs pixel detector matrix and the corresponding OMEGA3 electronics. The black spots are the solder bumps.

THE SILICON DETECTOR

The silicon pixel detector used for the biological tests is made on a standard 300 µm thick high resistivity substrate. The pixels are patterned on the p-type side of a *p-i-n*

silicon structure with a total sensitive area of 38.4 mm² for a total number of 1024 pixels (16 columns and 64 rows) and the detector is mounted on an Omega2 read-out electronics chip.

EFFICIENCY TESTS WITH HIGH ENERGY BEAMS

Beam tests were performed at the H6 extraction line of the CERN SPS North Area. The π^- beam had a momentum of 120 GeV/c and the experimental set-up used for the tests is shown in Figure 3-3. Efficiency and position resolution measurements were made using a silicon microstrip telescope with spatial resolution ~10 µm while data-acquisition triggers were provided by the coincidence output from a scintillator telescope.
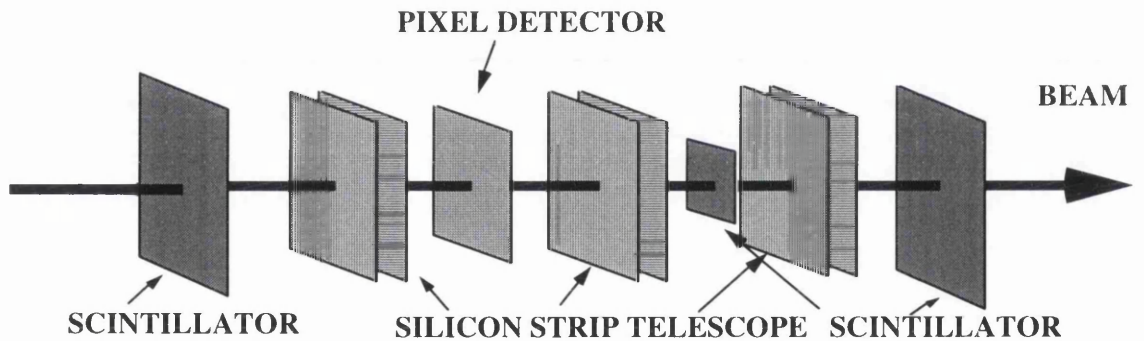
Figure 3-3. Set-up used for the beam-tests

A beam spot of 1 mm² was defined by the overlapping of two 1mm diameter scintillating fibres. This can be seen in Figure 3-4 which shows the beam profile

accumulated with a gallium arsenide device processed with non-alloyed ohmic contact. There are no dead pixels in the beam region and the detector responds uniformly to high energy particles. Figure 3-5 shows the measured efficiency curve as a function of the comparator threshold of the pixels.
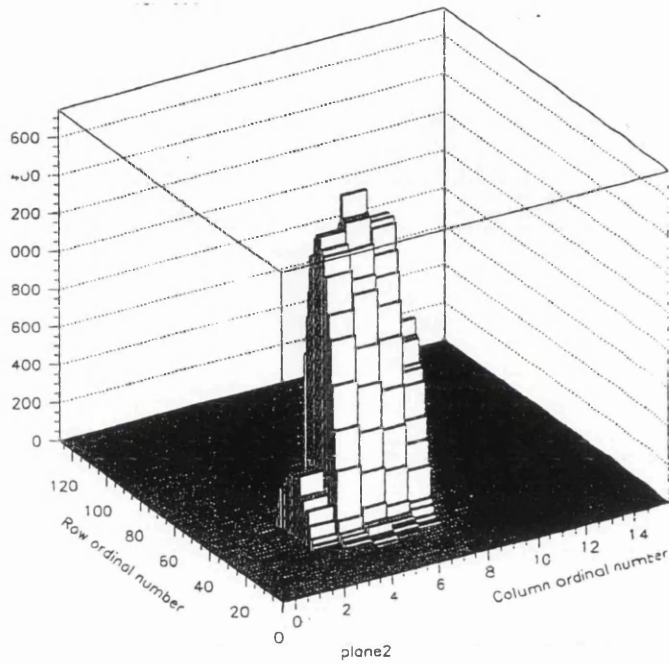
Figure 3-4. Beam profile measured by a gallium arsenide pixel detector matrix.
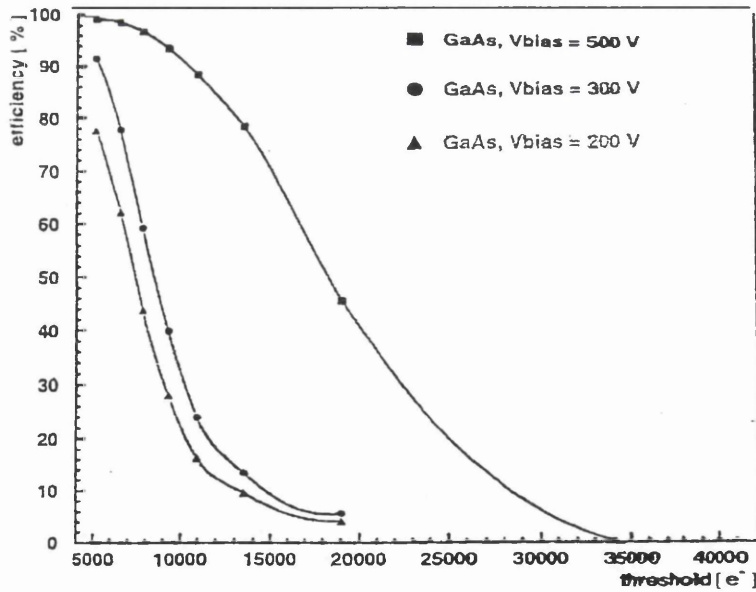
Figure 3-5. Efficiency versus comparator threshold at different values of the bias voltage.

The detection efficiency of the 120 GeV/c π^-, relative to that of the telescope microstrip detectors, is more than 97% in the plateau region at high bias voltage, demonstrating the better charge extraction of this new type of device [109][111].β^- AND X-RAY

SOURCE IMAGES

Images were taken using radioactive sources: ^{90}Sr (1.2MeV end point energy β^-) ^{241}Am (60 keV X-rays) and ^{109}Cd (22.1 keV X-rays) the latter energy close to that used in most radiological applications.

IMAGING SET-UP

Figure 3-6 shows a sketch of the β^- and X-ray imaging set-up. The radioactive sources are placed at approximately 10 cm from the detector, to minimize shadow effects, and phantoms of different shape and thickness were placed directly on the back side of the GaAs detector. The processing of the ohmic contact of the 200 μm thick GaAs detector used for these tests is traditional, without ion implantation on the back-side. The working bias voltage is 100V which does not allow full depletion, but optimises the response of the pixel matrix in terms of uniformity and minimising the number of noisy pixels.

The noisy pixels originated from the high leakage current of the detector at high bias voltages. Although the Omega3 read-out circuit provides some leakage current compensation (~10 nA/pixel), this did not function properly in this version of the electronics because of a circuit design error which was subsequently identified and corrected in the new Omega3^I design version.
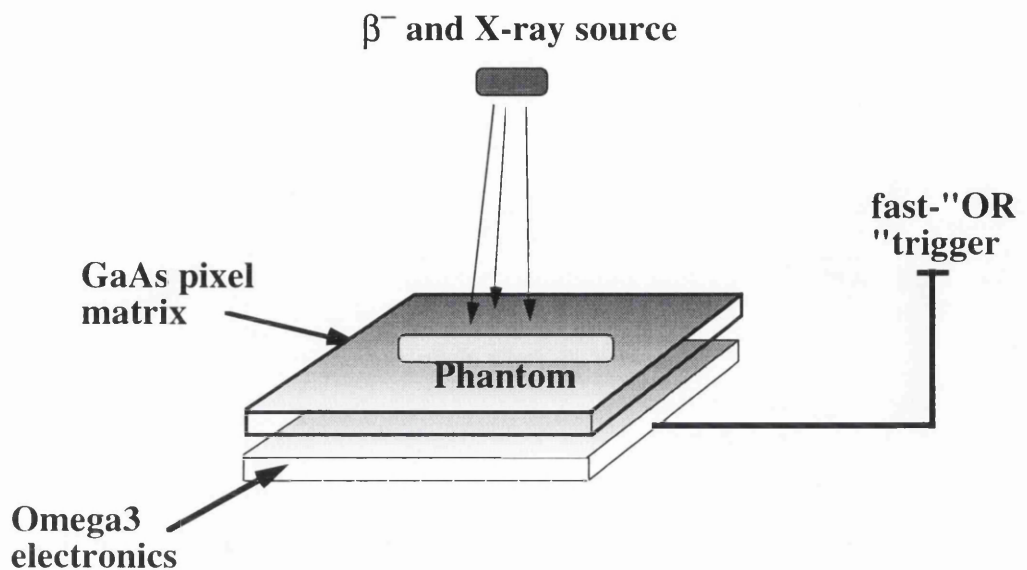
Figure 3-6. Set-up for β· and X-ray imaging. A semi-insulating gallium arsenide pixel matrix, bump-bonded to Omega3 electronics, is irradiated by different radioactive sources. An internal, fast 'OR' (F.O.) is used to trigger the system.

Figure 3-7 shows a steel wire of 500μm diameter shaped as an 'omega' and irradiated with ß⁻ from a ⁹⁰Sr source.

The accumulation of counts per pixel obtained with the absorber in position was subtracted from the corresponding numbers without absorber, taken under identical conditions of exposure. The result is a positive image of the wire. No cross-talk between neighbouring pixels is present at this comparator threshold setting and the percentage of noisy pixels is less than 5%.
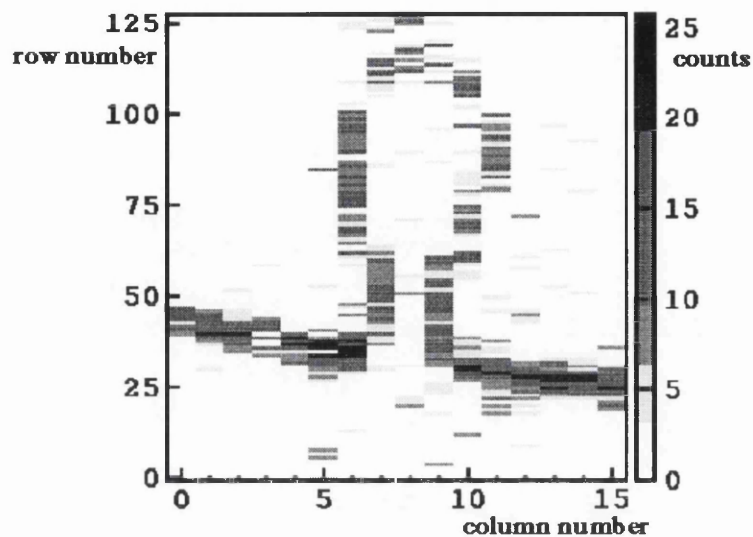
Figure 3-7. Image of a 500μm diameter steel wire exposed to a ^{90}Sr source. The counts per pixel accumulated with the wire in place have been subtracted from the image of the source to produce a positive image. The electronics threshold was fixed to 5000e⁻.

Figure 3-8 also shows the image of a steel wire, this time 1mm thick, illuminated with a ^{90}Sr β⁻ source (left) and ^{109}Cd 22.1 keV X-ray source (right). At the bottom of each image is shown the projection of the number of counts along the column axes, the average of which is used to calculate SNR and SCR using the relations :

$$SNR = (n - n') /(n+n')^{1/2}$$

$$SCR = 2(n - n') / n+n'$$

Equation 3-1

where n and n' are, respectively, the average number of counts per pixel in the background region and in the target region.

The β^- source image was obtained with 500 000 fast-"OR" triggers, giving a SNR= 17.4.[112]
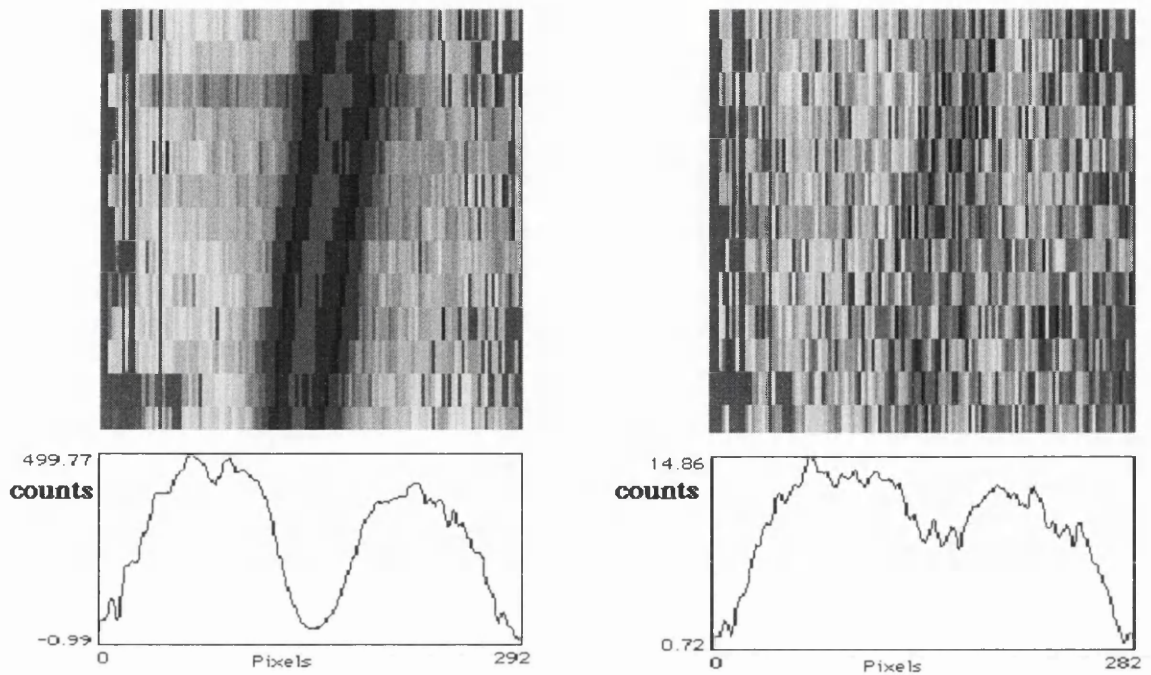
Figure 3-8. Image obtained with a 1mm diameter steel wire irradiated with a ^{90}Sr β^- source (left) and a ^{109}Cd X-ray source (right). The comparator threshold used corresponded to a signal of 5000e⁻ and the number of fast 'OR' triggers was 500 000 and 50 000 respectively. The lower part of the picture shows a projection of the number of counts in one direction. The calculated S/N is 1.3 and the S/C is 27% for the X-ray source.

The X-ray source image was obtained with 50 000 fast-"OR" triggers. The average number of counts per pixel detected in the background region was ~14 and in the target region ~8, giving a SNR = 1.3 and a SCR = 27%. Despite the low statistics and the threshold which was set just below the 22.1 keV K_α peak from the source, the wire is distinguishable from the background, demonstrating the high sensitivity of the counting pixel system. The data in both images have not been processed and correspond to the accumulated raw data without any noise subtraction or filtering.

APPLICATION TO BIOCHEMISTRY

With a similar system (Figure 3-9), the possibility of detecting organic materials labelled with radioactive tracers for autoradiography was also investigated. In this type of measurement the sensitivity of the detector and the absence of noise are the main figures of merit due to the low sample emission rate and the long exposure time needed to collect an image. For these measurements both GaAs and Si pixel detectors were used, bump-bonded with the Omega3 and Omega2 read-out chip respectively.
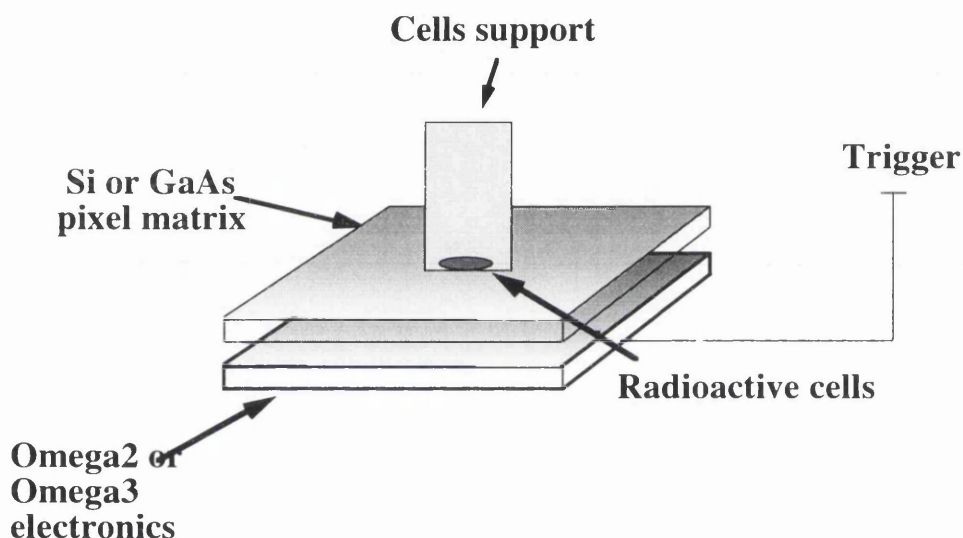
Figure 3-9. Set-up used for autoradiography. Radioactive cells housed in a plastic cylinder were placed on the back-side of the silicon or GaAs detector.

For the auroradiography tests we used cultured human mammary epithelial cells which were harvested from stock culture flasks and seeded on the 3μm thick mylar bottom of a cylindrical container. The cells grow attached to the mylar surface in their culture medium, labelled with the ß⁻ emitter ^{32}P. The ^{32}P radionuclide has a half life of 14.3 days, maximum beta particle energy 1.7MeV and average emission energy of 0.695 MeV. For the latter energy the range in silicon is ~ 1.5mm [113]. After incubation the non-incorporated radioactive material was removed. Following washing and drying,

clusters of labelled cells were present at the bottom of the container. The glass cylinders were put on the detector with the mylar surface in direct contact with it.

Cell samples with different concentrations were imaged and the count rate compared with a liquid scintillator counter, showing a very good agreement. The noise limit of the Si system was measured to be less than 10^{-4} cps mm^{-2}, allowing a linear response with sample activities from 0.005 nCi to 0.5 nCi. Similar results were obtained with GaAs. In Figure 3-10 are shown the image of a sample containing a cluster of cells with radioactivity of about 0.4 nCi. The GaAs detector was the same used for the contrast measurements and the exposure time was ~150 minutes for both the silicon (left) and GaAs (right) detectors[114].
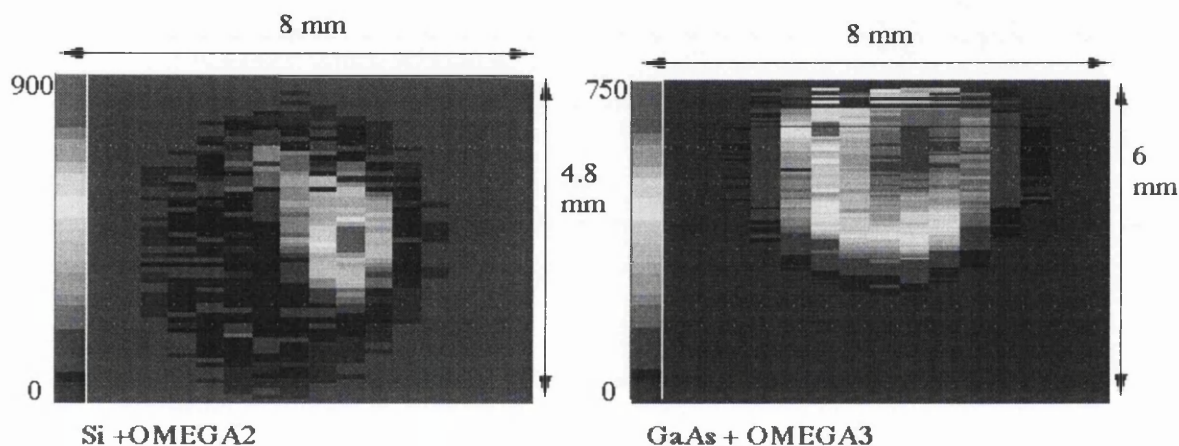
Figure 3-10. Image obtained with a Si+Omega2 electronics detector (left) and GaAs+ Omega3 electronics (right), of a sample containing a cluster of ^{32}P labelled cells with radioactivity of about 0.4 nCi. The exposure time was 150 min.

DNA SEQUENCING MEASUREMENTS

Samples of DNA restriction fragments were treated in the biochemistry laboratory in the Ecole Polytechnique Federale de Lausanne, measured with a standard radiographic

film and a phosphor imager [116] and then transported to CERN for a comparative test using a silicon pixel detector mounted on Omega2 electronics. The size of the samples matched as closely as possible the geometry of the detector and a full area of 1.6 cm x 2.5 cm was measured, scanning the sample over the detector with the use of a micrometer. The acquisition system was modified to stop automatically after a fixed amount of time in order to normalise the exposure conditions of the different regions of the sample (Figure 3-11).
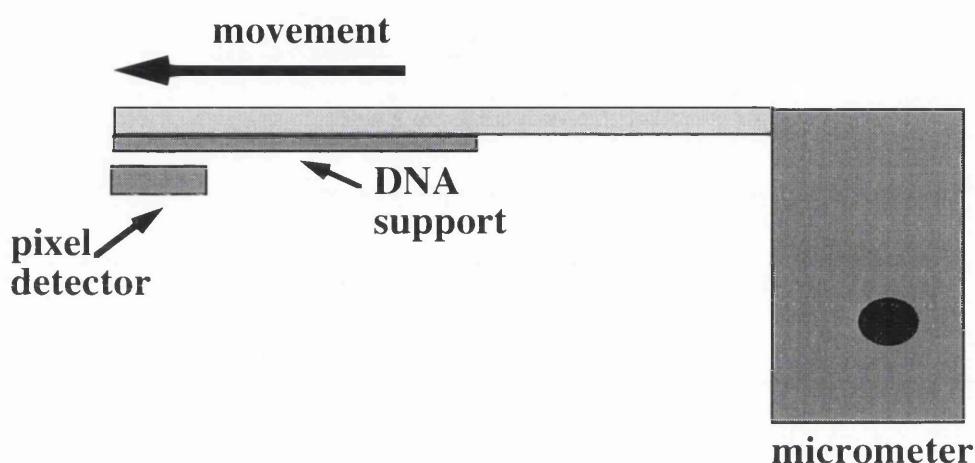
Figure 3-11. Set-up for the DNA autoradiography. The DNA support was shifted by a micrometer on the top of the pixel matrix. A complete DNA sequence required 5 movements of the DNA support.

The DNA sequences were prepared using the so called "blotting technique", which is based on the hybridization of nucleic acids DNA and RNA.

If DNA dissolved in water is heated to 100 °C or exposed to a very high pH (>13), the pairs of complementary bases which normally link the two filaments of the double helix break and the double helix rapidly dissociates into two filaments. This process is called DNA "denaturation" and was considered irreversible for many years until reversibility

was demonstrated in 1961[113]. This process is known as "renaturation" or "hybridization" of DNA and it is possible if the separated DNA filaments are kept for a long time at a temperature of 65 °C. Similar reactions are possible between two chains of nucleic acids DNA/DNA, RNA/RNA or DNA/RNA, under the condition of "complementarity" of the nucleotidic sequence.

The measurement of the number of copies of a specific gene in a DNA sample is done by the hybridization of the DNA with a "probe" filament marked with a radioactive or chemical tracer. The hybridization speed is proportional to the quantity of a certain DNA sequence in a mixture of different sequences. The hybridization is so sensitive and selective that it is possible to identify complementary sequences present even in very low concentrations, even at the level of one molecule per cell. In this way it is possible to determine how many copies of a particular DNA sequence are present in a cellular genome.

The DNA probes are often used after gel electrophoresis to identify those nucleic acid molecules which are completely or partially complementary to the probe sequence. The RNA analysis is called a "northern blot". The RNA molecules are separated by gel electrophoresis according to their dimensions where the shortest segment migrates fastest in the gel. The hybridization with DNA probes is then carried out after transferring the RNA segments on to a nylon foil blotting. Afterwards the nylon foil is left in a solution containing the marked DNA probe[10].

Figure 3-12 shows schematically the procedure for the detection of a DNA sequence. In this case it is a DNA/DNA hybridization which is normally referred to as a "southern blot". The nucleotidic sequence is determined after cutting the DNA to sections of different lengths using "restriction enzymes". Using again the blotting technique, denaturated restriction fragments are separated by gel electrophoresis, transferred onto nylon foils and exposed to the probe. The complementary DNA sequences will hybridize with the marked DNA and are afterwards identified using an autoradiographic detector.

In the sequences we measured, the DNA probe was labelled with ^{32}P which, as for the previous autoradiographic test, is well suited to our silicon and gallium arsenide pixel detectors.
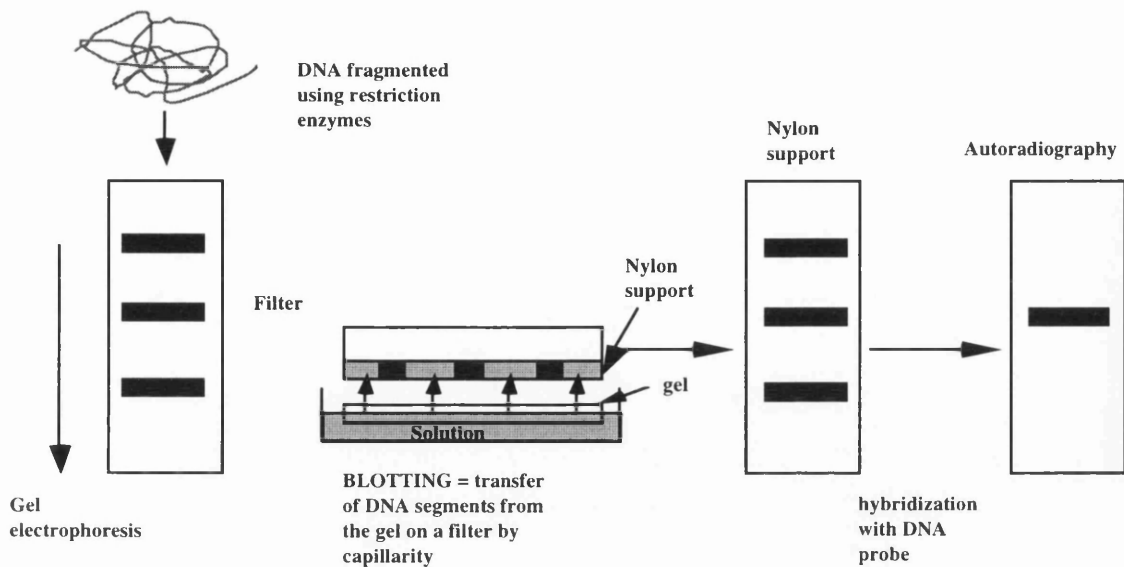
Figure 3-12. Schematic representation of the "southern blot". DNA sequences are reconstructed after hybridization with DNA probes. The separation of denaturated DNA is made by gel electrophoresis and the sequence is then transferred onto a nylon plate by capillarity. In the case of radioactive probes the reconstructed DNA is then visualized with an autoradiographic radiation detector.

Figure 3-13 shows the response of a DNA sequence measured with three different methods. The first employed a commonly used X-ray film, the second picture was made using a phosphor imager[117] and the third a self-triggered silicon pixel detector. The three images required different exposure times: 40 hours for the X-ray film, 20.5 hours for the phosphor imager and 6 hours per scanned slice (5 in total) for the silicon pixel detector.

The spatial resolution, defined as the full width at half maximum of the image generated by the signal from a source of infinitely small dimension, depends strongly on the thickness of the detector. Simulations of the response of an 8mm long source of negligible width have shown a FWHM of ~660μm for the 'point spread function' in the case of a 300μm thick silicon detector. The FWHM can be reduced to ~520μm for a 150μm thick detector.

The direct comparison of the 3 pictures required some image processing. Both the phosphor-imager and the X-ray film images had to be digitised by a scanner and magnified, therefore their quality should be evaluated critically.

X-RAY FILM
TOTAL EXPOSURE
TIME **40H**

PHOSPHOR IMAGER
TOTAL EXPOSURE TIME
20.5H

SILICON PIXEL DETECTOR
TOTAL EXPOSURE TIME **6H**
(5 images)
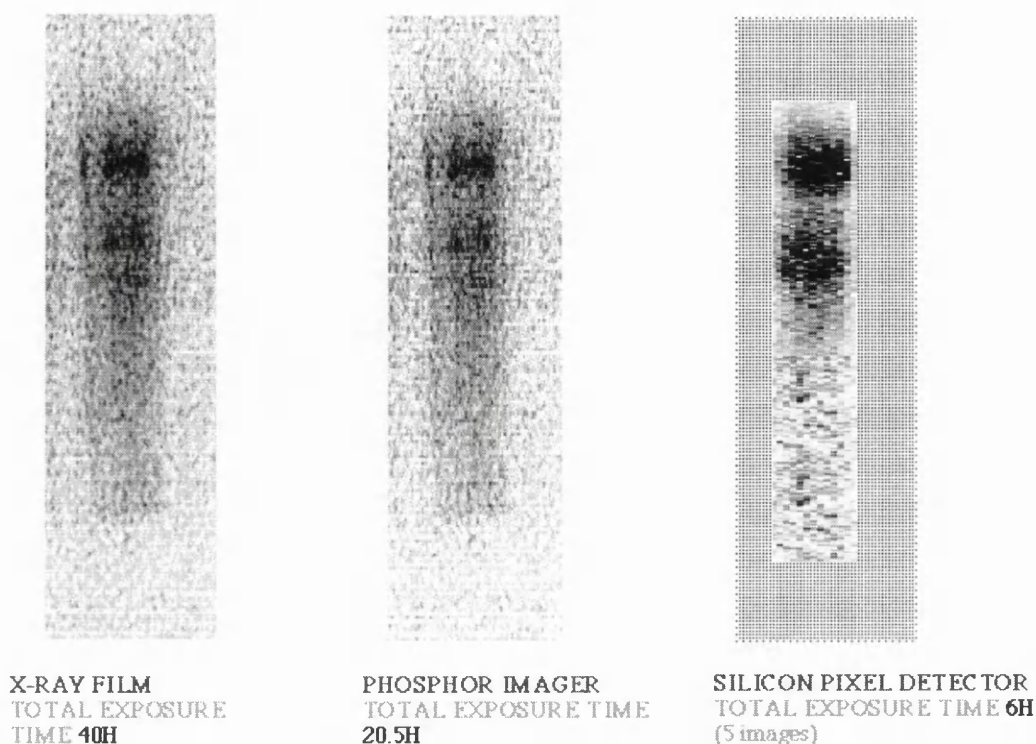
Figure 3-13. The same DNA sequence imaged with three different methods. The X-ray film required an exposure time of 40 hours while 20 hours were needed for the phosphor imager and 6 hours accumulation time per slice (five in total) for the silicon pixel detector. The thickness of the different detectors goes from ~20µm for the film emulsion to ~500µm active layer in the phosphor imager and 300µm thickness for the silicon detector.

Figure 3-14 shows the linear response of the silicon pixel detector. The same detail of the DNA sequence was exposed for different times and the total number of counts detected is plotted in Figure 3-14 b).

The linearity and sensitivity of our system are very good due to the almost total absence of detector noise at the 15 000 e⁻ threshold used for these measurements. It is interesting to note that the DNA fragment is already clearly visible after only half an hour exposure time.
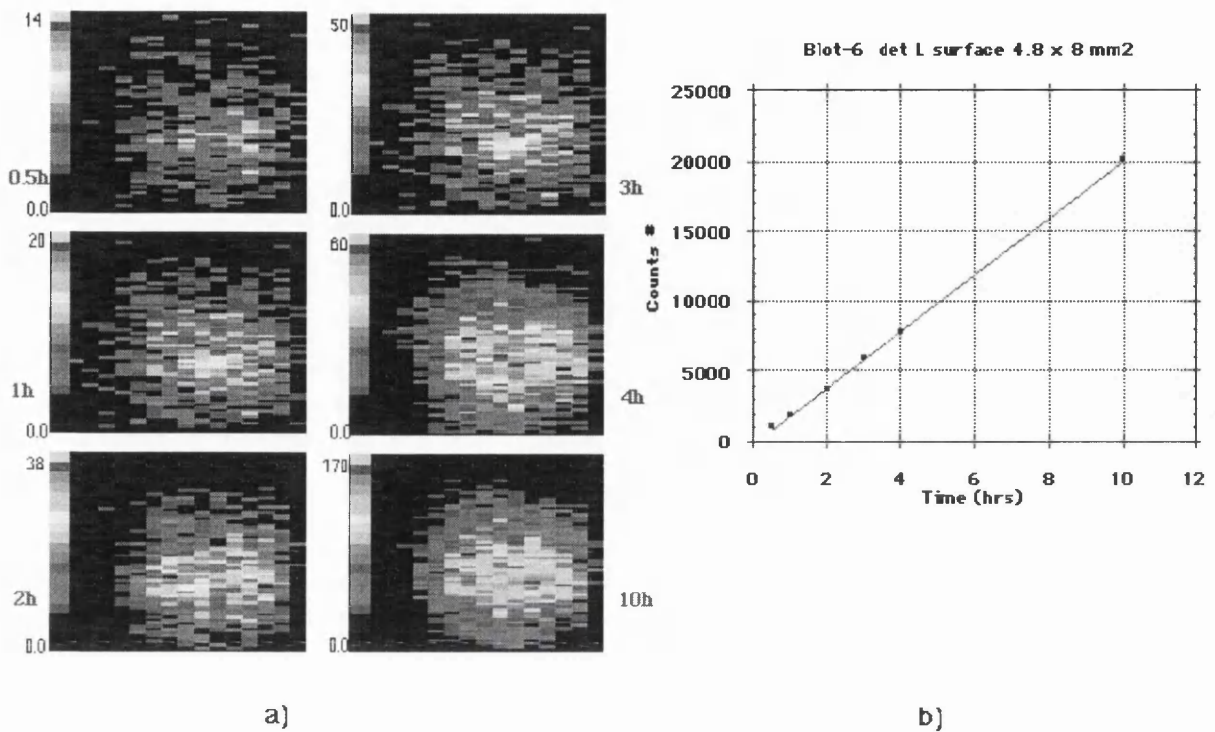
Figure 3-14. Linearity of response of the silicon pixel detector. The curve represents the total number of counts accumulated over the total matrix after a certain exposure time. The hot spot image is clearly visible after half an hour exposure time without filtering.

A direct comparison between the two profiles of the same DNA sequence as a function of the propagation length along the electrophoresis direction is shown in Figure 3-15. The phosphor image profile (solid line), scanned at 200μm resolution with 20 h exposure time, is compared with the silicon detector profile (data points) after 10 hours of exposure. In order to increase the statistics a line profile was calculated by adding the pixel content of each row. The pixel detector profile reproduces the profile obtained by the phosphor imager in half the time. The spatial resolution of the pixel system is 75μm (small pixel dimension), while the phosphor imager resolution is the 200μm resolution of the laser beam used to scan the image.
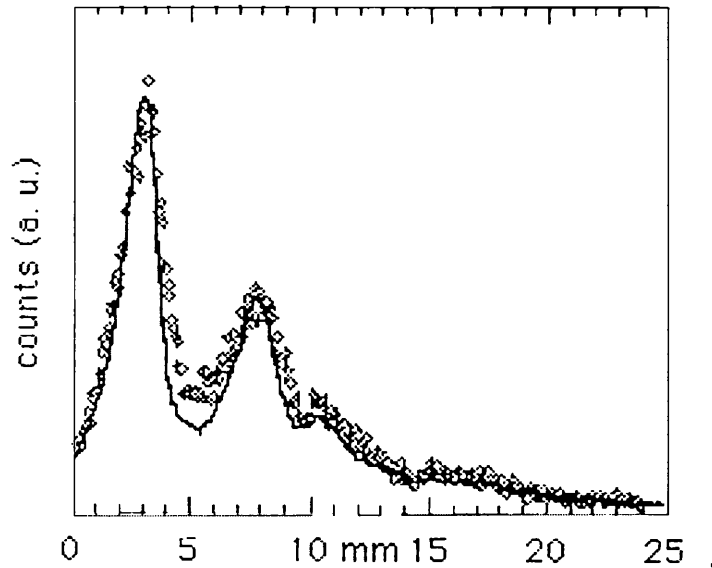
Figure 3-15. Direct comparison between the profiles of the same sample obtained with the phosphor imager (solid line) after 20 hours of exposure and the silicon pixel detector (diamonds) after 10 hours of exposure. In order to increase the statistics the pixel contents of each row were added together.

SUMMARY

It was demonstrated that the Omega3 electronics associated with a gallium arsenide or silicon pixel detector can collect images of phantoms with low contrast and good signal-to-noise ratio. The present system is not optimised for β^- or X-ray imaging because of asymmetric pixel dimensions and binary read-out architecture, but has low noise performance and high sensitivity. These properties are important parameters for this demonstration in combination with the presence of a fast-"OR" in the electronics which allows the system to be self-triggering.

The detection efficiency for high energy particles is more than 97%, thanks to the optimisation of the detector processing. An ion-implanted ohmic contact is used, as well as traditional metal-layers, which allows an over-depletion of the detector active area and an increase of the charge collection efficiency.

The asymmetry of the Omega pixel detectors is an advantage in applications like DNA-^{32}P labelled sequence autoradiography. In this case the radioactivity in the DNA

fragment has a geometrical distribution which follows the geometry of the detector (long thin lines), so a good spatial resolution is needed only in one direction. The good sensitivity and self triggering capability of the detector, in combination with the possibility of on-line monitoring, makes this device competitive with presently available systems in terms of reduction of exposure time.

CHAPTER 4

This chapter describes an investigation of a novel type of visible photon pixel detector based on high resistivity silicon with a special contact transparent to visible and infrared (IR) light. The detector was bump bonded to the OmegaD and Omega2 electronics [123].

This study was motivated by the search for a high resolution, fast and compact photosensitive device to use in combination with scintillating fibres for high energy particle tracking or scintillating crystals for nuclear medicine applications, where it is necessary to use a converter to detect high energy X-rays.

The chapter begins with a description of tests of the optical characteristics of the detector. These were measured by illuminating the transparent window with various pulsed monochromatic light sources. The results of tests with radioactive sources and particle beams using scintillating fibres coupled to the pixel matrix by an image intensifier are then described. Finally images obtained by illuminating scintillating crystals commonly used in nuclear medicine with radioactive X-ray sources are shown.

VISIBLE PHOTON PIXEL DETECTOR

The mechanical structure of the photosensitive hybrid silicon pixel detector is shown in Figure 4-1. To allow the visible light to reach the sensitive detector region, the aluminium layer on the back side, through which the bias-voltage is supplied, was removed and substituted by an n^+ ion implantation. The dimensions of the matrix match those of the OmegaD and Omega2 electronics, covering an area of 4.8 x 8 mm^2 in each case.
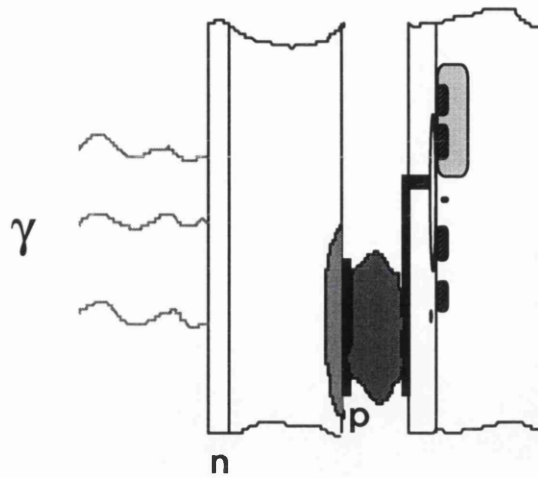
Figure 4-1. Sketch of the hybrid pixel detector used for visible photon detection

NOISE AND NON UNIFORMITY MEASUREMENTS OF THE PIXEL CHIP USING IR LIGHT

Normally the behaviour of the read-out chip was assessed using a row of test pixels at the top of the matrix, electrically injecting a signal across a test capacitance[60]. In the case of the photosensitive pixel detector we have the possibility to address every pixel in the matrix.

A schematic diagram of the experimental set-up used for this purpose is shown in Figure 4.2.
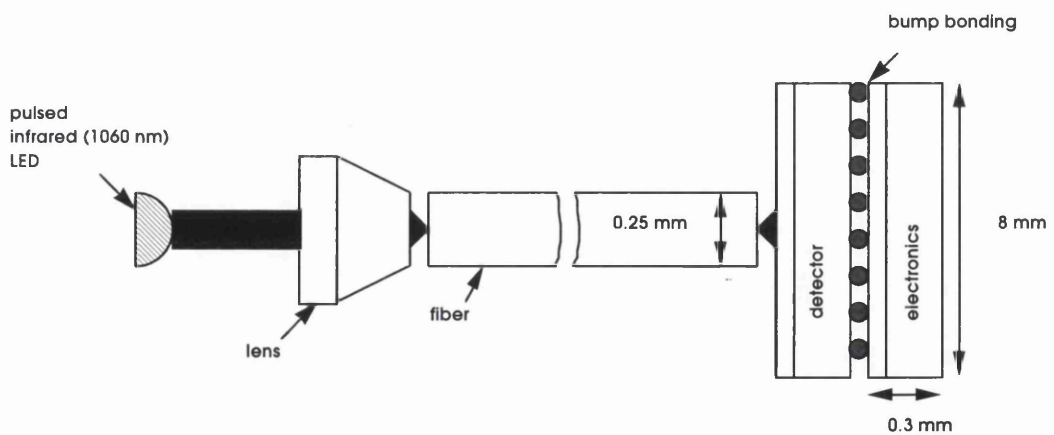
Figure 4-2. The optical set-up used to inject infrared light into the photopixel. The infrared LED was pulsed at the same frequency as the electronic strobe.

In this case the light of an infra-red (IR) Light Emitting Diode (LED) ($\lambda = 1060$ nm) was focused into a 250 µm diameter fibre to produce a spot of the same diameter on the back side of the detector. The LED was then pulsed at the same frequency as the detector read-out strobe and the strobe delay was adjusted to correspond with the 500 ns internal delay of the read-out circuit.

From previous electrical measurements of a test row only, a threshold variation of 15%[62] was expected from pixel to pixel. The threshold is measured by varying the input signal until a particular pixel responds positively to 50 % of given strobes. It was possible to vary the input signal amplitude by adjusting the LED bias voltage. Output pulses of ~5ns width were obtained using a home-made LED driver and the pulse frequency was 100 kHz

The calculation of the number of photons emitted by the LED was made using the *Responsivity* curve of the UDT photodiode[118]. The *Responsivity, R* (Amperes/Watt), is an expression of the spectral response of a photodiode (Figure 4-3) and is correlated to the Quantum Efficiency (QE) of the device by the Equation:

$$QE = \frac{1.24 \times R}{\lambda}$$

Equation 4-1

where λ the wavelength. The number of photons emitted by the LED per pulse can be calculated by [121][122]:

$$N_{ph} = \frac{1}{QE_{PD}} \frac{A_{PD}}{e \times f}$$

Equation 4-2

where QE_{PD} is the photodiode quantum efficiency, A_{PD} is the photodiode current, e the electron charge and f the LED pulse frequency.
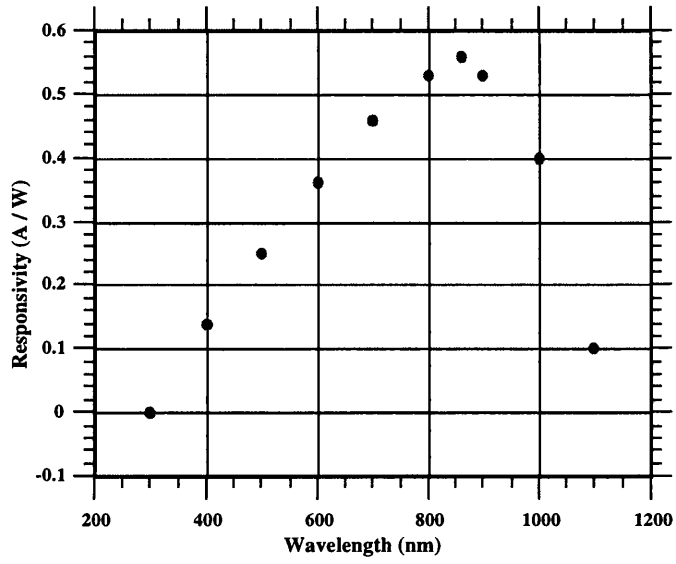
Figure 4-3. Responsivity curve of the UDT photodiode [118]

The photon number from the IR LED increased linearly with the applied voltage in the region of interest as can be seen in Figure 4-4
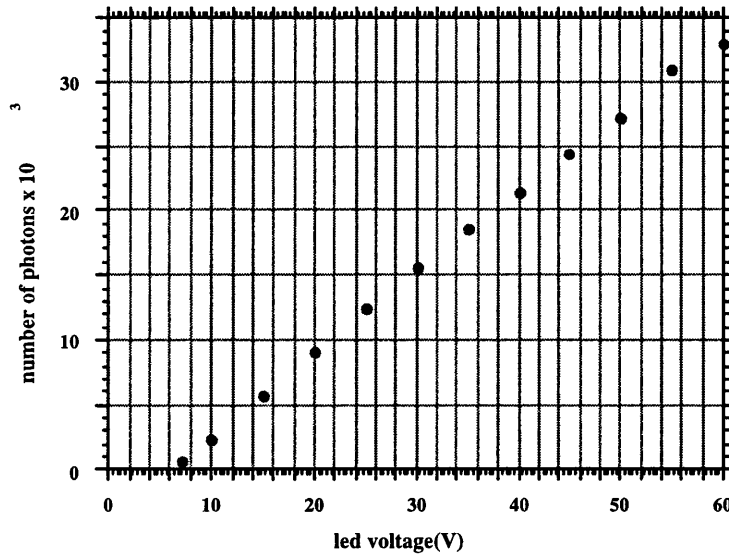
Figure 4-4. Calibration curve of the infra-red light emitting diode (LED). The number of photons emitted per pulse varied linearly with the LED bias voltage.

As it was impossible to know in absolute terms how many electrons are collected in one pixel, a first estimate of the threshold variation was made by dividing the standard deviation σ_{th} of the LED bias voltage by the mean for one row Q_{th}: $\sigma_{th}/Q_{th} \sim 16\,\%$, a ratio which corresponds very closely to the electrical measurements [60][61]. In the column the variation was somewhat lower, $\sigma_{th}/Q_{th} \sim 12\,\%$ (Figure 4-5). This lower value was expected due to the electrical biasing for the pixel read-out chip which was done on a column by column basis.
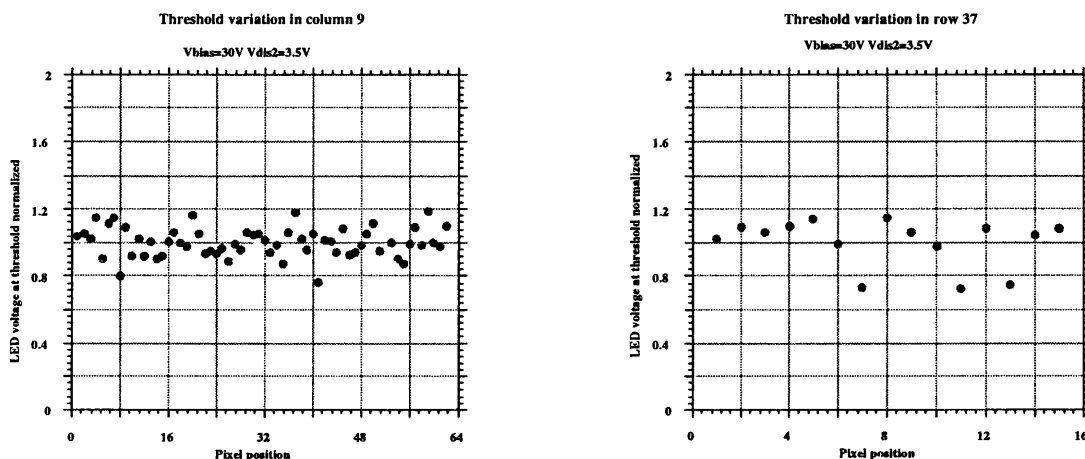
Figure 4-5. Threshold levels expressed in terms of the LED bias voltage (normalised) for column 9 (left) and row37 (right). Vdis2 is the voltage applied to the comparator circuit corresponding to a threshold of ~10 000 e.

An estimate of the noise was made by plotting the number of positive responses over a given number of strobes versus the input signal amplitude. The curve obtained using this technique is shown in Figure 4-6. The difference in input signal between 2 % and 98 % is equivalent to 4 σ_n, where σ_n is the noise referred to the input[60]. Calculating the ratio of noise over mean threshold, $\sigma_n/Q_{th} \sim 2\,\%$ is obtained which corresponds to a value of σ_n of around 200 e⁻ assuming a threshold of 10 000 e⁻. This figure agrees with radioactive source measurements [61]

I.R. LED (EG&G C30116-1060nm)

Pixel position (12,9) Vbias=30V Vdis2=3.5V
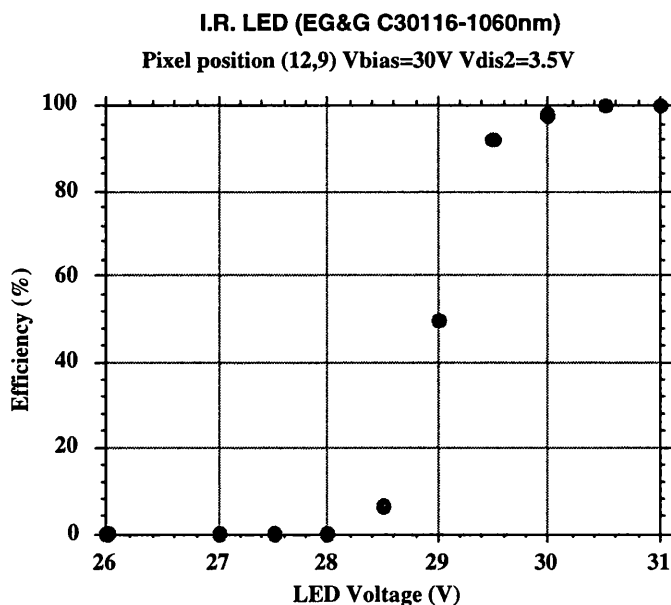
Figure 4-6. Number of positive pixel responses divided by the number of strobe pulses given for various input signals. This curve can be used to estimate the noise of the system.

Another important feature of the system is the non-uniformity of the internal delay from pixel to pixel. As in the previous measurement a single pixel in the matrix was addressed with light pulses, but for more precise injection of the optical power we used a pig-tailed LED (ABB HAFO-1A184A, λ= 850 nm), with a 50 μm fibre core diameter. The LED was then pulsed with the same frequency as the detector strobe and the strobe signal rising edge was adjusted to coincide with the falling edge of the internally delayed signal. This corresponds to the minimum delay of the collected charge arrival before the start of the read-out [62].

The variation of the delay from pixel to pixel for one column and for one row were also estimated (Figure 4-7). The delay variation is again made by dividing the standard deviation of the measured delays, σ_t by the mean delay, D_t. For column 8, for example, $\sigma_t/D_t{\sim}3.4$ % and for row 12 $\sigma_t/D_t \sim 8$ %.
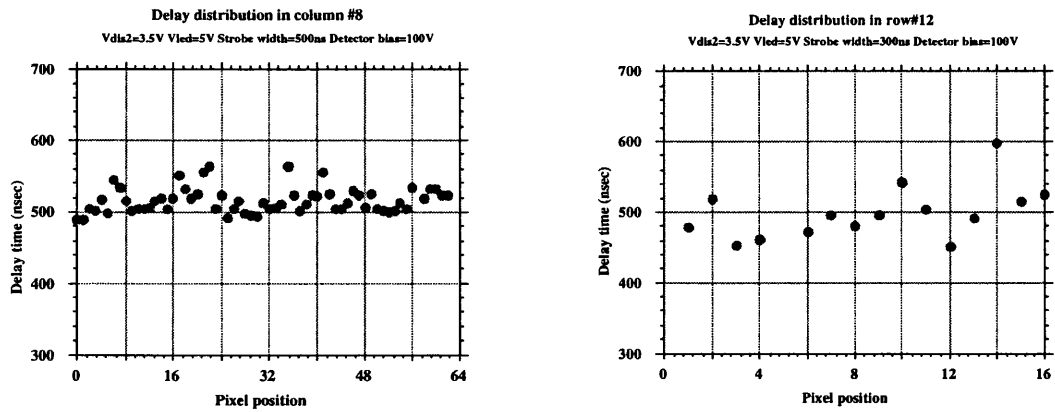
Figure 4-7. Variation of the delay from pixel to pixel in one column (left) and one row (right).

The row measurements correspond well with previous electrical measurements [62] and the column measurements indicate once again a better uniformity than the rows.

PIXEL RESPONSE AT DIFFERENT VISIBLE WAVELENGTHS

The behaviour of the pixel detector was then studied with visible light, with the same test set-up used for the IR light tests.

LEDs of three different wavelengths were used: red (λ = 635 nm), green (λ = 565 nm) and blue(λ = 470 nm). Firstly, to check the responsivity of the detector to the various wavelengths, we monitored the current flowing into the back of the detector. This current is the sum of the detector leakage (dark) current and the photocurrent.

A high frequency pulsed current (100 kHz) was injected into the LED and the difference in the current from the detector with and without illumination noted. The results are shown in table 4-1.

111

table 4-1 Measured response of the silicon pixels and of the commercial photodiode (UDT-FIL 100V) at different wavelengths

LED type	λ (nm)	LED DC current (mA)	Pixel photocurrent (μA)	Photodiode photocurrent (μA)
Blue	470	50	0.70	0.64
Green	565	20	0.25	0.27
Red	635	20	3.6	3.9
IR	1060	20	4.2	0.9

In all cases the detector was sensitive to light. It can be seen however, that the quantity of light injected per unit of drive current by the blue LED was less than for the others. The measured photocurrent of the detector was then compared with the photocurrent obtained from the UDT photodiode. These results are also given in table 4-1. It appears that the high resistivity silicon detector is more sensitive than the commercial diode for longer wavelengths. This can be explained by the higher penetration depth of IR light into the silicon pixel detector active volume (Figure 1-5).

The complete pixel detector including the pixel read-out electronics was then activated using the different LEDs. The LEDs were pulsed with pulses of variable amplitude and a width of < 5 ns and the strobe of the pixel electronics was synchronised to the LED drive circuit. Measurements were made of the LED bias voltage required for 50 % response from the pixel read-out electronics at various detector bias voltages. Figure 4-7 shows the results of measurements obtained with red and green light.

In the case for blue light it was never possible to detect the converted photons despite the amount of photocurrent detected. This can be explained since the pixel electronics is most sensitive when the photo-electric conversion takes place inside the depletion region of the silicon detector and this is not the case of blue light which penetrates to a depth of only ~1μm [24], still in the ion implantation region. This does not seem to prevent charge collection in the case of direct photocurrent read-out, which was made on the same side as the illumination.

In the case of the red light source, a detector bias of around 70 V was necessary before the required LED bias voltage flattened out, whereas with the green light around 110 V was necessary (Figure 4-8).
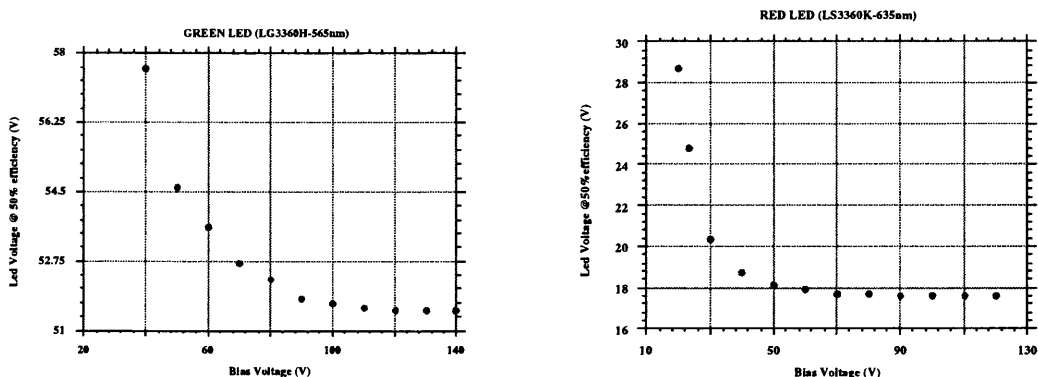
Figure 4-8. The LED input voltage required to have a pixel response in 50% of strobes, for green (left) and red (right) LEDs.

This can be explained by realising that most of the green light is deposited in the first 2 μm of the silicon and this must be depleted for the photoelectrons to be fully detected.

As the back side of the detector is implanted with n^+ to provide the ohmic contact this requires a large voltage before being fully depleted. It was therefore chosen to work at 110 V when using the red LED and 120 V when using the green one. As a further verification of the good sensitivity of the pixel electronics to visible light, the noise measurements described above were repeated for the red and green LEDs. Figure 4-9 shows the results obtained for the green (left) and red (right) LEDs. Again using a correction factor for the LED voltages the values of σ_n/Q_{th} obtained were 2 % for the red LED and 2 % for the green LED.
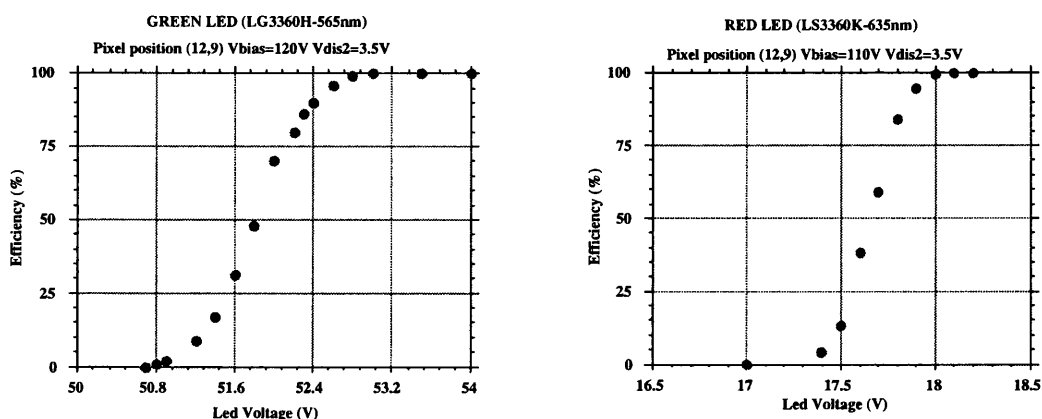
Figure 4-9. Noise measurement results obtained for green (left) and red (right) LEDs.

Finally the quantum efficiencies of the silicon pixels relative to the UDT-FIL 100V silicon photodiode were calculated. The results are shown in Figure 4-10 [123]. The dots represent the ratio of the measured photocurrents for the high frequency illumination while the squares represent the ratio between the number of photons estimated at the threshold for a single pixel and the number of photons measured with the UDT photodiode. The error on this second approach is essentially due to the uncertainty in the dimension of the focused spot and the corresponding uncertainty in the number of pixels illuminated during the measurement.
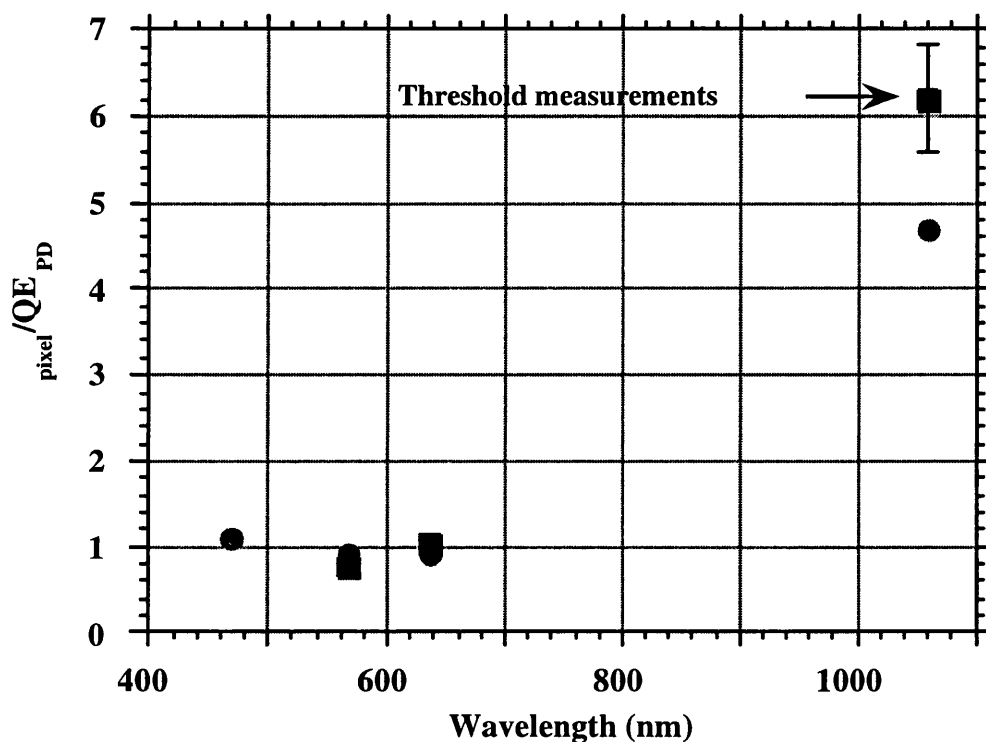
Figure 4-10. Comparison of the quantum efficiency of the silicon pixel detector with the UDT-FIL 100V photodiode. The dots represent the ratios of the measured photocurrents while the squares represent the ratio between the number of photons estimated at the threshold and the number of photons measured with the UDT photodiode.

READ OUT OF SCINTILLATING FIBRES AND SCINTILLATING CRYSTALS

Based on the silicon detector described above, a novel read-out system for scintillating fibres and scintillating crystals was developed as a combination of the silicon pixel matrix and a micro-channel plate (MCP) image intensifier with a maximum photon gain of ~ 1000. Scintillating fibre ribbons and crystal bundles were coupled to the detector array. Light emitted from the scintillating materials was amplified in the MCP device and detected by the photo-sensitive pixel detector.

SYSTEM SET-UP AND CALIBRATION

Figure 4-11 shows the set-up used to calibrate the system. At the input to the image intensifier there is a type S20 photocathode with a peak sensitivity at 420 nm and a maximum quantum efficiency of 22%. This is followed by the MCP, which provides the amplification, and then by a type P46 phosphor screen with an emission peak at 530 nm and a decay time (fast component) of ~ 100 ns.

The image intensifier (type 1450R from DEP[118]) is a proximity focused device. The input-output windows are 18mm in diameter. A 3 mm thick fibre-optic faceplate made of a bundle of 10 μm diameter clear fibres (SCHOTT) [128] provides good optical contact between the phosphor screen and the pixel detector.
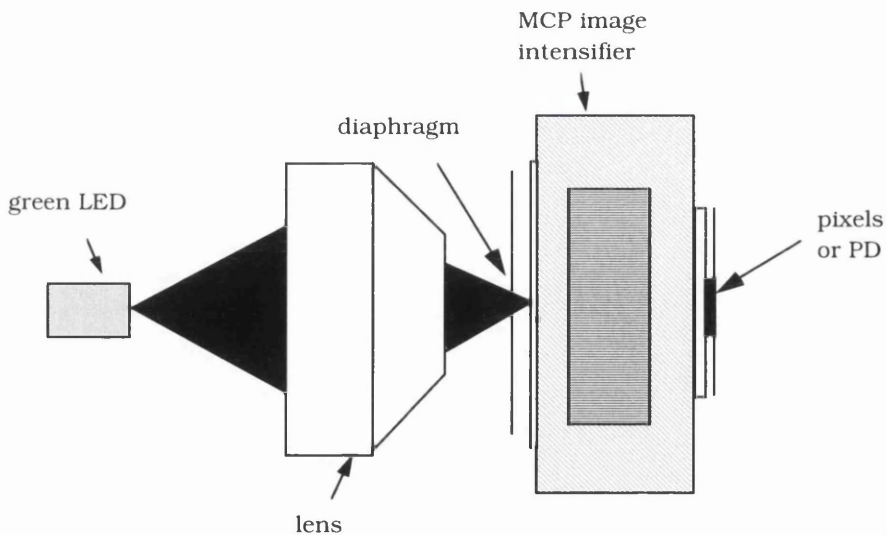
Figure 4-11. The set-up used for calibration of the MCP image intensifier. The diameter of the diaphragm is 300 μm.

A first test was performed in order to determine the gain of the MCP. The light from a green LED was focused through a diaphragm onto the photocathode of the image intensifier and the light output from the phosphor screen was detected by the UDT photodiode.

The same photodiode was later used to measure the incident light, giving a direct measurement of the image intensifier photon-gain as a function of the applied voltage across the MCP. The results thus obtained are shown in Figure 4-12.
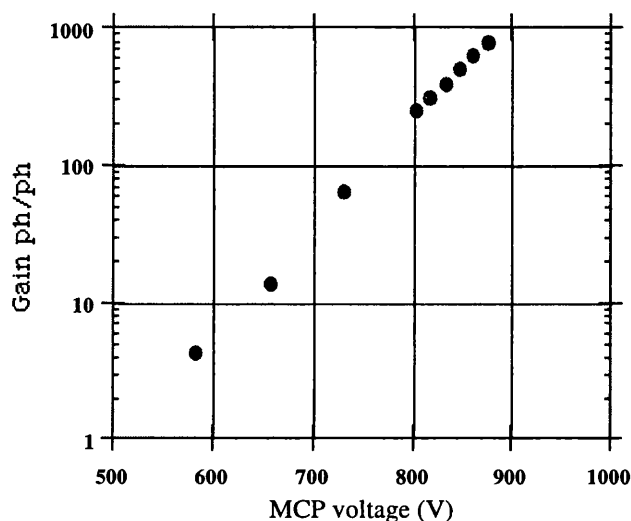
Figure 4-12. The gain versus applied voltage characteristic of the MCP image intensifier. This curve agrees well with the manufacturer's specifications.

These correspond very well to the manufacturer's data sheet. The maximum gain obtained was ~ 1000 for an applied voltage of ~ 900 V. The standard operating condition utilised a gain of 800, corresponding to an applied voltage of 875 V.

The photodiode was then replaced by the photopixel matrix and the image of the 300 μm diaphragm was collected (Figure 4-13). The FWHM of the image covers four pixels in the short dimension, corresponding to the 300 μm diameter.
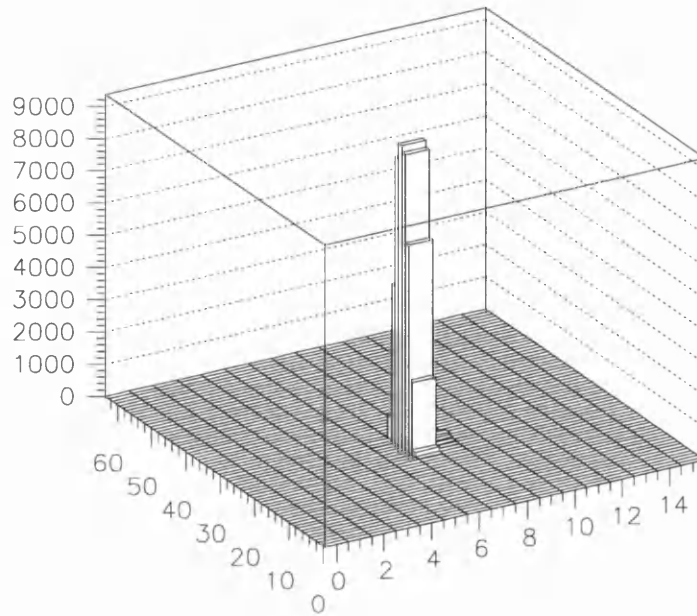
Figure 4-13. The accumulated profile of the diaphragm. The FWHM is 4 pixels, which corresponds to the 300 μm diaphragm hole.

TESTING WITH A RADIOACTIVE SOURCE

The intensifier photocathode spectral sensitivity matched the emission spectrum of SCSF-38 blue emitting scintillating fibres (peak emission at 430 nm)[125]. With the experimental set-up of Figure 4-14, tracks from a collimated ^{90}Sr β-source in a five-layer ribbon of 500 μm diameter fibres were imaged. The scintillating fibre ribbon was coupled to the intensifier photocathode using an optical gel, as shown in Figure 4-14. The fibre length was 15 cm.
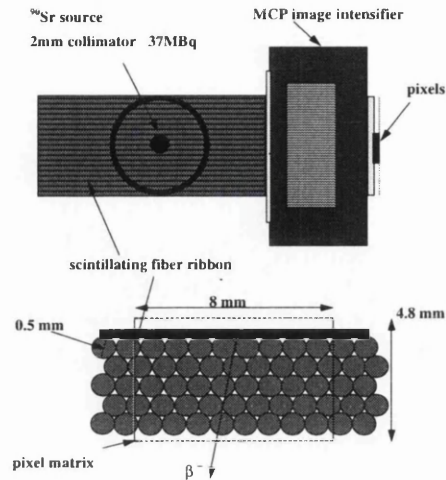
Figure 4-14. The set-up used for the radioactive source measurements.

The attenuation length of this kind of fibre has been measured at ~2 m[126].

The ^{90}Sr β-source, collimated by a 2 mm hole, was placed 6 cm from the image intensifier. Random triggers were given to the pixel detector and the beam profile shown in Figure 4-15 was accumulated.
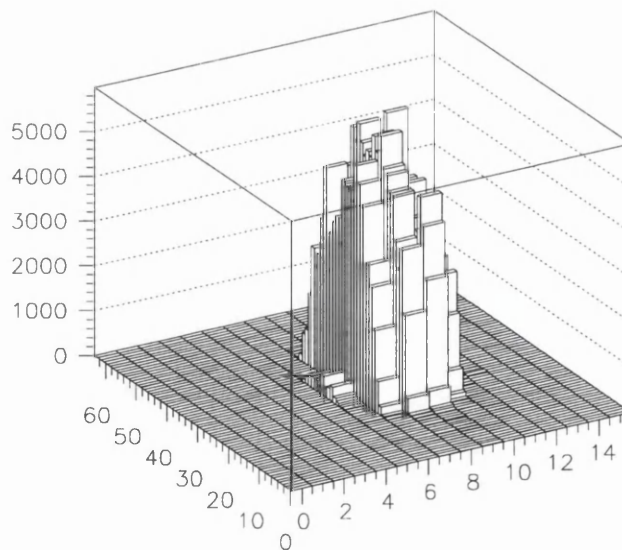
Figure 4-15. The accumulated beam profile for the collimated radioactive source.

The 2 mm collimation corresponding to 4 pixels in the long dimension was clearly observed, together with around 29 pixels hit in the short dimension, corresponding to the 2.1mm thickness of the fibre ribbon. In this way we verified that the proposed set-up works.

The efficiency was then measured using two other scintillating fibres, S1 and S2, which were coupled to standard photomultiplier tubes and used to provide a trigger for the fibre bundle.

The ^{90}Sr ß source was placed in this case at a distance of ~9 cm from the fibre bundle (Figure 4-16). The expected light yield from each fibre was ~24 photons at a mean wavelength of 430 nm [126].
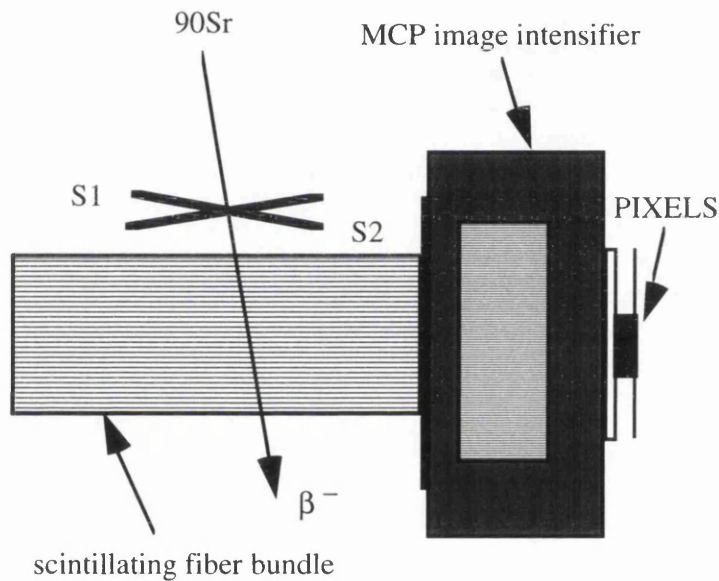
Figure 4-16. Telescope for ß particle detection. Kuraray SCSF-38 1 mm diameter scintillating fibers[125], S1 and S2 were used to trigger on the incoming particles.

Assuming an image intensifier gain of 1800 (the measured gain with the green LED (1000) multiplied by the ratio of the photocathode quantum efficiencies for the different wavelengths) and the Si quantum efficiency of 70%, we expect to collect ~30 000 e per fibre in the pixel detector. This charge, however, is spread over at least 11 pixels. The standard pixel detector comparator threshold was 10 000 e-. Data were accumulated on the pixel detector read-out system and the resulting beam profile is shown in Figure 4-17. It is possible to observe at least 2 rows of fibres.
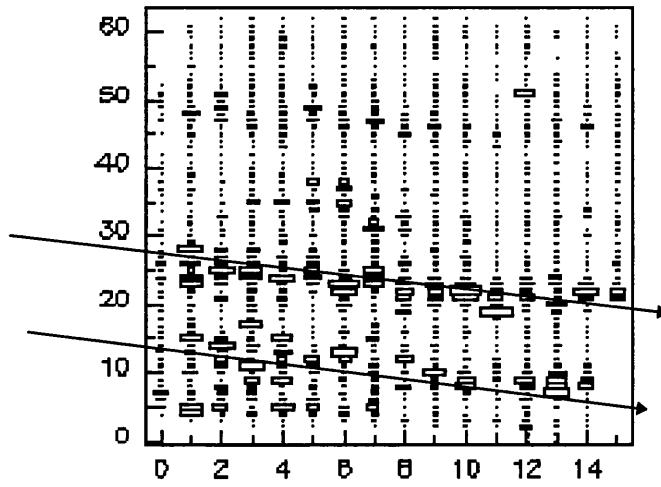
Figure 4-17. Accumulation of tracks detected by the photopixel matrix. The single fibre efficiency cannot be evaluated due to the fibre-pixel mismatch.

A scan of detection efficiency versus pixel threshold is shown in Figure 4-18.
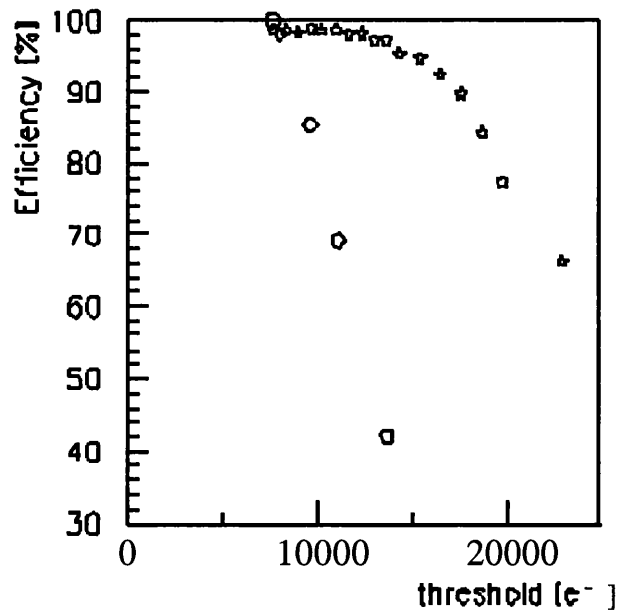
Figure 4-18. Fibre tracking detection efficiency (open circles) compared with 300μm silicon pixels (stars) as a function of threshold setting.

120

The detection efficiency is defined as the presence of at least one hit in the pixel matrix per trigger. The efficiency was 100% for a pixel threshold of ~8000 e⁻. This was compared with the detection efficiency of a 300 μm thick silicon detector which directly detects the particles. It is difficult to define the single fibre detection efficiency of the system as the fibre diameter is not well matched to the pixel dimension.

BEAM TEST RESULTS

Another test of the detection efficiency of the system was made using the H6 test beam at the CERN SPS. This facility provided 120 GeV/c pions acting as Minimum Ionizing Particles (MIPs). The only modification made to the set-up was that the fibre ribbon was replaced by a ribbon of 1.5 m length. The fibre ribbon was then inserted into the RD-19 pixel telescope. The geometry of the telescope with the fibres added is shown in Figure 4-19.

The beam was defined by the cross-over of scintillating fibres S3 and S4, which formed a $1 \times 1 \text{mm}^2$ area. The distance between this cross-over point and the image intensifier was 65 cm. Data were accumulated in all three planes after setting different threshold currents in the photopixel plane.
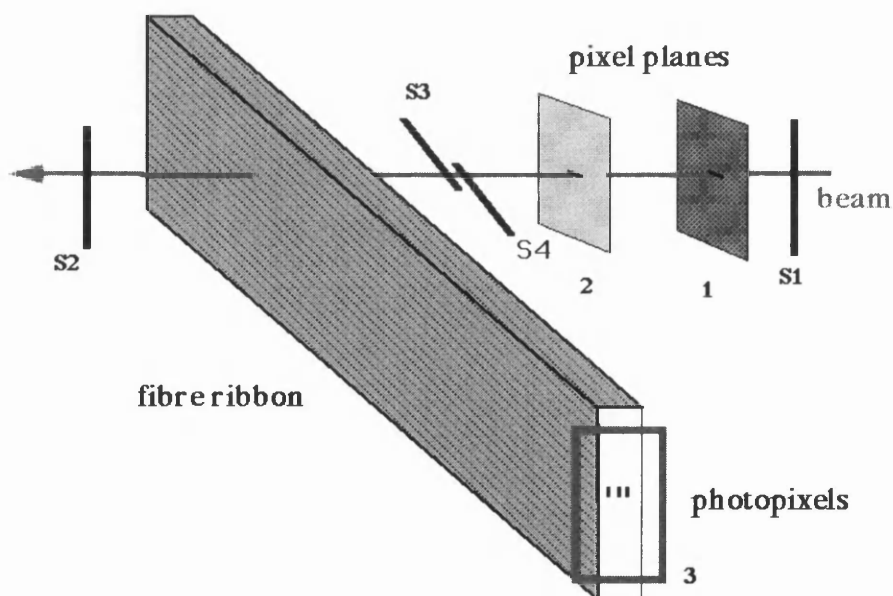
Figure 4-19. The RD 19 pixel telescope with the fibre ribbon added. Triggers are produced by the coincidence of signals in scintillators S1, S2, S3 and S4. This forms a $1 \times 1 \text{ mm}^2$ area in pixel planes 1 and 2. The beam itself is much wider than this.

To make a first estimate of overall detection efficiency, events with a track in planes 1 and 2 were examined, looking for at least one correlated hit in plane 3.

The curve of efficiency versus threshold is shown in Figure 4-20. For reference, data were added from a 300 µm thick silicon pixel detector placed directly in the beam. It was observed that the detection efficiency of the fibre set-up measured in this way is around 40%. As each incident particle crossed several fibres, more than one hit was expected in plane 3. Therefore, a track in plane 3 was defined as an event with two or more correlated hits.

The track detection efficiency, also shown in Figure 4-20, was at best 18%. A further test was made, increasing the MCP bias voltage to ~ 900 V in order to increase the gain of the MCP. In this case the detection efficiency reached a maximum of 51.2% and the track detection efficiency a maximum value of 23%.
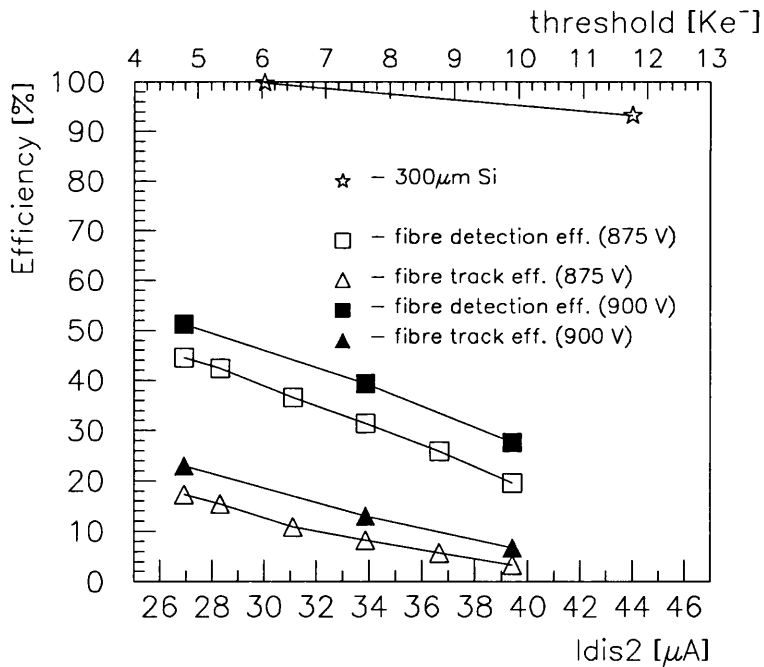
Figure 4-20. The efficiency versus threshold curve for the fibre ribbon. The 300 µm Si curve is added for reference.

This leads to an analysis of the system's limitations. Typically, the number of photons produced by a MIP crossing a fibre and reaching its end is ~ 20 [126]. This means that at 875 V MCP bias one MIP will produce ~ 29 000 photons at the output of the image intensifier. We have corrected the gain measured in the green with the photocathode quantum efficiency at 430 nm. With a quantum efficiency in the green of 70% the pixel detector collects ~ 20 000 e⁻. With an MCP bias voltage of 900 V, the charge delivered to the pixel is typically ~25 000 e⁻.

In addition, light emitted from one fibre is spread over several pixels (the small pixel dimension is 75 μm whilst the fibres are 500 μm in diameter). As the lowest comparator operating threshold of the pixel detector is around 8 000 e⁻, the low track detection efficiency is consistent with the limitations of the system.

A beam profile is shown in Figure 4-21. The two columns corresponding to the 1 mm scintillator crossover are clearly evident. Compared with the source measurements there is a large number of background hits. These are not present when the beam is off, and can be explained by particle 'hits' in the fibres outside the 1 mm × 1 mm coincidence.
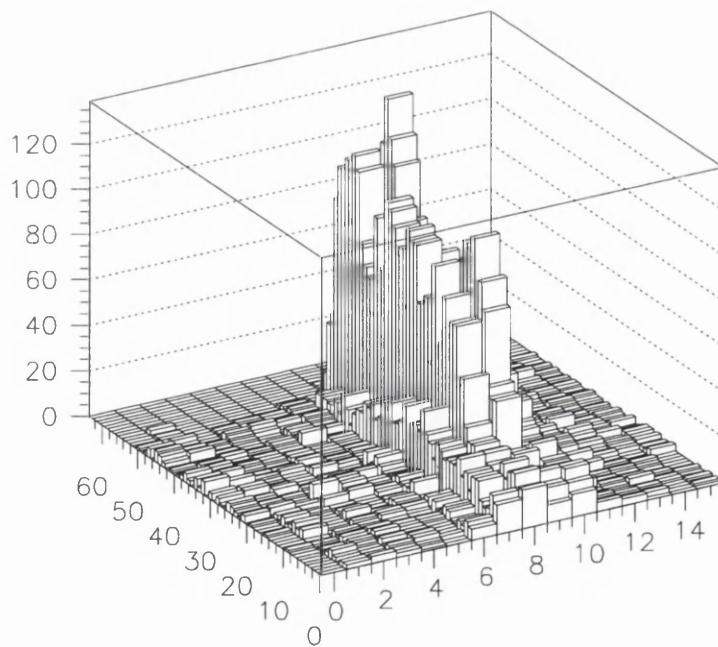
Figure 4-21. The accumulated beam profile in the fibre plane. The 1 mm wide coincidence region is clearly evident. The hits outside this region are due to untriggered particle tracks.

IMAGING APPLICATIONS WITH SCINTILLATING CRYSTALS

In a further set of measurements the system discussed above was used to image 122 keV γ-rays, close in energy to those used in nuclear medicine, from a [57]Co source. The possibility of single photon counting, high spatial resolution and possible Compton rejection by using the comparator threshold of the electronics, renders such a system interesting for this kind of application.

Figure 4-22 shows the configuration of the visible photon imaging system. The crystals were coupled to the intensifier like the scintillating fibres.
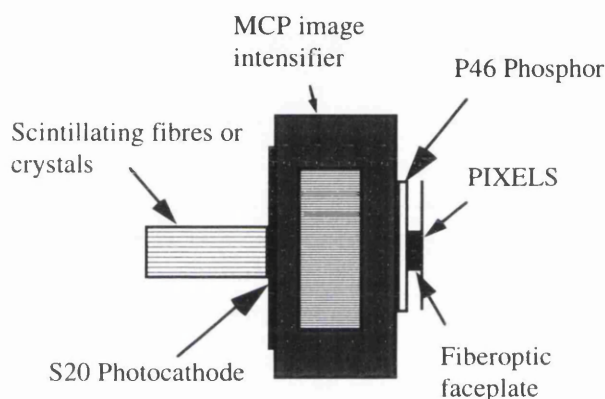
Figure 4-22. Configuration of the photon imaging system. The MCP image intensifier is used with a maximum photon gain of 1000 (green).

In order to test the suitability of the system for medical applications, images were formed of different scintillating crystals commonly used in nuclear medicine. In each case we illuminated the crystals with a [57]Co radioactive source with a peak emission photon energy of 122 keV.

Figure 4-23 and 4-24 show images obtained with two 1mm^2 10 mm long CsI crystals with a peak emission wavelength of 550 nm placed at the photocathode. These crystals should emit ~ 1600 visible photons for the 122 keV x-rays[22]
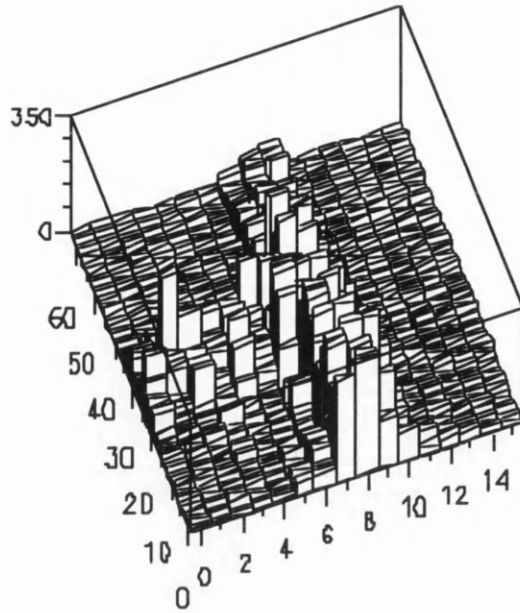
Figure 4-23. Image obtained with two 1 mm^2, 10mm long CsI crystals. They were placed in a T shape at the image intensifier photocathode and irradiated with a ^{57}Co source.
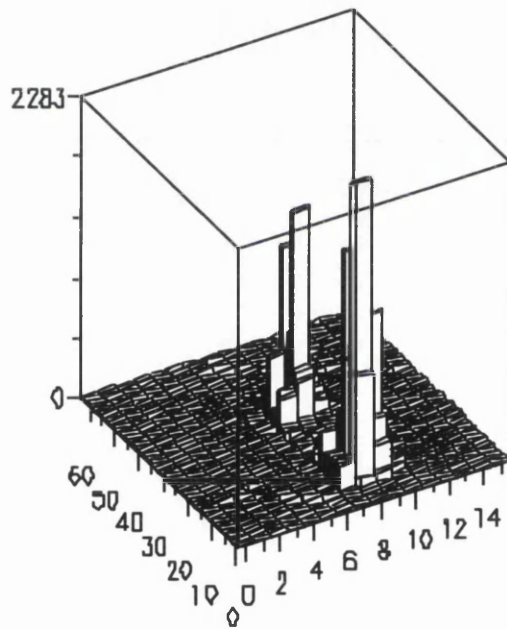
Figure 4-24. The image obtained with two 1 mm^2, 10 mm long CsI crystals. The crystals were placed at 90° with respect to the image intensifier photocathode and the distance between them was ~1mm .

Assuming an image intensifier gain of 1000 and 70 % quantum efficiency for the Si, ~1 x 10^6 e$^-$ are expected to be generated in the pixel detector. Thus we should detect every X-ray which falls within the sensitive strobe interval (~500ns). The crystals were first joined in a T shape and in the second test separately placed at 90° with respect to the photocathode surface. In this case the distance between the two crystals was ~1mm. The separate images of the two crystals are clearly resolved.

Figure 4-25 shows the image obtained using a bundle of 24 YAP : Ce* crystals of 0.7 x 0.7 mm^2 cross-section and 16 mm length, emitting at 370 nm. Again the image of the crystals is clearly observable. In this case we expect ~ 300 photons per x-ray [[129] resulting in ~ 380 x 10^3 e$^-$ collected by the pixel detector. It should be noted that the background hits in these images come from noise in the image intensifier. There are no noise hits in the pixel detector when the image intensifier is switched off. The main interest in using this read-out for medical imaging is the single x-ray detection capability and the possibility of rejection of photon counts after Compton scattering with a properly adjusted threshold in the pixel discriminator. At present the maximum threshold can be set at ~ 100 keV.
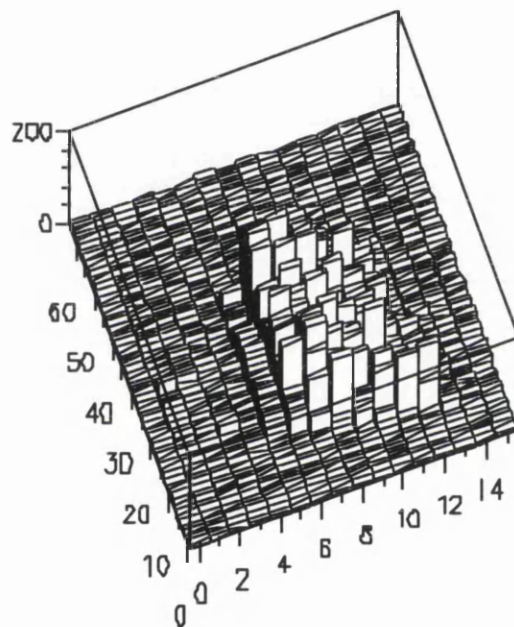
Figure 4-25. Image of a square shaped bundle of 24 YAP:Ce crystals.

SUMMARY ·

A system which combines a silicon pixel detector, a MCP image intensifier, scintillating fibres and scintillating crystals was tested with radioactive sources and particle beams. Such a system offers a very interesting alternative for the read-out of scintillating materials.

While the advantages of a high spatial resolution are maintained, compared with multi-anodes photomultipliers, system cost is kept to a minimum. The pixel detector offers more than 100 times better read-out speed than that offered by CCDs.

The image intensifier chosen behaved exactly according to the manufacturer's specifications. Tracks were detected by the pixel detector using both a radioactive source and a high-energy particle beam. The total detection efficiency is limited at present by the quantum efficiency of the photocathode, the minimum threshold of the pixel detector and the shape of the pixel itself.

There are several ways of optimising this system in a future iteration. One improvement would be to use an image intensifier produced by Intevac[127] which incorporates a GaAsP photocathode with a peak quantum efficiency of 39 % at a wavelength of 530 nm. A new pixel read-out chip is being developed with a lower minimum threshold. It would also be beneficial if the pixel dimensions were better matched to the scintillating crystal dimension or the fibre diameter.

CHAPTER 5

SUMMARY AND CONCLUSIONS

The ideal detector for imaging applications has to have a high spatial resolution, to cover a big area and to be efficient for the type of radiation used. For medical applications where X-rays are used in a wide energy range direct detection is the preferred technique, but due to the limited availability of high efficiency semiconductor materials, feasible only below 100 keV X-ray energy. Photon counting is preferable, moreover, if the X-ray source is not monochromatic since the spread in X-ray energy generally worsens the noise performance of the detector.

Nuclear medicine, which deals with photons at energies above 100 keV, needs other approaches for its detectors, essentially converters before photodetecting devices. With the same type of considerations pixels are preferred to other detectors, cooled CCDs or smart pixel sensors as promising substitutes for film plates.

Semiconductors are very well suited in their intrinsic properties to the requirements mentioned above. VLSI technology helps in this direction and nowadays a wide variety of structures, (strips, monolithic pixels, hybrid pixels) is available while even more sophisticated detectors are under study to cope with the extreme requirements of radiation hard environments.

A general introduction to the advantages and disadvantages of the different approaches to pixel detectors was first presented. More details were given of the Omega hybrid pixel family, their structure and the technique used to cover large areas with them. This served as an introduction to the study presented in the following chapters, where the Omega electronics chips were used in combination with silicon and gallium arsenide pixel detectors.

In chapter 2 a direct measurement of the concentrations between 1.8×10^{16} /cm^3 and 2.4 $\times 10^{16}$ /cm^{3}of the EL2 defect at different bias voltages and different temperatures was described. The motivation for this study was a demonstration of the influence of electric field in the concentration of EL2 defects in SI-GaAs devices. The original, purely optical "dynamic" technique was chosen as an alternative to electro-induced techniques. The set-up for infrared tests is normally used with simply polished samples, and the necessity of having a biased device required some study to process semitransparent contacts, in order to have at the same time a uniform electric field on the detector and optical transmission of the infrared spectrum.

The trend of the above results seem to confirm the theory which predicts the presence of a quasi-neutral region in an LEC GaAs Schottky detector after the application of a bias voltage. But insufficient supply of injected electrons, overall at low temperature, might explain the expected variation of 3% also observed experimentally A direct dynamic measurement of EL2$^+$ using MCDA at the full set of bias voltages was not possible at the present experimental conditions, but further optimisations of the set-up should allow a more comprehensive study of the effects reported here.

It was shown that a pixel detector made by coupling the Omega3 electronics with a gallium arsenide detector can collect images of phantoms with a contrast of 27% and a signal-to-noise ratio of 1.3 with a comparator threshold of 5000 e using a ^{109}Cd source. The detection efficiency for high energy particles is more than 97%, thanks to the optimisation of the detector processing. An ion-implanted ohmic contact, used as an alternative to more traditional metal contacts, was shown to allow an over-depletion of the detector and an increase of the charge collection efficiency.

The present system is not optimised for β^- or X-ray imaging because of the asymmetric pixel dimensions and binary read-out architecture, but has low noise performance and high sensitivity. These properties are important parameters for this demonstration, together with the fast-"OR" in the electronics which allows the system to be self-triggering.

The asymmetry of the Omega pixel detectors is an advantage in applications like ^{32}P labelled DNA sequence autoradiography. In this case the radioactivity in the DNA fragment has a geometrical distribution which follows the geometry of the detector (long thin lines), so a good spatial resolution is needed only in one direction. The good sensitivity, 2×10^4 cps/mm^2 over a sensitive area of ~40 mm^2 and self-triggering capability of the detector, in combination with the possibility of on-line monitoring,

makes this device competitive with presently available systems in terms of reduction of exposure time. The use of the existing large area pixel detector planes could give sequence distributions in less than half the time compared with phosphor imagers and ¼ of the time compared with film plates. Furthermore the good spatial resolution of the pixel detectors, as low as 50 μm at present, could save time in the electrophoresis process.

A system which combines a silicon pixel detector, a MCP image intensifier, scintillating fibres and scintillating crystals was tested with radioactive sources and particle beams. A quantum efficiency of 53%, 66% and 78% was measured at 470nm, 565 and 635 nm respectively and results as expected for a silicon photodetector. The infrared response at 1060 nm was ~6 times higher for the pixel detector, in agreement with the ratio of the devices depletion regions 300 μm for the silicon pixel detector and and 50 μm for the UDT photodiode used for calibration. Such a system offers a very interesting alternative for read-out of scintillating materials: while the advantages of high spatial resolution are maintained, compared with multi-anodes photomultipliers, system cost is kept to a minimum. The pixel detector offers a read-out speed as high as 4 μs for a 16 x 64 matrix, compared with 10th of milliseconds of CCDs.

The image intensifier chosen behaved exactly according to the manufacturer's specifications. Tracks were detected by the pixel detector using both a radioactive source and a high-energy particle beam. The total detection efficiency is limited at present by the quantum efficiency of the photocathode, peak at ~18% in the blue region, the minimum threshold of the pixel detector and the shape of the pixel itself.

There are several ways of optimising this system in a future iteration. One improvement would be to use a better image intensifier, for example one produced by Intevac[127] which incorporates a GaAsP photocathode with a peak quantum efficiency of 39 % at a wavelength of 530 nm. Pixel electronics with a lower comparator threshold and pixel dimensions better matching the scintillating crystal dimensions or the fibre diameter would also be beneficial.

FUTURE

THE PHOTON COUNTING PIXEL DETECTOR

The experience gained with the Omega pixel detector electronics in tracking devices for high energy physics and the attempt to apply these devices to X-ray imaging (in work presented in this thesis) has triggered the study of a new, single-Photon counting read-out chip for pixel detectors which is better suited for imaging applications in medicine, biology and particle beam monitoring.

The chip is a matrix of 64 x 64 identical cells covering a total sensitive area of 1 cm². It is intended to be bump-bonded to an identical monolithic matrix of semiconductor diodes made from either Si or GaAs. Each cell comprises a preamplifier, a discriminator and a 15-bit counter. Each cell also has a 5-bit register which enables individual pixel comparator threshold adjustment as well as testing and masking.

Each cell (Figure F-2) comprises a preamplifier, a discriminator and a 15-bit counter. The preamplifier and discriminator have the same schematic as the LHC1 pixel read-out chip [63], but the layout has been adapted to the new pixel shape. In addition, the threshold can be adjusted individually for each pixel, a feature which was not present in the previous chips. Individual masking and testing of cells is also possible using 2 flip-flops reserved for that purpose. An externally supplied shutter signal determines when the counter is active. The layout of the cell is shown in Figure F-1.

Read-out is performed 16 columns at a time by putting the counters in series to form a long shift register per column. The number of clock cycles required for read-out is therefore 15 x 64 x 4, which results in a read-out time of less than 400µs for a clock frequency of 10MHz.

A micro-photograph of the single "Photon counting" pixel cell is shown in Figure F-3.
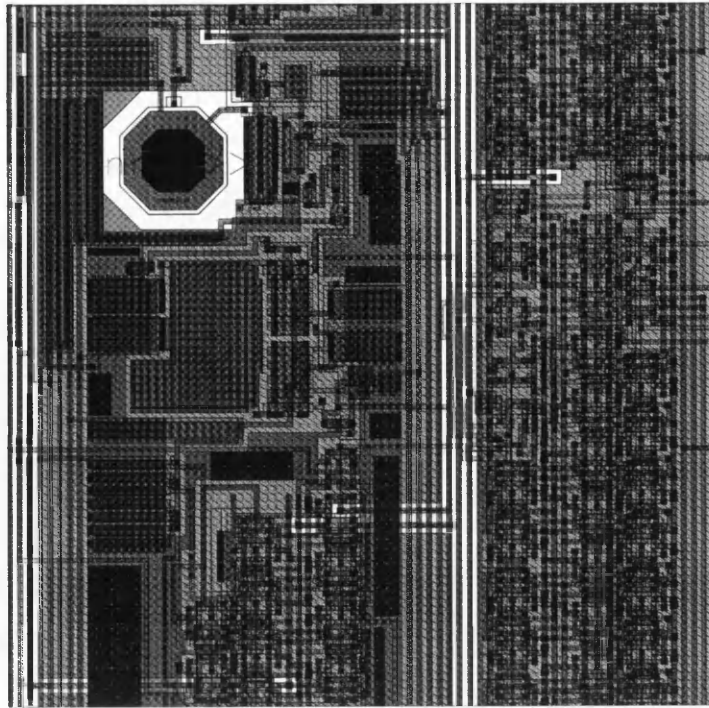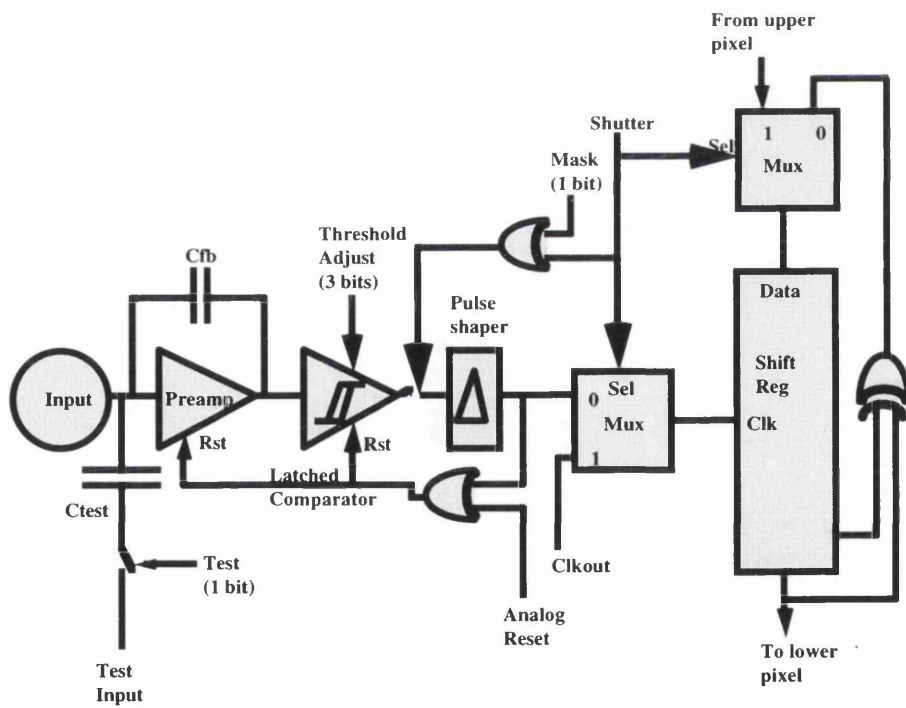
Figure F-1: Layout of the cell
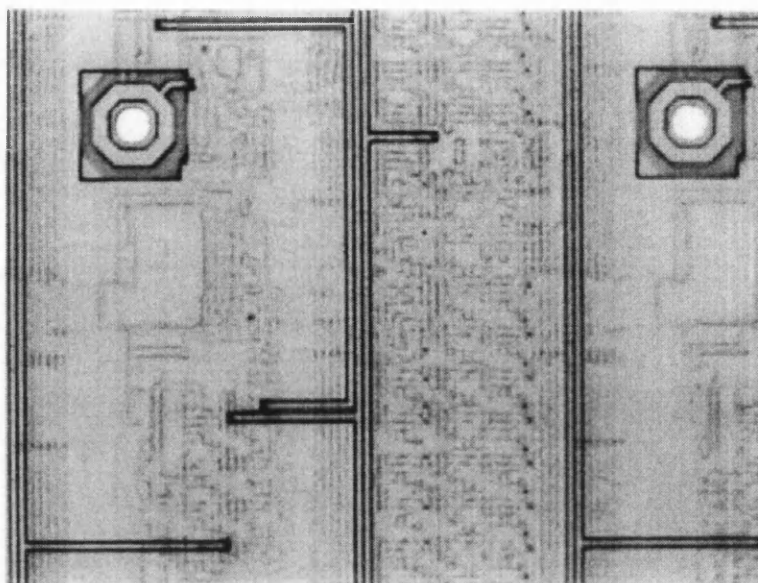

Figure F-2 Pixel block diagram

Figure F-3. Micro-photograph of the single Photon counting cell.

The first prototypes of these Photon counting electronics chips are presently under test and giving promising results [132]. The characterisation of the pixel read-out electronics chip in combination with a gallium arsenide is foreseen for the very near future.

References

[1]   L.R.Evans, "The Large Hadron collider", CERN/AC-95-002.

[2]   E.H. M. Heijne et al, "The silicon micropattern detector: a dream?", *Nucl. Instr. And Meth. A 273(1988)615.*

[3]   E. Heijne, "Development of silicon pixel detectors: an introduction", *Nucl. Instr. and Meth.A 275(1989)467*

[4]   E. Heijne et al., "First operation of a 72 k element hybrid silicon micropattern pixel detector array", *Nucl. Instr. Meth. A 349 (1994) 138.*

[5]   E. B. Hughes et al.,"Prospects for non-invasive angiography with tunable X-rays", *Nucl. Instr. Meth. B 10/11 (1985) 323*

[6]   D. Cline et al., "A compact sub-angstrom X-ray source for protein crystallography, nano-technology and coronary angiography", *UCLA-CAA0101-6/93.*

[7]   L. Fatigante, "Breast cancer and early diagnosis: clinical implications", *presented at the Fifth international workshop on gallium arsenide and related compounds, Cividale del Friuli, June 1997.*

[8]   C. Shieber et al., "CdTe detectors in medicine: a review of current applications and future.perspectives", *Nucl. Instr. Meth. A 322 (1992) 604*

[9]   D.L.Lee et al., "A new digital detector for projection radiology", *Proc. SPIE Vol. 2432 (1995) 237.*

[10] G. Madonna, "Autoradiografia digitale con rivelatore a silicio cristallino a microstrisce", Tesi di laurea, Universita' degli studi di Napoli, facolta' di Scienze, dipartimento di Fisica. 1996.

[11] H. D. Zeman et al. ,"Evaluation of Synchrotron X-rays for transvenous coronary angiography, *Nuch. Instr. Meth 222 (1984) 308*

[12] G. Knoll, "Radiation detection and measurements", John Wiley and Sons 1989.

[13] S. Webb, "The physics of medical imaging", Institute of Physics Publishing, Bristol U.K. 1988

[14] A.Sandborg et al., "Influence of X-ray energy spectrum, contrasting detail and detector on the signal-to-noise ratio (SNR) and detective quantum efficiency (DQE) in projection radiography", *Phys. Med. Biol., 1992, vol 37, No 6, 1245.*

[15] U. Welander et al., "Resolution as defined by line spread function and modulation transfer functions for four digital intraoral radiographic systems", *Oral and maxillofacial radiology, Vol. 78 No. 1 July 1994.*

[16] U. Welander et al., "Absolute measures of image quality for the Sens-A-Ray* direct digital intraoral radiography system", *Oral and maxillofacial radiology, Vol. 80 No. 3 Sept. 1995.*

[17] F. Arfelli et al., "Silicon detectors for synchrotron radiation digital mammography", *Nucl. Instr. Meth. A 360 (1995) 283.*

[18] M. J. Cree et al., "Towards direct reconstruction from a gamma camera based on Compton scattering", *IEEE Trans. Med. Imag. Vol. 13, No. 2, June 1994.*

[19] C.J. Solomon et al., "Gamma ray imaging with silicon detectors - a Compton camera for radionuclide imaging in medicine", *Nucl. Inst. Meth. A 273 (1988) 787*

[20] T. Kamae et al., "Prototype design of multiple Compton gamma-ray camera", *IEEE Trans. Nucl. Sci. Vol. 35, No.1 February 1988.*

[21] F. Pederson et al, "Using a hybrid pixel detector for dynamic radiography, proceedings of the *Nuclear Science Symposium 1996, Anaheim, California.*

[22] Preciosa Ltd., Opletalova 17, 466 67 Jablonec nad Nisou, Czech Republic.

[23] S. Sze, "Semiconductor devices, Physics and Technology", John Wiley & Sons, 1985.

[24] S. M. Sze, "Physics of semiconductor devices", John Wiley & Sons, 1981.

[25] W. Bencivelli et al. Evaluation of elemental and compound semiconductors for X-ray digital radiography. *Nucl Instr. Meth. A 310 (1991) 210.*

[26] C. J. S. Damerell, "Vertex detectors: the state of the art and future prospects", lectures presented at the *Twenty Third Annual Summer Institute On Particle Physics, SLAC, Stanford, California 94309. July 1995.*

[27] M. R. Squillante et al., *Semiconductors and semimetals, Vol. 43 (1995) 470.*

[28] F. Sauli, "High-rate, position-sensitive radiation detectors: recent developments and application in particle physics, medicine and biology", *CERN-PPE/94-150.*

[29] A. Olivo et al., "Imaging with silicon pixel detectors", presented at the *"Fifth international workshop on GaAs detectors and related compounds"* Cividale del Friuli, June 1997.

[30] F. Arfelli et al, "Silicon X-ray detector for syncrhrotron radiation digital radiology", *Nucl. Instr. Meth A 353(1994) 366*

[31] E. M. Schooneveld et al., " A silicon detection System for DNA sequencing", *Nucl. Instr. Meth. A 305(1991) 581*

[32] E. Bertolucci et al.,"Autoradiography with silicon strip detectors", *submitted to Physics in medicine and Biology.*

[33] B. Alfano et al.,"Digital imaging in radiology:preliminary results obtained with a high spatial resolution 2D silicon detector", *IEEE Trans. Nucl. Sci. Vol. 40 (1993) 987.*

[34] M. Conti, "Silicon microstrip detectors for X-ray imaging with a TDC and transputer DAQ", *Nucl. Instr. Meth. A 360(1995)287.*

[35] A. Czermak et al.,"A new 2-dimensional high resolution Si detector for β^- and γ-radiography", *Nucl. Instr. Meth. A 360(1995)290.*

[36] C.J.S. Damerell et al, " Charge-coupled devices for particle detector with high spatial resolution" *Nucl .Instr. Meth., 185 (1981) 33.*

[37] D. Heidtmann et al., CCDs propel medical diagnosis into digital format", *Laser Focus World, Biomedical Imaging, december 1991.*

[38] Fisher corporation, 12300 North Grant street, Denver, Colorado 80241. MAMMOVISION, product data.

[39] M.G. Strauss et al.,"CCD-based detector for protein crystallography", *Nucl. Insr. Meth. A297 (1990) 275*

[40] J.H. MacDonald et al.,"Preliminary results from a novel CCD-based imaging system for biomedical applications", Dept. Of Physics, Institute of cancer research, Royal Marsden Hospital, Sutton Surrey UK.

[41] B.E. Burke et al., "CCD Imagers for soft X-ray astronomy", *presented at the 1993 IEEE workshop on Charge-Couple Devices and advanced image sensors", W. Davies centre for computer research, University of Waterloo, Waterloo Ontario, Canada June 1993*

[42] Hedges et al., "VXD3: The SLD vertex detector upgrade based on a 307M pixel CCD", *presented to the 4th international workshop on vertex detectors, Vertex 95- 1996 WIS 96-18.*

[43] A Bakker et al., "A 3-stage 80: 7mm image intensifier combination for the CERN UA2 scintillating fibre detector", *presented at the workshop on scintillating fibres development for the SSC, Batavia IL, USA Nov. 1988.*

[44] P. Annis et al., "The Chorus scintillating fiber tracker and opto-electronic read-out system", *Subm. To Nucl. Instr. Meth. 1997*

[45] L. Struder et al.,"Device modelling of fully depletable CCDs", *Nucl. Instr. Meth. A253 (1987)386.*

[46] Schick Technologies, 31-00 47th avenue Long Island, New York Computed Dental Radiography

[47] M. Campbell et al., "A 10 MHz micropower CMOS front end for direct read-out of pixel detectors" *Nucl. Instr. Meth A 290 (1990) 149.*

[48] J. F. Arens et al., "Development of pixel detector for SDC vertex tracking", *3rd International Symposium on SSC, Atlanta (1991*

[49] D.M. Raymond et al, "A prototype pixel read-out chip for asynchronous detection applications", *Nucl. Instr. Meth. A310 (1991) 552.*

[50] P. Delpierre et al., "Large scale pixel detectors for DELPHI at LEP200 and ATLAS at LHC", *Nucl. Instr. Meth. A 342 (1994) 233*

[51] ATLAS technical proposal for a general purpose pp experiment at the Large Hadron Collider at CERN. *CERN/LHCC/94-43*

[52] CMS, The Compact Muon Solenoid technical proposal, *CERN/LHCC 94-38*

[53] M. Cuzin et al, "Preliminary characterization of a new hybrid structure with CdTe: X-ray imaging capabilities", *SPIE Vol. 2278 X-ray and UV detectors (1994)/21.*

[54] M. Raymond et al., "A 2-D amplifier array chip for pixel detector read-out", *Nucl. Instr. Meth A 348 (1994) 673.*

[55] C. Ronnqvist et al., "A 64-channel pixel read-out chip for dynamic X-ray imaging", *presented at the 1996 IEEE Nuclear Science Symposium and Medical Imaging Conference, Anaheim, CA 1996.*

[56] F. L. Augustine, "Multiplexed read-out electronics for imaging spectroscopy of high-energy X-ray and gamma photons", *Nucl. Instr. Meth A 353 (1994) 201.*

[57] E. R. Fossum, "Novel sensor enables low-power, miniaturized imagers", *Photonics Spectra, January 1996.*

[58] F. Pedersen, "The DIXI project, a hybrid pixel detector for projection imaging in radiology", *Department of radiation sciences, Uppsala University, Box 535, S-751 21 Uppsala, Sweden. ISSN 0284-2769 1996*

[59] E.H.M. Heijne et al. "Development of hybrid and monolithic silicon micropattern detectors", *CERN DRDC/90-81.*

[60] F. Anghinolfi et al., "A 1006 element hybrid silicon pixel detector with strobed binary output", *IEEE Trans. Nucl. Sc. NSS 39 (1992)*

[61] H. Beker et al, "A hybrid silicon pixel telescope tested in a heavy-ion experiment", *Nucl. Instr. Meth. A 332 (1993) 188.*

[62] M. Campbell et al., "Development of a pixel read-out chip compatible with large area coverage", *Nucl. Instr. Meth. A 342 (1994) 52.*

[63] E. Heijne et al., "LHC1: A semiconductor pixel detector read-out chip with internal, tunable delay providing a binary pattern of selected events", *Nucl. Instr.Meth. A 383 (1996) 55.*

[64] J. Franka et al, "Solder bump technology: present and future", *Semiconductor fabtech, 289*

[65] D. J. Pedder, "Flip-chip solder bonding for advanced service structures", *Plessey reasearch and technology, research review 1989.*

138

[66] T. Mimura, "System module: a new chip-on-chip module technology", *IEEE Custom Integrated Circuits Conference 1997, 439.*

[67] Alenia S.p.A., Via Tiburtina Km 12.400, I-00131 Roma, Italy.

[68] G. Lanzieri, "Advances in GaAs material and contact technology", presented at the 5*th* *International workshop on gallium arsenide and related compounds" Cividale del Friuli Italy, 17-20 June 1997*

[69] LETI, Departement Systemes, 85 X, 38041 Grenoble Cedex, France.

[70] IMC AB, KTH Stockholm, Sweden

[71] M. Cuzin, "CdTe in photoconductive applications. Fast detector for metrology and X-ray imaging", *Nucl. Inst. Meth. A 322 (1992) 341.*

[72] C.J. Kenny et al., "A prototype monolithic pixel detector", *Nucl. Instr. Meth A 342 (1994) 59.*

[73] W. Snoeys et al.,"First beam test results from a monolithic silicon pixel detector", *Nucl. Inst. Meth. A 326 (1993) 144.*

[74] S. Parker et al., "Digital quantum mammography with monolithic silicon pixel detectors", *Proposal submitted to the National Institutes of Health, January 1995.*

[75] S. Parker et al," Breast cancer calcification measurements using direct X-ray detection in a monolithic silicon pixel detector", *IEEE Trans. Nucl. Sci. Vol. 41, No 6 Dec. 1994*

[76] S. Avrillon et al., "Preliminary test results from a single-sided 2-dimensional detector using p-MOS pixels", presented at the 9*th* *international workshop on room temperature semiconductors X and γ detectors associated electronics and applications, Grenoble Sept. 1995*

[77] L. E. Antonuck et al. ,"Thin-Film, flat-panel, composite imagers for projection and tomographic imaging", *IEEE Trans. Med. Imag. Vol. 13 No 3 (482) Sept. 1994.*

[78] D. L. Lee et al.,"A new digital detector for projection radiography", *SPIE Vol 2432 / 237.*

[79] S. Parker et al,"3D- A new architecture for solid state radiation detectors", *presented at the 3rd workshop on pixel detectors, Bari April 1996.*

[80] V. Palmieri et al.," Hybrid superconducting pixel detector", *to be printed in Nucl. Inst. Meth.*

[81] D. S. McGregor et al., "Gallium arsenide radiation detectors and spectrometers", *Semiconductors and semimetals Vol. 43, 383.*

[82] F. Nava et al., "Influence of electron traps on charge-collection efficiency in GaAs radiation detectors", *Nucl. Instr. Meth. A 349 (1994) 156.*

[83] L. Berluti et al., "Gallium Arsenide particle detectors: a study of the active region and charge-collection efficiency", *Nucl. Instr. Meth. A 354 (1995) 364.*

[84]   M. Rogalla et al, "Characterization of semi-insulating GaAs for detector application" *to be published in Nucl. Inst. and Meth.*.

[85]   A. Prasad, "Non-stoichiometric defects in III-V semiconductors", PhD thesis, .Chemistry Department University of California, Berkeley (1996).

[86]   M. Alietti et al, "An optical-beam-induced-current study of active region and charge collection efficiency of GaAs particle detectors", *Nucl.Instr. Meth. A 355 (1995) 420.*

[87]   W. Braunschweig et al., "Charge collection efficiencies and reverse current densities of GaAs detectors", *CERN lib. PITHA 94-67*

[88]   M. Kaminska et al., "EL2 defects in GaAs", *Semiconductors and semimetals, Vol. 38, 59.*

[89]   G. M. Martin et al., "The mid-gap donor level EL2 in GaAs", *Deep centers in semiconductors", S. Pantelides (Gordon and Breach Science Publishers, New York, 1986) , 457.*

[90]   R-S Tang et al., "Compensation assessment in "undoped" high-resistivity GaAs", *J. Appl. Phys. 66 (1), July 1989, 256.*

[91]   T. Kubicki et al., "Calculation of the electric field in GaAs particle detectors", *Nucl. Instr. Meth. A 345 (1994) 468.*

[92]   D. S. McGregor et al. "Present status of undoped semi-insulating LEC bulk GaAs as a radiation spectrometer", *Nucl. Instr. Meth. A 343 (1994) 527.*

[93]   L. Polenta, "Electric field behaviour and space charge regions in SI GaAs Schottky diodes", presented at the *"Fifth international workshop on GaAs detectors and related compounds"* Cividale del Friuli, June 1997.

[94]   D. McGregor et al., "Evidence for field enhanced electron capture by EL2 centres in semi-insulating GaAs and the effect on GaAs radiation detectors", *J. Appl. Phys. 75 (12), June 1994, 7910.*

[95]   J Frenkel, "On pre-breakdown phoenomena in insulators and electronic semiconductors". *Phys. Rev. 54, 647 (1938).*

[96]   P.T. Panousis et al., "Field enhanced emission and constant-field domains in semiconductors with deep traps". *App. Phys. Lett. 15 (3) 1969, 79.*

[97]   V. Y. Prinz et al., "Influence of a strong electric field on the carrier capture cross-section by non-radiative deep level centers in GaAs". *Phys.Stat..Sol. (B) 118, (1983), 159.*

[98]   J. C. Adams et al., "Below band-gap electroabsorption in bulk semi-insulating GaAs". *App. Phys.Lett. 63 (5), 633 (1993).*

[99]   A. Pillukat et al. "Magnetic circular dichroism of the diamagnetic charge state of EL2 in GaAs", *App. Phys Lett. 60 (22) 1992, 2794.*

[100] Freiburger Material Forschungszentrum, Stefan Meyer strasse 21 Freiburg, Germany.

[101] Center for Advanced Materials, Lawrence Berkeley Laboratory, Dept. Of Material Science, University of California, Berkeley, California 94720. U.S.A.

[102] D. Ball, "An introduction to magnetic circular dichroism spectroscopy: general theory and applications", *Spectroscopy 6 (1), 18 (1991).*

[103] D. Hoffmann et al., "Optical and magneto-optical determination of the EL2 concentrations in semi-insulating GaAs", *Semic. Sci. Techn. 6 (1991) 170.*

[104] G. Martin, "Proceedings of the 1ˢᵗ Conf. On Semi-insulating III-V Materials, *Edited by G.J. Rhees, Shiva Publishing Ltd., 13-28 (1980).*

[105] A. Chantre et al, "Deep level optical spectroscopy in GaAs", *Phys. Rev. B23, 5335 (1981).*

[106] D. Holmes et al., "Stoichiometry-controlled compensation in liquid encapsulated Czochralski GaAs", *App. Phys. Lett. 40, 46 (1982).*

[107] G. Martin, "Optical assessment of the main electron trap in bulk semi-insulating GaAs". *Appl. Phys. Lett 39(9) 1981.*

[108] Freiberger Compound Materials GmbH, Berthelsdorfer Str. 113, D-09599 Freiberg / Sachsen.

[109] F. Nava et al, "Performances of SI GaAs detectors fabricated with implanted ohmic contacts", *submitted to IEEE Trans. Nucl .Sci.*

[110] G. Bertuccio et al, Performances of SI GaAs detectors at 20C and at -30C for X and g - rays spectroscopy, *submitted to Nucl Instr. Meth.*

[111] R. Bates et al, "Gallium arsenide pixel detectors", presented at the *"Fifth international workshop on GaAs detectors and related compounds"* Cividale del Friuli, June 1997.

[112] C. Da Via' et al, "Gallium Arsenide pixel detectors for medical imaging", *to be published on Nucl. Instr. Meth.*

[113] F.H. Attix, Introduction to radiological physics and radiation dosimetry, *Wiley Interscience 89, 569 (1986).*

[114] S. R. Amendolia et al., "Use of silicon and GaAs pixel detectors for digital autoradiography". *IEEE Trans. Nucl. Scie. Vol. 44, No 3,(929), June 1997.*

[115] E Bertolucci et al. , Autoradiography with silicon strip detectors, *subm. to Physics in Medicine and Biology*

[116] J.C. Shuterland, electronic imaging of electrophoretic gels and blots, *Advances in electrophoresis 6, Chrambach et al, VCH Publishers: New York and Weinheim (1993) 1-42.*

[117] Molecular Dynamics Phosphor Imager SF

[118] United Detector Technology Catalogue, model number FIL 100V.

[119] ABB-Hafo, 850nm pigtailed (50/125 NA=0.2)

[120] Hewlett Packard,Company, P.O. Box 4026, Englewood, Co 80155-4026.

[121] B.H. Candy, "Photomultiplier characteristics and practice relevant to photon counting", *Rev. Sci. Instrum. 56 (2), feb. 1985.*

[122] M. L. Meade, "Instrumentation aspects of photon counting applied to photometry", *J. Phys. E: Sci. Instrum., Vol. 14, 1981.*

[123] C. Da Via et al., Imaging of visible photons using hybrid silicon pixel detectors, Nucl. Instr. and Meth. A 355(1995)414.

[124] DEP (Delft Electronicische Producten), Dwazziewegen 2, 9300 Ab Roden (Dr.), Holland.

[125] Kuraray Co. Ltd., Methacrylic Resin Division, Hatchobory 2-Chome, Chuo-ku, Tokyo 104, Japan.

[126] A. Cardini et al., Laboratory test of a high resolution scintillating fibre hodoscope, *INFN PI/AE 94/08, submitted to Nucl. Instrum. Methods Phys. Res., 1994.*

[127] INTEVAC, Eo Sensors Division, 601 California Ave, Palo Alto, California 94304 – 0883, USA.

[128] Schott Schleiffer AG, Feldbachstrasse, 80 CH-8714 Feldbach.

[129] R. Pani et al., "Multi-crystal YAP:Ce detector system for position sensitive measurements", *submitted to Nucl. Instr. and Meth. A (1994).*

[130] D. Puertolas et al.,"An ISPA camera for gamma rays", IEEE trans. Nucl. Sci. , Vol. **42**, No. 6(2221) Dec. 1995.

[131] D. Puertolas et al., "An ISPA camera for beta radiography", IEEE Trans. Nucl. Sci., Vol. **43**, No. 5 (2477) Oct. 1996

[132] M. Campbell et al., "Read out for a pixel matrix with 15-bit single photon counting ", *submitted to the IEEE Nuclear Science Symposium, Albuquerque, New Mexico, November 1997.*

Acknowledgements

143